Scuola di Dottorato di Ricerca
Ingegneria dell'innovazione industriale
XXXIII Ciclo

An integrated modelling approach for tunnel ventilation systems

Tutore scientifico
Prof. Ing. Diego Angeli

Candidato
Dott. Ing. Pietro Cingi

Coordinatore del Dottorato
Prof. Ing. Franco Zambonelli

Università degli Studi di Modena e Reggio Emilia
Anno Accademico 2020-2021

in memoria
di Maurizio Cingi

Sommario in lingua italiana

Un modello semplificato in grado di prevedere i flussi di aria in un tunnel stradale è sviluppato e descritto nel presente lavoro. Tale modello fornisce uno strumento snello e di rapida esecuzione per la previsione e valutazione del funzionamento del sistema di ventilazione, date condizioni iniziali e condizioni al contorno.

Il modello è sviluppato a partire dalle equazioni di bilancio della massa, della quantità di moto e dell'energia, discretizzate su un dominio monodimensionale basato su un modello topologico a grafo. L'algoritmo di soluzione, assieme ad alcuni accorgimenti volti al trattamento dei termini sorgente/pozzo, è illustrato nel dettaglio. Il metodo numerico discusso è implementato in Python secondo logica a oggetti, che garantisce flessibilità al codice.

Un'istanza del modello, adattata alla geometria del Tunnel del Monte Bianco (TMB) è calibrata sulla base dei risultati di una precedente campagna sperimentale tramite ottimizzazione. Tale processo è frutto dell'adattamento e implementazione metodo di ottimizzazione genetico basato sull'Evoluzione Differenziale (DES). L'approccio è validato mediante il confronto dei risultati di simulazioni stazionarie con dati esterni alla calibrazione, provenienti dal database del sistema di controllo del TMB. Il modello calibrato è inoltre impiegato per la simulazione transitoria di due degli eventi presenti nel database del TMB, con esiti soddisfacenti.

Infine, un'ipotesi tuttora ampiamente adottata nell'ambito della gesione di incendi in tunnel a ventilazione trasversale, ossia che l'annullamento della velocità longitudinale nella porzione di tunnel interessata dall'incendio garantisca il confinamento del fumo, è stata discussa e provata mediante esperimenti su un modello in scala.

L'approccio sviluppato consente il calcolo in tempi rapidi di profili longitudinali di pressione, temperatura e velocità con ragionevole precisione. La disponibilità di un modello di questo tipo fornisce ad esempio un supporto fondamentale per effettuare studi parametrici sul sistema di ventilazione. Nonostante esistano ad oggi molti altri esempi di codici 1D per il calcolo dei flussi in tunnel stradali, molti di questi non simulano l'intero sistema di ventilazione – facendo quindi uso di ipotesi semplificative molto forti (e.g. portata imposta alle bocchette di immissione ed estrazione). Al contrario, l'approccio sviluppato simula il flusso nei canali di ventilazione, i cui coefficienti di attrito sono ottenuti mediante calibrazione sulla base di dati sperimentali ad alta risoluzione.

Introduction

In many civil infrastructures, including road and railway tunnels, underground stations and car parks, airflow control is crucial for the safety of users. This is even more the case when operating in emergency conditions, since air velocity is one of the main factors influencing smoke or pollutants distribution in case of fire or other hazardous events. Therefore, along the years, a huge effort has been put in the design and testing of airflow control strategies, aimed at quickly containing and evacuating vitiated air from the areas occupied by users.

The present work is framed in a long-standing research cooperation among the engineering departments of the University of Modena and Reggio Emilia, the Gruppo Europeo di Interesse Economico del Traforo del Monte Bianco (GEIE-TMB), the French-Italian consortium in charge of the maintenance and management of the *Mont Blanc* tunnel (TMB), and Mimesis, an engineering company specialized in fluid dynamics, concerning the study and optimization of the *Mont Blanc* tunnel ventilation system. Within such framework the ventilation system has been the subject of a number of studies, whose results have all been pivotal to the development of the computational model presented here.

The main aim of this joint research is to minimize the response time of the ventilation system to a fire event in the tunnel. The pursued condition consists in having all the smoke confined within a 600 meters long tunnel stretch, centered on the event location, in the minimum possible time. To this aim, the availability of accurate and fast prediction methods is a crucial asset to devise, and subsequently optimize, advanced control strategies. While a full 3D simulation can be a helpful tool for addressing issues involving limited parts or details of the full domain (e.g. to estimate the effect of a single axial fan on the surrounding tunnel stretch), its application to the whole domain not feasible due to the size of the latter.

Hence, the present study is motivated by the need to devise an integrated approach, aimed at the creation of reliable 1D numerical models of specific road tunnels with relatively complex ventilation systems, as in the case of the *Mont Blanc* tunnel.

Such an approach must be based on a solid numerical algorithm for the solution of a weakly compressible flow network. The code should contain a toolkit, organized in modules so as to maintain maximum flexibility, in order to quickly set up a "digital twin" of a given tunnel. Since any adaptation of the numerical model to a specific tunnel would need experimental data for its calibration, the approach should necessarily include a standardized and repeatable process for gathering the field data needed for the calibration and validation of the model itself.

Within the present work, a computational tool is specifically developed to predicting the airflow distribution in the TMB ventilation system. The choice of developing an in-house tool, instead of resorting to commercial 1D network flow solvers or general-purpose scientific computation packages, is motivated by a number of inherent advantages, including

the high degree of customization, ease of portability and deployment, and code reuse, for example in a co-simulation (also known as multi-scale) framework.

Chapter 1 contains a literature review. The history of the development of computational models of road tunnels is briefly resumed, highliting the various possible approaches. Then, the state of the art is framed, with a focus on simplified models – that are meant to be quick, but maintain a reasonable accuracy – as well as on the strategies employed for saving computational time and resources in more complex simulations, such as multi-scale.

A detailed description of the physical domain composed by the *Mont Blanc* tunnel and its ventilation channels is provided in Chapter 2, as well as a list of the measurement devices and ventilation machinery installed in the system. The control system of the tunnel is also commented, along with some insights and examples regarding the management of an emergency event in the *Mont Blanc* tunnel.

The backbone of the numerical model is outlined in Chapter 3, starting from differential governing equations which are simplified, integrated, and discretized on the base of a topological representation based on an oriented graph. This allows for the reduction of the problem to a 1D one, and provides an ideal domain for tackling balance equations by means of an iterative procedure. The expression of the resulting equations in matrix form is detailed, and a tailor made solution algorithm is developed for their solution. The representation sources/sinks of both momentum (e.g. fans, friction) and heat (e.g. a fire, or heat exchange with the tunnel walls) are explained in detail. The non-linear terms involved in some of the momentum sources/sinks (i.e. fans, friction terms) are treated so as to mantain the momentum conservation equations in linear form, while ensuring higher stability of the solution procedure. Lastly, a specific logic for managing the sequence of events (e.g. turning on/off of a fan) that can happen at certain time instances within a transient simulation is designed. Such approach is integrated with a note on the transients which are to be considered when activating or deactivating a fan.

In the numerical model, all the relevant thermo-fluid dynamic features of the *Mont Blanc* tunnel ventilation system are modeled by means of integral transfer parameters. Such parameters need to be finely tuned based on reliable physical data, in order for the model to reproduce the behavior of the actual system with satisfactory accuracy. For this reason, within Chapter 4 a calibration process is explained and performed by means of a genetic optimization algorithm. A detailed report on the in-situ collection of the dataset by means of a continuous airflow acquisition facility is provided. Then, a comparison between calibrated model prediction and experimental data is brought forth.

In Chapter 5, the model instance that was calibrated at the previous chapter is employed for validating the model in transient conditions. Two transient simulations were set up to emulate the time dependent tunnel velocity profiles during two emergency events that were recorded in the *Mont Blanc* tunnel by the embedded control system. While the activation times of the centrifugal fans are taken from the experimental data log, the automated control logic of the axial jet-fans is fully simulated by means of a PID controller sub-model. The results of the comparison are illustrated and discussed.

Lastly, in Chapter 6, an assumption that has been taken as a starting point for the design of the current ventilation system of *Mont Blanc* tunnel is discussed, i.e. to consider the smoke as successfully confined in case of null longitudinal velocity value in correspondence of the emergency event location. Its validity is proven through a set of experiments on a scaled model of a road tunnel with transverse ventilation, capable of simulating the action of a pressure difference between the tunnel ends.

The developement of a 1D model of a road tunnel does not represent a novelty per se: this kind of model has been very widely used for the design and control of ventilation systems in tunnels for at least 60 years. However, in most cases, the ducts constituting the ventilation systems are not part of the numerical model. Therefore, simplifying assumptions need to be made, such as constant flow rates at insufflation or extraction points. In the case of a very long and deep tunnel, more variables may significantly influence the flow, such as the outside temperature, hence the interest of developing such a complex 1D model.

Moreover, it is arguably the first time a model of this kind is developed on the basis of an extensive measurement campaign, that has been conceived and carried out specifically for the model calibration. Thanks to the calibration process, the model is capable of predicting with sufficient accuracy the flow in the ventilation ducts, leading to a satisfactory prediction on the longitudinal velocity in the main tunnel.

Despite its lower accuracy with respect to 3D full scale models, the present method is proven to be a convenient and lightweight computational tool, capable of reproducing different ventilation scenarios potentially occurring in the *Mont Blanc* tunnel with satisfactory accuracy, and applicable with relative ease to a large variety of similar systems.

Contents

Sommario in lingua italiana **i**

Introduction **iii**

1 Background and literature review **1**
1.1 Introduction . . . 1
1.2 Small and large scale experiments . . . 1
1.3 Numerical methods . . . 3
1.3.1 1D models . . . 4
1.3.2 3D models . . . 6
1.3.3 Multiscale models . . . 8
1.3.4 The present study . . . 9

2 Case study **11**
2.1 The *Mont Blanc* tunnel . . . 11
2.2 Ventilation system . . . 13
2.2.1 Transverse ventilation system . . . 13
2.3 Axial jet fans . . . 15
2.4 Control system . . . 15
2.4.1 Velocity profile estimation . . . 15
2.4.2 Control logic . . . 16
2.4.3 Fire management examples . . . 18

3 Numerical model **21**
3.1 Introduction . . . 21
3.2 Governing equations . . . 21
3.3 Simplifying assumptions . . . 22
3.4 Boundary conditions . . . 24
3.5 Topological representation . . . 25
3.5.1 Network features . . . 26
3.6 Time and space discretization . . . 27
3.6.1 Interpolation schemes . . . 28
3.6.2 Incidence matrix and its transpose . . . 29
3.6.3 Central differences . . . 30
3.6.4 Upwind . . . 30
3.6.5 Discrete equations . . . 31
3.7 Governing equations in matrix form . . . 33

3.8 Solution algorithm . . . 37
3.9 Treatment of source/sink terms . . . 38
3.9.1 Friction . . . 39
3.9.2 Centrifugal fans . . . 40
3.9.3 Jet fans . . . 47
3.9.4 Heat transfer . . . 49
3.10 Event based logic for transient simulations in the TMB . . . 50
3.10.1 Activation ramps . . . 51
3.10.2 Experimental data and modeled ramps . . . 51
3.11 Some notes on model implementation . . . 57

4 Model calibration 65
4.1 Introduction . . . 65
4.2 Parameters choice . . . 65
4.3 An alternative approach: equivalent roughness . . . 66
4.4 Reference data . . . 67
4.4.1 Measurement facility . . . 67
4.4.2 Measurement campaign . . . 68
4.4.3 Velocity profiles . . . 69
4.4.4 Natural draught . . . 72
4.5 Error definition . . . 76
4.6 Algorithm and hyperparameters choice . . . 76
4.6.1 Parallel implementation . . . 78
4.7 Calibration Results . . . 78
4.8 Steady state validation tests . . . 82

5 Validation in unsteady condidions 85
5.1 Introduction . . . 85
5.1.1 PID control . . . 85
5.1.2 Jet fans management in the numerical model . . . 86
5.2 Experimental data set . . . 87
5.3 Applications . . . 88
5.4 Results . . . 88

6 Experimental verification of smoke confinement 95
6.1 Introduction . . . 95
6.2 Experimental facility description . . . 96
6.2.1 Rotameter correction . . . 98
6.3 Governing parameters and flow conditions . . . 99
6.4 Dimensional analysis . . . 101
6.5 Experimental protocol . . . 103
6.6 Design of experiments . . . 104
6.7 Results . . . 104
6.7.1 Influence of the source parameters . . . 104
6.7.2 Influence of the dampers characteristics . . . 105
6.7.3 Flow rate at the depressurized end . . . 105

7 Conclusions 109

List of Symbols **117**

Ringraziamenti **129**

Chapter 1

Background and literature review

1.1 Introduction

Airflow control is a critical issue in a large number of civil infrastructures, expecially road and railway tunnels, since it determines air quality and breathability in ordinary operating conditions, and temperature distribution and smoke movement in case of fire. Such a topic received great interest during the last century, and many efforts were put in the characterization (via in situ measurements, experiments on scaled models) and prediction (via numerical modelling) of the flow conditions which can take place.

In the following, the most relevant examples of the different approaches will be pointed out and briefly explained, along with some minor works that are very specific to the present case study.

1.2 Small and large scale experiments

Full scale tests can be conducted either in unused tunnels, or even in operating road tunnels during a traffic closure. This approach often requires large financial investments in terms of measurement facilities, that can grow even bigger if working on an operating tunnel, due to the missed incomes implied by temporary closure of the infrastructure. On the other hand this approach provides large amounts of collected data, possibly leading to a more thorough understanding of the physical behaviour of the system, and to the development of more precise computational models.

A wide review of the experiments on tunnel fires which were conducted in the second part of the 20th century is available at the dedicated chapter of [1]. Among the examples from such time span, *EUREKA project EU 499 FIRETUN* [2] is possibly the most notable: with nine European nations joining their efforts, 20 tests were conducted between 1990 and 1992 and evaluated from 1993 through 1995. The numerous important results gained during the project formed a strong basis for international discussion of fire safety concepts. The Memorial Tunnel fire ventilation test program [3] is also worth to be mentioned for the size of the experimental campaign which included 98 tests, tackling a variety of possible ventilation strategies (including transverse ventilation, natural ventilation and longitudinal ventilation with jet fans).

Fourteen full-scale fire tests were carried out between 2000 and 2001 in the Second Benelux Tunnel [4]. The tests employed several kinds of fire sources: fuel pans, cars, a van

and covered truck loads. Temperatures, radiation levels and optical densities in the tunnel were measured, as well as smoke velocities and heat release rates.

The response to forced ventilation of vehicles and pool fires was instead studied by Carvel [5], who found that the size of a large HGV fire is greatly increased by forced longitudinal ventilation, while ,for small pool fires and car fires, increasing the ventilation tends to reduce the size of the fire. Fire and ventilation tests performed in the *Mont Blanc* road tunnel in 2000 are carefully recorded and commented in [6] where the influence of the ventilation regimes on the smoke progress is analyzed in detail. Martegani *et al.* [7] carried out tests to investigate the flow field resulting from the installation of coupled jet fans at different pitch angles.

Do to their high specificity to the case study, in situ measurement campaigns are still broadly employed. Kròl *et al.* [8] carried out a thorough analysis on the effects of natural draught on the overall flow in a longitudinally ventilated tunnel. The measurement facility consisted in two poles supporting a number of anemometers stacked vertically: by moving such poles transversely through a section, they were able to acquire flow velocity on a remarkably fine grid of measurement points. Wang *et al.* [9] investigated jet fans performances in a very long tunnel (more than 18 km) by means of a grid of vane anemometers, placed at different locations along the tunnel. Further examples of employment of frames of different shapes for the handling and positioning of multiple measurement devices can be found in the recent literature [10, 11].

The variables of interest are generally: (i) concentration of pollutants, as one of the main aims of the research on road tunnel ventilation is the assessment and improvement of air quality; and (ii) air velocity, as it strongly influences the distribution of combustion products in case of emergency.

Multi-point in situ velocity measurements, also based on fixed-point anemometers, were taken inside the *Mont Blanc* tunnel by Levoni *et al.* in 2011, [12, 13]. In 2012, longitudinal velocity measurements were taken with a radically improved spatial resolution, thanks to a custom made moving measurement facility [14]; such measurement campaign will be described in detail in the dedicated section of Chapter 4.

Because of the high associated costs, often only a limited number of tests can be carried out on full scale systems. To address this issue, as well as the fact that such experiments are highly specific to the particular tunnel geometry and layout, small scale tunnel models are often used to represent ventilation and fire scenarios.

The interpretation of their results is strongly dependent on the relevant scaling laws: scaled model results can be successfully used to extrapolate proportionality constants used in semi-empirical correlations aimed at predicticting the occurrence of the smoke confinement in real tunnels.

Given the vastity of the existing literature concerning scaled models, the overview will be focused on experiments concerning tunnels equipped with a transverse ventilation system (analogously to the *Mont Blanc* tunnel).

Vauquelin and Mégret [15] conducted a series of experiments in a small-scale tunnel, in which a fire source was placed in between two exhaust ducts. Different positions and shapes of the vents, as well as different fire heat release rates (HHR) were tested. The study proves that rectangular vents located at the tunnel ceiling are more efficient than vents with other shape and location. Subsequently Vauquelin and Telle [16] performed an experimental study involving a single vent located on one side of the fire, proposing the *confinement velocity* as main flow control variable. Such a velocity is defined as the minimum adverse

velocity required to prevent the smoke from propagating past the extraction vents, and it is usually associated with a correspondent extraction flow rate at the ceiling vents (since, neglecting a pre-existing axial flow in the tunnel, setting the extraction rate also sets univocally the axial velocity profile within the tunnel). Confinement velocity was mapped for a number of values of HRR, under the assumption of a symmetrical smoke flow. More tests were then performed [17] on the same set-up, to estimate the extraction flow rate required for several values of HRR.

Wang *et al.* [18] carried out a series of full-scale experiments, studying the effect of natural convection on smoke propagation, using passive openings on the tunnel ceiling. Velocity and temperature fields were measured at ceiling level, as well as the height of the smoke layer and its extension beyond the openings.

Further studies focused more on the stability of the smoke stratification. Fan *et al.* [19] investigated the mixing process between the hot smoke layer and the cold air layer. Li *et al.* [20], through the use of Fire Dynamics Simulator, showed that such phenomenon always occurs if the air is extracted at the bottom layer. This flow condition is greatly undesirable: not only an instability in the smoke stratification compromises the presence of breathable air at ground level, but it is also proved to significantly reduce the effectiveness of the smoke extraction process [21, 22]. More recently, further experimental studies were carried out in order to investigate the influence of transverse and longitudinal systems on the efficiency of smoke confinement [23, 24].

It is only recently that tunnel ventilation research tackled hybrid ventilation systems. Lee *et al.* [25] evaluated the performance of the smoke extraction duct under natural and longitudinal ventilation flow conditions by conducting a series of fire tests in a small-scale tunnel. Such a study proves that natural ventilation is in general preferable to longitudinal ventilation, due to its smaller disturbance on the smoke stratification.

Chen *et al.* [26], after carrying out experiments in a small-scale tunnel which combined of longitudinal ventilation and one ceiling extraction opening downstream with respect to the fire, concluded that the length of smoke back-layering increases with the distance between the ceiling extraction opening and the heat source. Using the same experimental facility, Tang *et al.* [27] carried out a series of experiments which focused on the observation of the smoke stratification; they classified flow regimes obtained into different categories.

All through the last decade Salizzoni *et al.* [28, 29, 30] put in a solid effort in the investigation of the behaviour of the buoyant plume of a mixture of air and helium, raising from the floor of a tunnel and simulating a fire. Throughout the works, which investigate both longitudinal and transverse ventilation systems, the response to the variation of several parameters was analyzed: buoyant source position and size, extraction vents position and shape, buoyant mixture velocity at the source. The latest work by the group [31] compared the performances obtained through different shapes of extraction vents, while keeping their surface unvaried, in absence of a longitudinal flow. It also shed light on the influence of vertical barriers fixed on the tunnel ceiling on smoke containment and stratification.

1.3 Numerical methods

The analysis of tunnel ventilation and fire control can be also carried out by means of numerical models, i.e. mathematical representations of the physical phenomena taking place in the physical system.

Besides being usually very flexible and less case-specific than experimental analysis, a numerical simulation is significantly more economic than an experimental test. The availability of a numerical tool capable of predicting the flows in the tunnel allows for large parametric studies on the system, on a scale that would not be reachable by means of experimental approaches: if the model is sufficiently lightweight, hundreds of test can be run within one hour. The accuracy of numerical models must be validated on the base of experimental findings, so as to assess the limitations and the range of applicability of the method.

Throughout the years, several numerical approaches have been adopted to tackle problems concerning fire safety problems in tunnels.

1.3.1 1D models

A 1D model can provide a very simple representation of the behaviour of a tunnel ventilation system. All the fluid dynamic quantities are assumed to be uniform in each tunnel cross section, therefore gradients are considered to exist along the longitudinal direction only.

These models can have very low computational weight, especially if further assumptions are made, e.g. incompressible flow, convection prevailing over diffusion. Since these (and other) reasonable assumptions can often be safely applied when representing road tunnels ventilation systems, 1D models are especially attractive for parametric studies: the choice of a simplified model is often dictated by the large number of simulations to be performed.

From the second half of the last century, many 1D models have been proposed in this field: the earliest attempts at the numerical modelling of tunnel systems were made in 1950s, for addressing safety issues especially in mine tunnels. Given the limited availability of computational resources at that time, most of them consisted in 1D models based on the Hardy-Cross method. Very early schemes will not be discussed here; nonetheless it is worth to mention a few works that – benefitting from a slightly more recent conception, thus a higher computational power – can be seen as turning point in the development of this approach. The first effective attempt at a more specific numerical analysis than plain flow prediction can be found in the work bt Gruer *et al.* [32]: the effect of a fire in the system was modelled. Temperature, velocity and combustion products distributions were calculated through steady state simulations.

The *TUNVEN* program [33] is possibly the first contribution to the subject from a national institution; it is capable of solving the coupled one dimensional steady state tunnel aerodynamics and advection equations. The results of the model consist in the usual longitudinal air velocities and pollutant concentrations, and are evaluated considering tunnel design, traffic load and ventilation rate. In order to extend the validity of the model to semi-transverse and transverse ventilation systems, *TUNVEN* has been coupled with another program (*DUCT*) which is in charge of calculating the air flow through the individual ports connecting the ventilation duct to the roadway.

Within the 1990s, several other national institutions contributed to the research on the subject, leading to numerical models that are still in use for the study of tunnel fires such as *ROADTUN*, *RABIT* and *SPRINT*. The most notable example may be found in *MFIRE* [34], developed by the US Bureau of Mines and tested [35] on experimental data from a reduced scaled model by Chang *et al.*.

A more recent application can be found in the code *SPRINT* [36], which has been

designed as to include the effects of gravity driven smoke propagation on the basis of a semi-empirical correlation. The tuning of the model parameters has been performed, in this case, on the base of the data available from [3], as well as field data measured in *Mont Blanc* tunnel.

The software *CAMATT* (CAlcul Monodimensionnel Anisotherme Transitoire en Tunnel) was first published in 2003 by *CETU*. It is a fire simulator for road tunnels, and it allows to model a variety of features such as axial jet fans, piston effect due to moving vehicles, heat propagation through the tunnel walls. On the other hand, the action of transverse ventilation is significantly simplified; the ventilation ducts are not modeled, and the vents are represented by means of fixed flow rates entering/exiting the tunnel at the corresponding location.

A clever and lean approach is presented in [37], where a generic network is modeled as a directed graph. Mass, energy and species conservation equations are solved at the nodes while the momentum conservation equations are solved along branches, creating a flexible model of broad applicability that can be easily adapted also to the case of road tunnel ventilation.

Subway Environmental Simulator (*SES*) constitutes another fundamental example of network based 1D model. Although it was developed by the United States Department of Transportation in 1975, it has been upgraded multiple times [38, 39, 40] and it is still widely used. A large number of relatively recent studies [41, 42, 43, 44] employed this tool to predict fire scenarios in subway stations. The last version of the model is dated 2017, and it has been renamed *STESS* [40]. The improvement consists in the substitution of the unsteady flow solver, which has been changed from a four-step Runge Kutta to a MMKP method that leads to a quicker convergence.

Fire and Smoke Simulator (*FSSIM*) [45], developed in 1997, is a network fire model written to simulate the spread of fire and smoke in a naval vessel. However, there is nothing in the model to preclude its use for other types of compartments: in *FSSIM* each compartment is represented as a single node with surfaces (equivalent of network nodes) and vent openings (equivalent of network branches) are represented as node connections. *FSSIM* is written in Fortran95.

In 2002, Jang *et al.* [46], used a 1D model for the determination of the aerodynamic coefficients in a 1800 m long highway tunnel. The calibration, performed on the basis of detailed experimental measurements, was able to provide the installation efficiency of the jet fans, the wall friction coefficient and the averaged drag coefficients related to vehicles.

An alternative to the 1D network methods that were presented can be found in *zone models*. Such models have beed developed on the base of an experimental evidence concerning fire scenarios: the frequent formation of a hot upper layer containing the fire effluents and a cooler lower layer. Therefore, zone models represent each node (or compartment) of the network as multiple uniform zones (typically two zones, representing the aforementioned layers) with connections between adjacent zones. Zone models are capable of including empirical relationships for phenomena such as smoke back-layering. The application of zone models to fire scenarios involving buildings is very frequent. On the other hand, their applicability to road tunnels is limited from the fact that they do not contain a longitudinal momentum equation, capable of predicting tunnel smoke dynamics. Moreover their validity is limited to those scenarios in which the smoke stratification is not lost, as the grid nature is not capable of handling layers mixing.

Nonetheless, modified versions of the zone model approach were developed through the

years extending their use to road tunnels. As an example, the solution found by Charters *et al.* [47] was to add a third layer, which can be called mixing layer, between the hot smoke layer and the cold air layer. More recently Suzuki *et al.* [48] addressed the problem of the coarseness of vertical partition by adding multiple mixing layers, providing a more accurate prediction of temperature distribution. CFAST [49] and BRANZFIRE [50] are examples of zone models which are still broadly used.

A promising class of simplified models, which does not properly belong to 1D models but is worth to be mentioned here for its low computational cost, is constituted by the methods based on machine learning. This approach has been vastly used in many fields to provide rapid predictions based on large amounts of data; nonetheless, its physics-related applications are still limited. A paper providing a general overview to the appication of machine learning to fire scenarios can be found in [51], with examples of using both dimensionality reduction, and deep learning with neural networks. In comparison with CFD results, some applications show that machine learning can provide full-field predictions at least two orders of magnitude faster than CFD simulations. Nonetheless, this methods still lack of an extensive validation against experimental data and have limited accuracy in some cases. Recent works [52, 53], investigated the possibility of employing a deep learning methodology for "emulating" temperature outputs produced by the 3D computational fluid dynamic software Fire Dynamics Simulator. In particular, [53] investigated the use of transpose convolutional neural networks, which – being essentially spatial filters – may be more suitable than simple neural networks for emulating the usage of a *LES* turbolence model. The coupling with a zone model, possibly leading to a very fast multiscale model, is also proposed.

1.3.2 3D models

CFD techniques are usually adopted when detailed flow field data are needed. Such techniques are able to provide temperature pressure and velocity fields, heat fluxes, smoke distribution at a very detailed level. On the other hand, the computational requirement of methods of this kind is very high. Even for the present-day vast availability of computational power, it is not feasible to use such methods for extensive parametric analyses. Even running a full steady simulation on a small sized tunnel would imply a number of basic operations which is several orders of magnitude bigger than that of a 1D model. Therefore, full CFD models are mostly used for verification processes, that do not imply a high number of test runs.

The issue of CFD modelling of fire emergencies scenarios in road tunnels goes beyond the scope of this work. Therefore, what follows is meant to be a glimpse on the evolution of this strategy highlighting cornerstone works, as well as an analysis on the model applicability range, followed by a few examples of more recent efforts. An extensive literature review on the early developments on the subject is available in [54].

The first significant attempt at addressing the subject was presented by Fletcher *et al.* [55] in 1994. The authors compared the results from a field model developed at the University of Sydney with data obtained from experiments on pool fires in a ventilated tunnel of small size (120 m long). The k-ϵ turbulence model was enforced; combustion was modelled assuming that the chemistry is fast compared with the mixing, by a mixture fraction model. Radiant heat exchange between the gas, soot and walls was modelled using the discrete transfer method. A qualitative good match between predicted and recorded

temperatures was found, and the work highlighted a number of interesting features of the flow behaviour and modelling sensitivities. In particular, the authors also pointed out how the addition of the turbulence production due to buoyancy was crucial to predict smoke stratification while soot production had a very little impact.

A comprehensive analysis of CFD capabilities from Wu and Bakar, dated 2000, can be found in [56]. Their contribution presents a numerical analysis of two fire scenarios compared with the results obtained on a reduced scale tunnel. The numerical model has been created by means of the commercial CFD package *FLUENT*. A standard k-ϵ turbulence model was adopted, along with a mixture fraction model for combustion. Radiation heat transfer has been neglected. The comparison shows that the numerical model underpredicts the confinement velocity, with a 20% maximum relative error. On the other hand, temperatures are critically over-predicted with an error up to 500%. The authors stated that temperature overprediction is mainly due to the hypothesis of fast chemistry enforced by the choice of the combustion model, which overestimates the reaction rate.

The open source package *Fire Dynamics Simulator* (*FDS*), a CFD model of fire-driven fluid flow, was publicly released in February 2000 by the National Institute of Standards and Technology (*NIST*) of the United States Department of Commerce. The algorithm solves numerically a Large Eddy Simulation (*LES*) form of the Navier–Stokes equations appropriate for low-speed, thermally-driven flow, with an emphasis on smoke and heat transport from fires. *FDS* has seen a massive employement ever since was it released, and is still one of the main choices for the 3D modelling of tunnel fires.

Jojo *et al.* employed *FDS* to simulate two different fire hazards in a 100 m long tunnel (35 m^2 cross section) under two different fire hazards [57]. Different ventilation systems considered, such as longitudinal, semi-transverse, transverse, hybrid. Due to the unavailability of experimental data, the model was compared to semi-empirical correlations for the determination of average temperature and confinement velocity. The model overpredicts the values of up to 100%. Sensitivity analyses on the effects of the grid size and iterations limit on the required computing time and accuracy of the results are also carried out.

In 2004, both *LES* and k-ϵ turbulence models have been employed and compared by Gao *et al.* [58]. It is found that thermal stratification and smoke backflow can be predicted successfully by LES. On the other hand, local temperature fields prediction overshoots the experimental values by up to 250%.

In 2006, Lee *et al.* used *FDS* to predict temperature and flow fields ensued in a reduced scale tunnel model [59]. Temperature distribution under the ceiling showed a relatively good agreement with experimental results, with deviations within 10%.

The commercial tool *FLUENT* was employed by Ballesteros-Tajadura *et al.* to calculate temperature and velocity fields ensued by a fire of 30MW within a real 1.5 km long tunnel [60]. The smoke spread in the domain was predicted by means of time dependent simulations, although the result was not validated against experimental data.

A detailed validation of FDS has been brought forward by Kim *et al.* [61]. The authors performed a detailed sensitivity study to turbulent Prandtl number, Schmidt number, Smagorisky constant, grid size – the results of the calculations were compared to experimental findings from Memorial Tunnel test program [3].

The work pointed out that the prediction produced by FDS shows a good qualitative agreement with the experimental data set in the proximity of the fire and downstream. Concerning the tunnel section which is upstream with rescpect to the fire, FDS shows

serious limitations in predicting the smoke layer extension and height.

In 2008, Van Maele and Merci [62] brought forward a further comparison between $k-\epsilon$ and *LES* turbulence approches, comparing the confinement velocity resulting from both numerical simulations with the findings of [56]. Both *FLUENT* (for $k-\epsilon$) and *FDS* (for *LES*) were employed for the tests. As usual, combustion was modelled by means of a mixture fraction model and radiation heat transfer was neglected. The work showed that both models provided a good prediction of critical velocity, but the flow fields were not validated against experimental data.

More recently, more attempts at full scale 3D modeling were presented, their feasibility being largely due to the increase in computational resources with respect to previous decades. In 2014, Weng *et al.* [63] brought forward three full-scale model experiments within a stretch of a metro tunnel which was connected, at one end, to an underground metro station, and had the other end opened to the outside enviroment.

Temperature distributions under the tunnel ceiling were measured and compared with the resulting fields of CFD simulations were performed by *FDS*, showing a remarkably good agreement. More simulations were performed in order to outline further considerations on the dependency of the temperature at the ceiling from the fire power. Flow fields were not compared against experimental data.

In 2018, Król *et al.* [64] investigated the duration of the transients due to the swithcing of axial fans in a road tunnel. They employed *FLUENT* for performing the simulations, and compared the results with data from an experimental campaign on a real tunnel. As the concerned tunnel was not horizontal, relative static pressure had to be applied by means of a user defined function, as well as the added dynamic pressure due to the wind action at the portals. The turbulence model of choice was k-ω SST. The authors found out that the flow in the tunnel, due to the remarkable intertia of the fluid volumes involved, takes a relatively long time to adapt to the switching of fans and return to steady state. The only experimental data compared with the numerical results consisted in the near-ceiling longitudinal velocity. A further work from the same team [8] provided more data, along with the comparison of the results obtained by employing different turbulence models.

All in all, full 3D CFD models of road tunnels still have computational costs that are extremely high, even referred to the most advanced technologies available nowadays. This is due to the fact that, in order to reach a decently precise result, a CFD model needs a good evaluation of flow characteristics even at locations which are far away from the fire (the region of interest) and this can only be achieved with a fine calculation grid. Given the scale of road tunnels, to have a sufficiently fine mesh on the whole tunnel layout could mean a tremendously high cells count.

This is the reason why only a limited number of CFD studies focus on the overall performance of the ventilation systems: it is far more common to limit the CFD domain to the region of interest and rely on experimental correlations to account for the rest of the domain. Also, for this reason, validations of the full flow field against experimental data are scarce in the literature. It is indeed very common to limit the validation to the region of interest, and sometimes even to just one variable.

1.3.3 Multiscale models

An interesting compromise between the two extremes represented by 1D models and full 3D simulations can be found in multiscale (or co-simulation) methods. This approach

combines a lean, simple network model covering the most part of the domain, with local use of 3D CFD for the accurate modeling of relevant flow details. These two models are conveniently coupled, meaning that they reciprocally provide boundary conditions to each other. The computational grid can therefore be defined as hybrid: 1D elements are connected to 3D ones generating a continuous domain in the longitudinal direction. The 1D and 3D algorithms (in charge of solving each part of the network) run in parallel, dynamically exchanging information concerning the variables values at their interfaces.

This approach ensures a high level of accuracy within the regions of interest, avoiding to deal with an excessively big computational grid but also to employ oversimplifying correlations for accounting the most part of the domain. Moreover, the assumption of longitudinal gradients only (all the fluid-dynamic quantities considered to be uniform in each tunnel cross section), which is fundamental for the development of a 1D model, can be dropped for the regions where it is less appropriate (i.e. proximity of the fire, proximity of an axial jet fan) in favour of a local 3D discretization.

This method has been extensively tested and documented by Colella *et al.* [65, 66, 67, 68]. A in-house 1D network model was indeed integrated with 3D subdomains, and its reliability was proved on a wide plethora of fire scenarios. A detailed summary of the contribution of the team to this class of methods can be found in [69], while a wider literature overview on hybrid models is available in [70].

Hybrid models can also be built employing a zone model instead of a 1D network model [71]. Although this practice is not really usual for applications to road tunnel fire scenarios, it has been successfully applied to ships [72] and buildings [73]. The coupling of a deep learning based model with a zone model is proposed in [53]. Although being very promising in terms of speed, it still lacks validation against experimental data.

Vermesi *et al.* [74] provided a proof of the computational advantage guaranteed by the usage of multiscale models. The case study was solved employing *FDS* for one third of the domain, including the fire, and a 1D graph representation for the remaining part; then a full scale, parallel 3D simulation was performed using *FLUENT*. The difference between the resulting temperature fields were limited to 2%, with a computational time saving as high as 97%.

1.3.4 The present study

The availability of a quick and reliable model, capable of verifying whether the smoke released by a fire is successfully confined under certain conditions, is of crucial importance for the optimization of the control logic of a road tunnel ventilation system.

The scope of the present study is therefore the development of a lightweight, flexible model capable of predicting, with sufficient accuracy and spatial resolution, the air flows ensued in the *Mont Blanc* tunnel under specific weather conditions and ventilation system configurations. The smoke distribution is not directly investigated in this case, as the *Mont Blanc* tunnel control system evaluates the smoke confinement using a criterion based on the longitudinal velocity of the air in the tunnel stretch concerned by the emergency event: such criterion, which is discussed in Chapter 6, can be easily embedded in the model.

Given the size of the case of study, and the requirements in terms of computational weight, the only feasible option is to resort to a 1D model class. In particular, a directed graph representation, similar to [37], has been chosen. A custom segregated algorithm has been devised for solving continuity and momentum conservation equations under a set of

simplifying assumptions (e.g. incompressible flow).

The development of such an algorithm does not constitute a novelty per se as countless examples of similar models are reported in literature (see Section 1.3.1 for examples). However, very few of the works published on this topic provide a detailed description of the numerical model, and even less propose a code implementation. None of the very few codes available have been found flexible enough to be adapted to the present case study.

Moreover, it is arguably the first time a model of this kind is developed on the basis of an extensive measurement campaign, that has been conceived and carried out specifically for the model calibration. Thanks to the calibration process, the model is capable of predicting with sufficient accuracy the flow in the ventilation ducts, leading to a satisfactory prediction on the longitudinal velocity in the main tunnel.

Despite its lower accuracy with respect to 3D full scale models, the present method is proven to be a convenient and lightweight computational tool, capable of reproducing different ventilation scenarios potentially occurring in the *Mont Blanc* tunnel with satisfactory accuracy, and applicable with relative ease to a large variety of similar systems. The present 1D model constitutes a suitable basis for a multiscale model. Future development may include the integration of a 3D submodel (e.g. using FDS), that – besides increasing the spatial resolution in selected regions of the domain – would allow for a more accurate representation of the effects of a fire.

Chapter 2

Case study

In the further sections a thorough description of the physical system constituted by the *Mont Blanc* tunnel and its ventilation system is provided, along with an overview on the installed machinery, measurement and control tools. The smoke containement strategy is then presented, with the support of a practical example of emergency management by the ventilation system.

2.1 The *Mont Blanc* tunnel

The *Mont Blanc* tunnel is 11,611 m long and acts as a connection between France and Italy for road vehicles. The entrance on the French side has an altitude of 1274 m above sea level, while the Italian entrance has an altitude of 1395 m. Being the tunnel surmounted by the biggest granite massif in Europe, there is no other communication between the tunnel and the outside than at portals level. (Fig. 2.1).

From now on, Metric Point (MP) will be used for refering to specific tunnel sections: the origin of such system ($MP = 0$) is set to the French entrance. On the other hand, $MP = 11611$ refers to the Italian portal. The sign convention inside the tunnel is set accordingly: positive sign is assigned to the direction France $\rightarrow$ Italy.

The tunnel longitudinal profile is characterized by different slopes: the highest point is approximately at its middle, at $MP = 5800$, and has an altitude of 1395 m. Starting from $MP = 0$, a slope of 2.4% is encountered; from $PM = 2850$ the slope lowers to 1.8% and remains constant until the highest point. From $MP = 5800$ to the Italian portal, the slope is -0.25%. The border between France and Italy is located at $MP = 7640$.

From a planar point of view the tunnel is essentially straight, with the only exception being a bend located in the proximity of the French portal. The bended tunnel stretch is approximately 190 m long.

The tunnel average cross section is 45.2 m^2. The maximum height of the ceiling is 6 m, although the presence of devices attached to the ceiling (such as axial jet fans, sensors, lights) limits the maximum effective height to 4.70 m. The roadway is 7 m large and it is flanked by two sidewalks which are in turn 0.8 m large. The roadway presents also a sideways slope of 1% to the right side (refering to an observator travelling in the direction France $\rightarrow$ Italy).

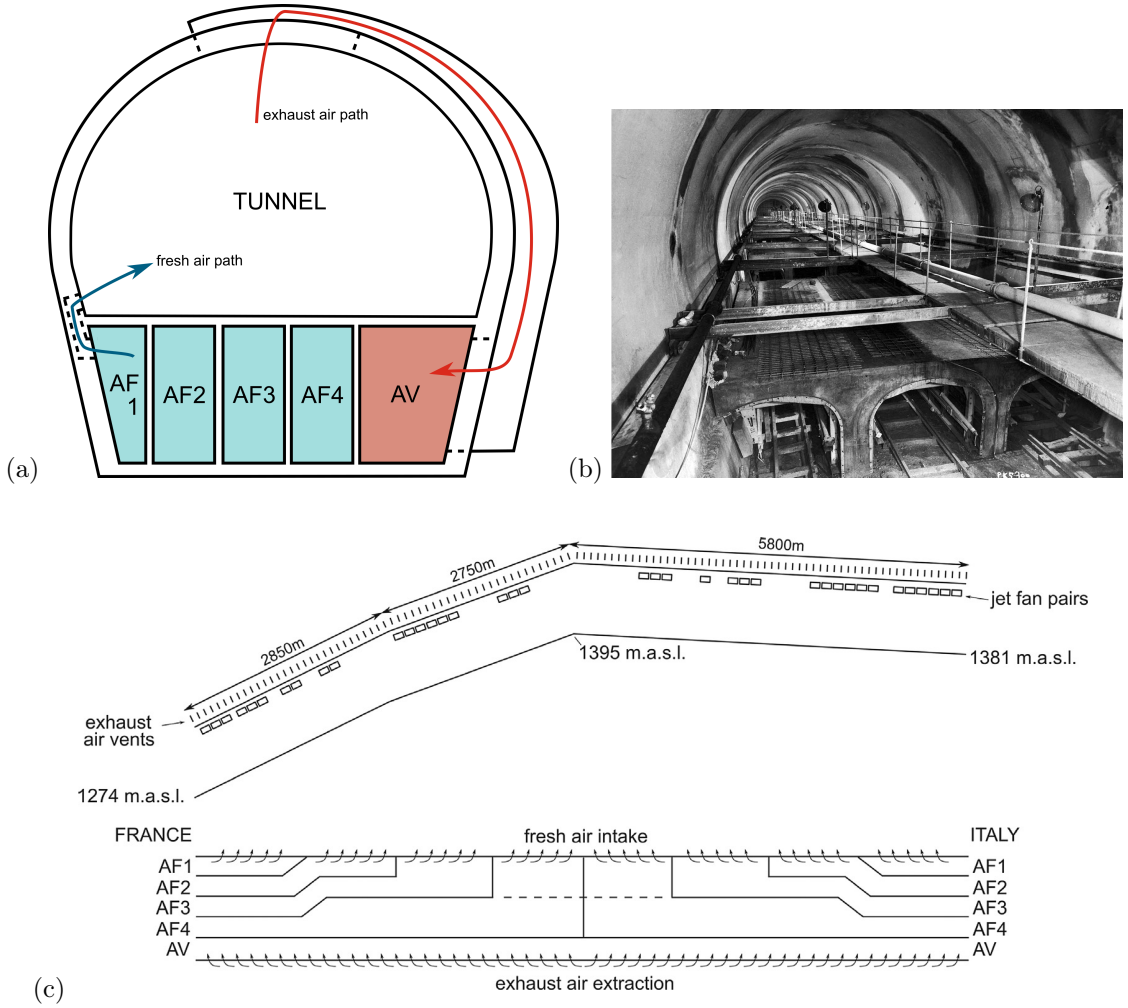

Figure 2.1: Various representations of the *Mont Blanc* tunnel ventilation system: (a) sketch of the transverse cross-section of the tunnel and underground ventilation channels with locations of fresh air and exhaust vents and indication of the corresponding flow paths; (b) photograph showing the tunnel construction with an insight of the underground channels (c) sketch of the longitudinal section of the tunnel (top view) and planform of the underground ventilation channels (bottom view).

Figure 2.2: Details of the *Mont Blanc* tunnel ventilation system: (left to right) interior of the ventilation station on the Italian side; underground fresh air channel; fresh air supply vents along the sidewalk; a pair of jet fans.

2.2 Ventilation system

The *Mont Blanc* tunnel emergency ventilation system is semi-transverse (or hybrid, or combined), and its main components are:

- a fresh air intake system;
- an exhaust air extraction system;
- a longitudinal air velocity control system;
- 37 pressurized safety shelters;
- sensors for the measurement of local air velocity, pollutants concentration, differential pressure between the shelters and the tunnel etc.;
- a control system capable of estimating the longitudinal velocity profile and managing different hazardous scenarios by governing fans activation.

2.2.1 Transverse ventilation system

Underground channels

Nine ventilation ducts, for both fresh air intake and exhaust air extraction, are located under the roadway (Figure 2.1). The exhaust air duct (also referred to as "AV" or "Channel 5") is the only one crossing continuously the whole tunnel length, and is located on the right side (from France to Italy). The AV channel is linked with the main tunnel by 116 adjustable vents (which can be either open or closed) located on the tunnel ceiling, approximately every 100 m. A fully open exhaust air vent – also called "*trap*" – has a cross section which is either 2.4 m^2 (for the 36 vents which are located in the proximity of stopping areas) or 3.4 m^2 (for the remaining ones).

The remaining eight ducts are in charge of supplying fresh air to the tunnel. All of them are connected to just a single side of the tunnel: four are connected to the Italian

side and four to the French side (see Figure 2.1). Each fresh air channel is composed of a "transfer" part and a "distribution" part. The channels don't have any connection to the main tunnel within their "transfer" part – which serves only as a link between the fresh air inlet and the "distribution" part. Vice-versa, the "distribution" part is linked to the main tunnel by means of small vents which are located at the sidewalk level every 10 m (see Figure 2.2) and have a cross-section of 0.06 m^2. Each fresh air channel is in charge of serving one eighth of the whole tunnel, so each "distribution" stretch has a length of approximately 1450 m.

Fresh air ventilation system

Concerning the fresh air intake system, a ventilation station is present at each end of the tunnel, and is in charge of supplying fresh air to the four ducts to which it is connected by means of centrifugal fans (Howden VRD1250/6011). Although each station feeds just four channels five fans have been provided, leaving one spare fan ready to replace one of the main fans in case of failure.

The fresh air intake system is also in charge of feeding fresh air to the 37 safety shelters, although the pressurization of the latter is further ensured by a set of auxiliary fans. Nonetheless it is crucial to keep the pressure in the fresh air ducts higher than the pressure in the tunnel, to avoid any recirculation: this guarantees the quality of the air provided by the fresh air ducts at any moment.

The regime of each fresh air fan is independent and can be adjusted in order to keep the related duct pressurized with respect to the tunnel: note that some of the fresh air channels include a very long transfer stretch and many section changes before their distribution part, thus the mechanical power required for a correct operation may be different for each channel.

The regimes of the fresh air fans are constantly adjusted according to the intensity and direction (if either one prevails) of the traffic and weather (which influences the pressure difference at the ends of the tunnel). In ordinary working conditions the aim of the fresh air system is to guarantee the quality of the air in the tunnel.

Exhaust air ventilation system

The air extraction duct is equipped with three centrifugal fans (Howden VRD1000/5021) at each end: two of these fans work in parallel, while the third is a spare fan which can quickly provide a backup in case of failure of one of the fans in charge. Four reversible axial fans (Howden D1713L1 1259 0.596), from now on called "*relais* fans" are also installed along the air extraction channel (at metric points: 2050, 4450, 6845, 9280) to help the quick depressurization of the extraction channel. All of these fans are generally activated only in case of emergency, and mostly work at maximum regime ($\sim$1000 rpm) to guarantee the maximum extraction flow-rate.

In case of emergency the extraction system is meant to guarantee the extraction of 150 m^3/s on a tunnel stretch of 600 m, centered on the fire event. In fact, the extraction of smoke along the tunnel stretch is ensured by the heavy depressurization of the extraction channel. The tunnel is put in communication with the depressurized channel by opening the seven extraction vents that are closer to the fire, while keeping closed all the remaining ones.

It has to be mentioned that the *relais* fans regime may be partialized in case the differential pressure between the main tunnel and the discharge side of the fan becomes negative, to prevent the risk of having the exhaust air leaking from the extraction duct to the tunnel through closed extraction vents (which are not air-tight even if closed). This working regime of the *relais* fans is called "*bridage*", in French language.

The most notable advantage of having the air extraction taking place at the ceiling level and the fresh air intake taking place at the floor level is the enhancement of smoke stratification. Therefore, a layer of breathable air, at least at ground level, should be available even in the tunnel stretch interested by the air extraction.

2.3 Axial jet fans

A longitudinal ventilation system is also present in the tunnel, and it is meant to assist the transverse ventilation system in case of strong pressure differences between the portals (the logic behind this feature will be clearer in Section 2.4.2).

A total of 38 axial jet fans couples are installed on the tunnel ceiling of the tunnel (see Figure 2.2). Such fans (Howden 710/330-10) are bi-directional and work at a fixed regime. The jet fans diameter is 80 cm and their nominal thrust is 600 N.

The axial jet fans have been the subject of an extensive study within a previous work from this same research group [75], which included both direct measurements in the proximity of the working fan and CFD simulations in order to determine the installation efficiency and their influence on the longitudinal flow within the tunnel. It has been proven that such fans do not significantly influence the pressure profile in the main tunnel; nonetheless, they do influence the air velocity on the whole tunnel by shifting the whole longitudinal profile upwards or downwards – according to their working directions.

2.4 Control system

Longitudinal velocity has a crucial influence on the diffusion of combustion products along the tunnel. Both tunnel and ventilation channels are equipped with several sensors, which provide information on the local values of the flow variables of the whole system. The control system also includes a software (called S.C.A.D.A., meaning Supervisory Control And Data Acquisition) capable of estimating on-the-fly the longitudinal velocity profile in the main tunnel, based on the measurements, and – in case of emergency – to manage the jet fans activation in order to control the shape of such profile.

2.4.1 Velocity profile estimation

The main variables measured by the system, which constitute the starting point for the estimation of the velocity profile, are:

- 20 velocity values within the main tunnel measured by anemometers located along the tunnel (covering its entire length);
- 8 flow rate values, measured at the start of transfer stretch of each fresh air channel;
- 4 flow rate values, measured at the end of the transfer stretch of the longest fresh air channels (AF3_FRA, AF4_FRA, AF3_ITA, AF4_ITA);

Figure 2.3: Detail of the installation of sensors in the ventilation channels.

- 2 flow rate values, measured at the ends of the vitiated air channel;
- 4 flow rate values, measured in the proximity of each *relais* fan;
- position of the opened extraction vents, if any.

All the flow rates are evaluated based on the pressure delta which ensues in a series of sensors (Debimo, KIMO®– Figure 2.3). Such differential pressure signals are converted and elaborated within dedicated control units (CP303, KIMO®), by an embedded software. For each 100 m tunnel stretch the SCADA software calculates:

- the flow rate entering the tunnel from the fresh air vents (assuming that the total flow rate measured in the channel is equally partitioned through the 1450 m tunnel stretch served by the channel);
- the flow rate leaving the tunnel through open extraction vents, if any;
- the total flow rate of the tunnel stretch, by algebraic sum of the previous two.

Since the flow rate entering (or leaving) a tunnel stretch from the vents represents the slope of the longitudinal velocity profile, the shape of such profile is already determined at this point. Then, the profile is shifted vertically – and eventually adjusted – to fit the velocity values measured by the anemometers.

2.4.2 Control logic

The longitudinal velocity profile is in general shaped as a broken line: the differences in terms of slopes between the different tunnel stretches is due to the air flow joining (or leaving) the main tunnel via fresh air (or extraction) vents. Hence, in case of normal working conditions, different segments are located in the vicinity of the distribution stretches of the eight fresh air channels.

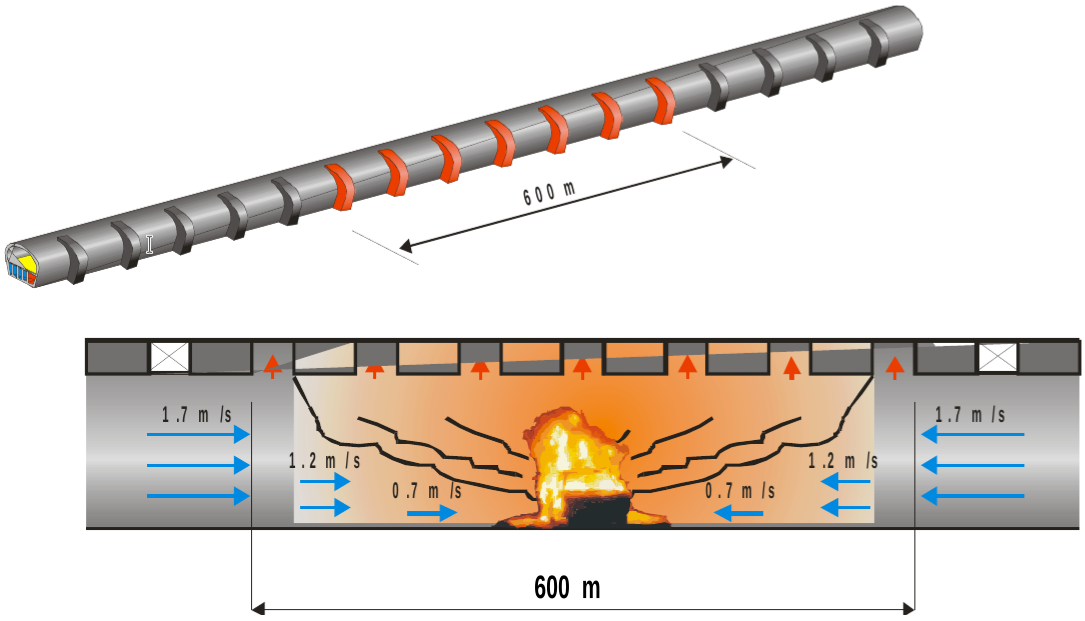

Figure 2.4: Example of successful smoke management, with null longitudinal velocity at the fire location.

In case of emergency ventilation the longitudinal velocity profile undergoes an abrupt change: a further segment is added in correspondance of the open extraction vents. The slope of such segment is steep, due to the high flow-rate (150 m^3/h) guaranteed by the extraction system, and obviously its slope is opposite with respect to the slopes induced by the fresh air intake.

The aim of the control logic is to reach null longitudinal velocity at the event location, therefore obtaining a local flow condition which resembles the one in Figure 2.4. The aforementioned shape features of the velocity profile in emergency working conditions are clearly suitable for this task, due to the abrupt change of velocity in the surroundings of the fire location. Nonetheless, the airflow in the tunnel is heavily conditioned by the pressure difference between the portals: the changes in such pressure difference entail a vertical translation of the whole velocity profile. This, in turn, can involve the whole profile to have negative (or positive) values – regardless of its shape.

The longitudinal ventilation, and its control system, has been included in order to tackle such an inconvenience: the velocity profile, within the limits dictated by the installed fans power, can be also shifted upwards or downwards by activating a number of jet fan couples.

Given the current velocity profile, and knowing the influence of an axial jet fan on the tunnel velocity, the prediction of the proper number of jet fans that need to be activated in order to obtain null velocity on the fire location can appear trivial. Nonetheless, the effect of turning on a jet fan is not instantaneous: since the goal is to obtain the desired profile in the shortest possible time, the best solution is certainly not to just turn on the exact number of fans that would produce the desired profile once that steady conditions are reached.

Indeed a quicker way to reach the desired condition would be to initially turn on more fans than what would be reqired in steady conditions, so as to speed up the transient, and then turn off (or even switch the direction of) some fans to avoid overshooting. Moreover,

the operation of the axial fans and their controller often starts before the "emergency condition profile" is established, because the depressurization of the exhaust air channel also goes through a long transient.

The relative complexity of the task, and the need to adapt the response of the controller as quickly as the influence of its action is observable on the system, favoured the choice of a PID (Proportional, Integrative, Derivative) controller. The output of the PID represents the number of jet fans which need to be turned on, and its sign represents the direction (following the usual sign convention where FRA $\rightarrow$ ITA is considered as positive). The input of the PID controller is provided by the longitudinal air velocity at the fire location.

2.4.3 Fire management examples

In Figure 2.5 an example of the variation of the tunnel longitudinal velocity profile due to the activation of the emergency ventilation system is reported. In the first frame (a) the velocity profile shape is the one typical of ordinary working conditions: the profile is essentially monotonous, with slope changes due only to the fact that in different tunnel stretches fresh air is fed by different channels (and fans, which can have different working regimes). The single segments, expecially those close to the portals, are not strictly straight because of density variations due to temperature variations and realistically non-uniform distribution of local flow rates. Indeed, the tunnel and channel walls are at about 25°C, while the outside air enters the domain at a temperature which is in general different from such value. The outside temperature differs at the two portals and changes according to the season and weather; the reference value which is often adopted is 5°C . At any time, most of the air contained in the domain has reached 25° C since the air velocity is small if compared with the domain size. Nonetheless, for the sections which are closest to the entrance, temperature gradients are relevant enough to influence the velocity profile.

In the second frame (b), all the positive slopes are decreased: under emergency conditions, fresh air fans regimes are brought to a minimum. Such regimes depend on the pressure difference between the portals, and should be high enough to keep the pressure in the fresh air channels higher than the pressure in the main tunnel – therefore avoiding backflow.

It is also evident that the extraction gates are open around the fire location, and the exhaust air channel is already depressurized. Indeed, it is easy to notice that the average slope around the fire location has changed to negative values: this means that, within that tunnel stretch, the air is starting to be extracted through the vents, and the exiting airflow is already prevailing on the entering airflow. Zooming in, it can be noticed how such part of the velocity profile presents abrupt steps: this is due to the spacing of the extraction vents, which is about 10 times larger than that of fresh air vents. The PID control has already turned on a significant number of jet-fans, but their effect on the velocity profile is still very weak.

Through the third (c) fourth (d) and fifth (e) frames, the average slope around the fire location is increasing in absolute value, since the regime of the extraction fans is still increasing and the pressure in the exhaust air channel is therefore still decreasing. Also, it is noticeable how the axial fans are starting to have an effect on the velocity profile: it is being signigicantly shifted upwards. The velocity value at the fire location is not zero yet, but the PID controller is already planning to turn some jet fans off.

In the last frame (f) we can notice that the extraction fans have reached their regime,

as the slope in extraction stretch is not increasing anymore. On the other hand the whole profile has been shifted further upwards, and now the velocity is zero at the event location. The PID controller is suggesting to turn off more fans, in order to contain overshooting phoenomena.

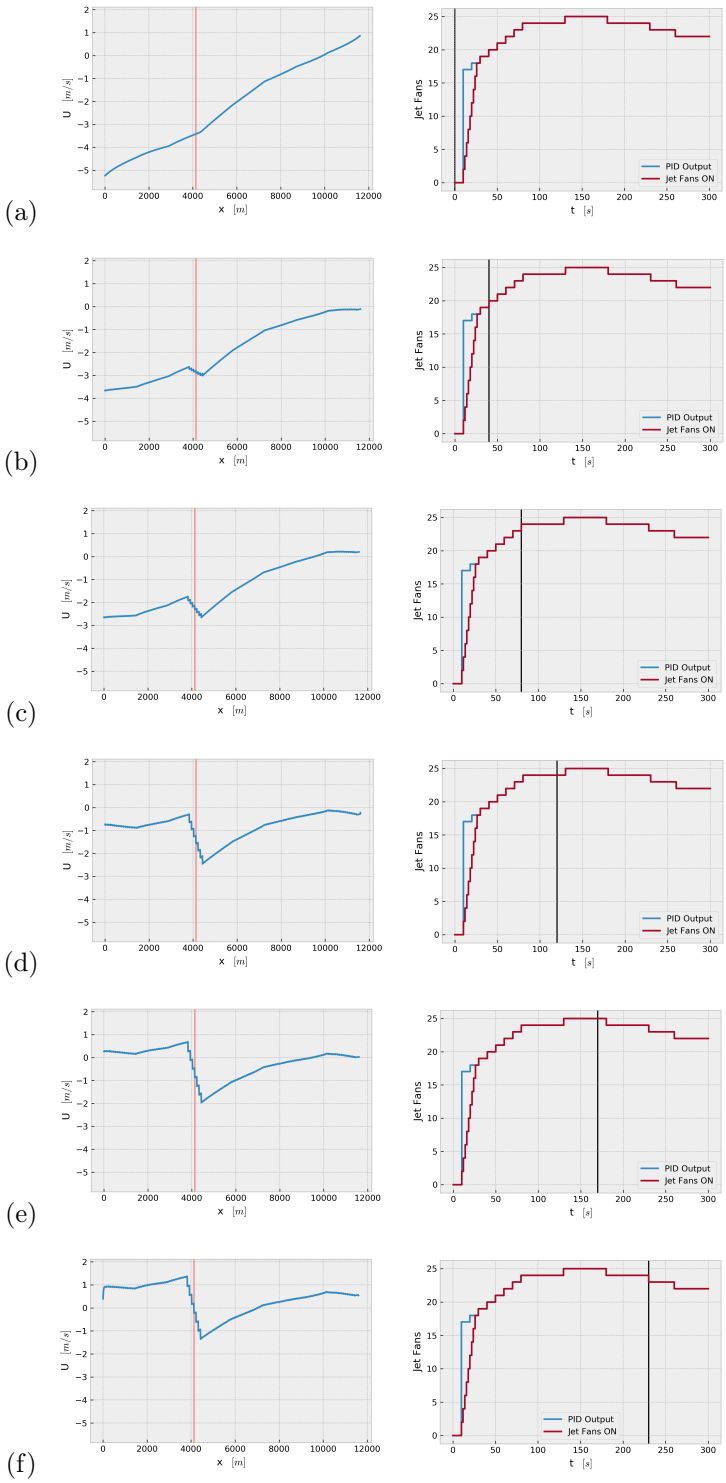

Figure 2.5: Example of the action of a PID controller (from numerical simulation), represented by 6 subsequent frames. The plot on the left shows the tunnel longitudinal velocity profile (with a red vertical streak highlighting the fire location), while the plot on the right represents the PID action through a time frame of 300 s (with the vertical line indicating current time).

Chapter 3

Numerical model

3.1 Introduction

The present chapter is devoted to the detailed description of the numerical method, starting from the set of governing differential balance equations. These are then discretized based on a graph representation of the domain, and conveniently expressed in matrix form. To this aim, a matrix form of first order interpolation operators is provided. Then, the solution algorithm is deviced and illustrated.

In the subsequent sections a few insights on the treatment of source/sink terms are provided in support of the numerical method, with a focus on the specific application on the *Mont Blanc* tunnel. Moreover, a management logic for the sequence of events that need to be accounted for while performing a transient simulation is explained. Lastly, some insights and examples regarding the object-oriented implementation of the numerical model are provided.

3.2 Governing equations

The governing equations forming the basis on which the present numerical model has been developed are:

- mass conservation;
- momentum conservation;
- energy conservation.

Starting with mass conservation, the continuity equation can be expressed as follows:

$$\frac{\partial \rho}{\partial t} + \nabla \cdot (\rho \boldsymbol{u}) = 0 \tag{3.2.1}$$

Both variables in the equation (3.2.1), density (ρ, scalar) and velocity ($\boldsymbol{u}$, $\mathbb{R}^3$ vector) are functions of both space and time.

The following equation is the differential expression of momentum conservation, written in Eulerian form:

$$\rho \frac{\partial \boldsymbol{u}}{\partial t} + \rho \boldsymbol{u} \cdot \nabla \boldsymbol{u} = -\nabla p + \nabla \cdot \boldsymbol{T} + \rho \boldsymbol{g} + \boldsymbol{\sigma}_M \tag{3.2.2}$$

In the equation (3.2.2) some further variables are introduced. Pressure (p, scalar) is also a function of time and space. Gravity acceleration ($\boldsymbol{g}$, $\mathbb{R}^3$ array) is employed to take into account the action of buoyancy. The source term ($\boldsymbol{\sigma}_M$, scalar) represents the effect of momentum sources or sinks.

Concerning the stress tensor ($\boldsymbol{T}$, $\mathbb{R}^{3,3}$ matrix), it represents momentum dissipation due to viscous interactions within the fluid. The complete explaination of such term will be omitted as it is beyond the scope of this work, see [77] for details. Such term will be soon replaced by a simpler one within the next section.

Under the assumption of incompressible flow, and neglecting the term due to viscous dissipation, the thermal energy equation can be written as:

$$\rho c \frac{\partial T}{\partial t} + \rho c \boldsymbol{u} \cdot \nabla T = \nabla \cdot (\lambda_T \nabla T) + \sigma_E \tag{3.2.3}$$

In the Equation (3.2.3), thermal conductivity (λ_T, scalar) and specific heat (c, scalar) depend on the fluid, along with its local pressure and temperature. The source term (σ_E, scalar) represents the effect of heat sources or sinks.

3.3 Simplifying assumptions

The system composed by the aforementioned differential equations is capable of describing thoroughly and univocally the motion of a continuous, non-isothermal fluid in space and time. Nonetheless, only a few analytical solutions to these equations exist, and they all refer to very simple geometries and flows, of little interest for this case.

Approximate solutions, which can be three dimensional and unsteady, can be obtained numerically. However, since the scope of the present study is to provide a quick and lightweight (although reliable) model, the equations (3.2.1), (3.2.2), (3.2.3) must be simplified.

In order to bring the governing equations to a simplified form, the following assumptions are made:

(i) as the air velocity in the tunnel is proven to be significantly lower than the speed of sound [14], the flow can be considered incompressible;

(ii) however, in such systems, density variations as a function of temperature are typically not negligible [78]; hence, air density is determined by means of an incompressible ideal gas law:

$$\rho = \frac{p_{ref}}{RT} \tag{3.3.1}$$

In Equation (3.3.1), p_{ref} is a reference pressure value, suitably chosen so as to represent the average absolute pressure in the system.

(iii) since the physical system is characterized by a very high aspect ratio, all the variables can be considered as dependent from a single spatial coordinate, which will be from now on called x;

(iv) the term representing viscous dissipation in the momentum balance equation is replaced by a loss term σ_{loss} depending only on velocity u;

(v) likewise, momentum sources such as fans can be represented by a source term σ_{fan} depending only on velocity u;

(vi) the diffusive term of the thermal energy equation along x is assumed as irrelevant with respect to the convective term and can be omitted; while wall heat transfer and internal heat generation are expressed by the source term σ_E.

Similar simplifying assumptions have been taken for many of the models reported in the literature review (see Section 1.3.1). Colella *et al.* employed a 1D model based on the same assumptions as a part of a multiscale model, and proved its validity against a wide variety of experimental data [65, 66, 67, 68].

The transition of space coordinates from 3D to 1D allows for significant simplifications to the equation. Continuity equation can be rewritten as:

$$\frac{\partial \rho}{\partial t} + \frac{\partial (\rho u)}{\partial x} = 0 \tag{3.3.2}$$

Before rewriting the momentum balance equation in a 1D form it is useful to express the gravitational term as the gradient of the gravitational potential:

$$\rho \boldsymbol{g} = -\nabla \left[\rho g (z - z_0)\right] \tag{3.3.3}$$

Hence, by replacing the gravitational term 3.3.3 within Equation (3.2.2) and subsequently simplifying to 1D:

$$\rho \frac{\partial u}{\partial t} + \rho u \frac{\partial u}{\partial x} = -\frac{\partial p}{\partial x} - \frac{\partial}{\partial x}\left[\rho g (z - z_0)\right] - \sigma_{loss} + \sigma_{fan} \tag{3.3.4}$$

It is worth to highlight that the stress tensor $\boldsymbol{T}$ loses its meaning in a 1D context, and it is therefore replaced by σ_{loss}. Such term represents the momentum loss due to friction and will be further explained within the next sections.

All the derivatives in space in the Equation (3.3.4) may be grouped:

$$\rho \frac{\partial u}{\partial t} + \frac{\partial}{\partial x}\left[\frac{\rho u^2}{2} + p + \rho g (z - z_0)\right] = -\sigma_{loss} + \sigma_{fan} \tag{3.3.5}$$

One can then define the total pressure P as the sum of the kinetic term, the pressure term and the gravitational term:

$$P = \frac{\rho u^2}{2} + p + \rho \ g \left(z - z_0\right) \tag{3.3.6}$$

Equation (3.3.5) can be rewritten in a more compact form:

$$\rho \frac{\partial u}{\partial t} + \frac{\partial P}{\partial x} = -\sigma_{loss} + \sigma_{fan} \tag{3.3.7}$$

Concerning the energy conservation equation (3.2.3), it can also be expressed in function of one spatial coordinate only:

$$\rho c \frac{\partial T}{\partial t} + \rho c u \frac{\partial T}{\partial x} = \lambda_T \frac{\partial^2 T}{\partial x^2} + \sigma_E \tag{3.3.8}$$

By applying the last simplifying assumption, i.e. removing the diffusive term, energy conservation equation reduces to:

$$\rho c \frac{\partial T}{\partial t} + \rho c u \frac{\partial T}{\partial x} = \sigma_E \tag{3.3.9}$$

Resuming the governing equations that have been identified and simplified so far:

$$\frac{\partial \rho}{\partial t} + \frac{\partial (\rho u)}{\partial x} = 0 \tag{3.3.10}$$

$$\rho \frac{\partial u}{\partial t} + \frac{\partial P}{\partial x} = -\sigma_{loss} + \sigma_{fan} \tag{3.3.11}$$

$$\rho c \frac{\partial T}{\partial t} + \rho c u \frac{\partial T}{\partial x} = \sigma_E \tag{3.3.12}$$

$$\rho = \frac{p_{ref}}{RT} \tag{3.3.13}$$

3.4 Boundary conditions

In order to be able to solve the differential equations which were obtained, initial and boundary conditions must be provided. Introducing $t_0 = 0$ as the starting time of the simulation, initial conditions for the three main fields can be defined as follows:

$$P(0, x) = P_0(x) \tag{3.4.1}$$

$$u(0, x) = u_0(x) \tag{3.4.2}$$

$$T(0, x) = T_0(x) \tag{3.4.3}$$

$$\tag{3.4.4}$$

Density is omitted here as it depends directly on temperature as in equation (3.3.1).

Concerning boundary conditions, velocity (u) or pressure (p) at the domain boundary are more likely to be known than total pressure (P), so the variables on which the boundary conditions are defined have been chosen accordingly. Since pressure gradient and velocity are related (as in Eq. 3.3.5), they are to be defined interdependently. If the velocity at one boundary is known, the pressure gradient at such boundary should be considered as zero:

$$u = \bar{u}, \quad \frac{\partial p}{\partial x} = 0 \tag{3.4.5}$$

Vice-versa if the pressure is known, it is common to set the velocity gradient as zero:

$$p = \bar{p}, \quad \frac{\partial u}{\partial x} = 0 \tag{3.4.6}$$

Temperature can be also set to a specific value on a boundary, if it is known:

$$T = \bar{T} \tag{3.4.7}$$

Otherwise its derivative can be fixed to a value, with the effect of fixing the heat exchanged through such boundary. As an example:

$$\frac{\partial T}{\partial x} = 0 \tag{3.4.8}$$

3.5 Topological representation

As it comes to conceiving a light-weight numerical model, hence reducing the domain complexity, the high aspect ratio of the tunnel and ventilation channels already suggests the possibility of representing the system by means of an oriented graph [76]. This kind of representation offers a series of advantages for this particular case.

First of all, two dimensions (the ones orthogonal to the tunnel axis) can be neglected and considered them just as branch properties. This allows for the discretization of the domain along just one dimension, thus reducing considerably the number of elements of the discretized domain with respect to a full 3D mesh.

Moreover, a graph model becomes very convenient if the represented network is highly interconnected. Indeed, graph theory provides an ideal tool to keep track of the connections between elements in the system equations, i.e. the incidence matrix [76] $\mathbf{A}$. This matrix has a number of rows equal to the number of nodes of the network it represents, and a number of columns equal to the number of branches. Its elements are meant to represent the connection between a node (determined by i, row index) and a branch (determined by j, column index), and have three possible values: 1 if the i-th node is the j-th branch starting node, -1 if the i-th node is the j-th branch end node and 0 otherwise. This particular way to summarise connectivity significantly facilitates the task of writing the discretized governing equations of the whole system in matrix form.

To translate the current system to a directional graph the whole system is subdivided into control volumes, that will coincide with the branches of the directed graph. Each branch, in turn, is connected to two nodes. Contrarily to branches, nodes are not characterized by a volume nor a mass per se, but merely represent interfaces of zero volume among concurrent branches. However, in a Finite Volume framework, a staggered mesh can be defined such that the domain associated to the i-th node is composed by half of all branches attached to such node (see Fig. 3.1). In order to store information about those entities it is then sufficient to save an array containing all the volumes which are associated to the branches. Being node volumes essentially linear combinations of branch volumes, and being the coefficients of such combination only dependent on the graph connectivity, node volumes are easily calculated from branch volumes using the incidence matrix $\mathbf{A}$.

It is then possible to assign different variables to node and branch domains. State variables such as temperature, total (or static) pressure, density, specific heat are defined on nodes; flow variables (mass flow rates and thus velocities) are defined on branches. Each branch also possesses specific geometric, thermodynamic and fluid-dynamic properties (length, section area, wall temperature, mechanical sinks and sources, heat transfer coefficients). Just like with the volumes, it is possible to define operators capable of projecting on nodes a field defined on branches (and vice-versa). While an in-depth explanation on such operators can be found in Section 3.6.1, it is for now sufficient to state that the incidence matrix $\mathbf{A}$ constitutes a powerful tool for writing such operators in matrix form.

It is also worth to anticipate that the definition of the domain of interest as two different sets of connected objects facilitates the staggering of the domains of integration of u (branches), and P, ρ, T (nodes), providing an ideal support for a Finite Volume discretiza-

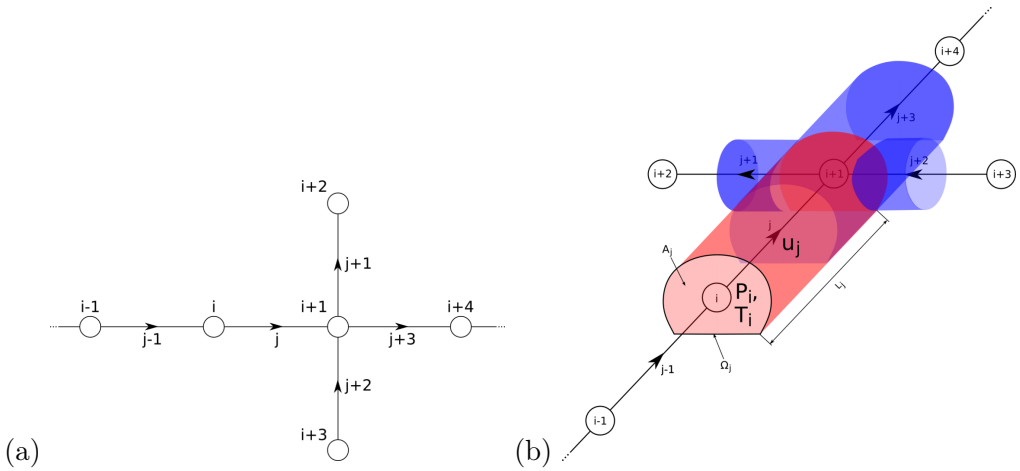

Figure 3.1: Example of basic graph: (a) a very simple network, (b) control volumes associated to the j-th branch (red) and *(i+1)*-th node (blue) of such network

tion of the governing equations.

The 1D network that has been designed to represent the *Mont Blanc* tunnel and its ventilation system is composed of $n_n = 2639$ nodes and $n_b = 3904$ branches. As it can be noticed in Figure 3.2, it is hard to plot a readable overall view of the graph, due to the different scales of some of its features: the spacing between fresh air vents (each of those is represented by a branch connecting the main tunnel with the ventilation channel of competence) is just 10 m, while the whole tunnel has a length of 11610 m.

The refinement of the partition used for the main tunnel (and for the *distribution* stretch of the fresh air channels) is a direct consequence of the spacing between fresh air vents: a space delta of 10 m or less between the tunnel nodes is required for the correct representation of the latter. The same concept applies to the exhaust air channel, in which the nodes have been placed in correspondence of each extraction vent (the spacing is not as regular, but can be considered to be around 100 m).

As a consequence, the *transfer* stretches of the fresh air channels are the only ones to whom a minimum partition delta is not dictated by the presence of connections to other branches. Some of these stretches are several kilometers long and could be theoretically represented by just one branch. In order to make the network suitable for the application of low-order interpolation schemes e.g. upwind (for whom an excessively coarse partition is undesirable as it would critically enhance numerical diffusion), those parts have been arbitrarily partitioned by adding a node every 100 m.

3.5.1 Network features

All kinds of features (geometric features, momentum heat and mass sources, but also state variables) that need to be associated with network elements are stored in arrays. Depending on which kind of element these features belong to, the array they constitute will have either length n_n or n_b (for nodes and branches, respectively).

The geometric features of the network are defined on branches. Therefore, the following arrays of length n_b are defined:

- $\boldsymbol{L}$ is the array which contains the length of each branch of the network;

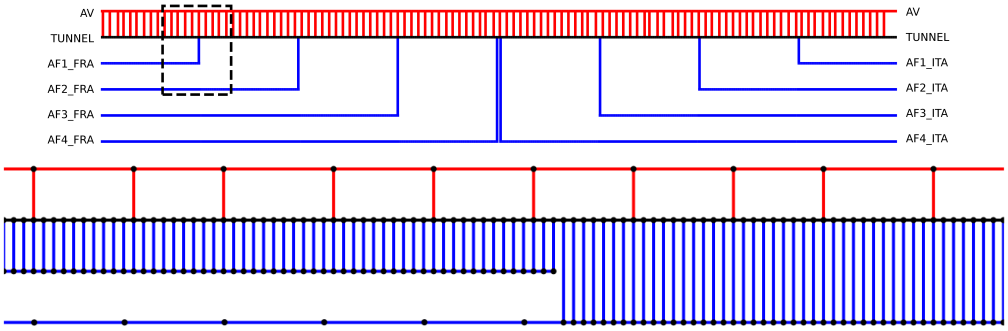

Figure 3.2: Representation of the TMB tunnel graph: (a) a simplified overall view, (b) a detailed representation of a portion of (a).

- $\boldsymbol{S}$ is the array which contains the cross-section area of each branch of the network;
- $\boldsymbol{D_h}$ is the array which contains the hydraulic diameter of each branch of the network;
- $\boldsymbol{V}$ represents the volume of each branch and it is defined as $\boldsymbol{L} * \boldsymbol{S}$.

The symbol $*$ has been employed to indicate *element wise product*. When applied between one dimensional arrays, like $\boldsymbol{\rho} * \boldsymbol{c}_p * \boldsymbol{V}_n$ in the first term of the second member, the result is an array that have as elements the products between the corresponding elements of the input arrays.

It is often necessary to access the volume feature of nodes elements. As previously mentioned, the volume of a node is represented by the sum of the semi-volumes of all the adjacent branches; the array of nodal volumes $\boldsymbol{V}_n$ can therefore be defined as:

$$\boldsymbol{V}_n = \frac{1}{2}|\boldsymbol{A}| \cdot \boldsymbol{V} \tag{3.5.1}$$

3.6 Time and space discretization

The governing equations previously introduced, complete with initial and boundary conditions, must be rewritten in discrete form in both space and time in order to be solved numerically.

In the present work, the Finite Volume method has been chosen. Such method is based on the partition of the whole domain in a number of conveniently small subdomains, within which the value of variables is considered as homogeneous. On each of the volumes it is therefore possible to integrate mass, momentum and energy balance.

The topological representation described in the previous Section 3.5 constitutes an ideal support for the calculation. The *staggering* between the two grids, formed by the node volumes and the branch volumes respectively, is a very useful (and frequently adopted) feature. Indeed, integrating velocity on a different domain with respect to pressure and temperature avoids the onset of numerical oscillations in the pressure field – a typical issue when employing a segregated algorithm.

The time coordinate t also needs to be partitioned into discrete intervals. For this reason, the time continuum is approximated with a series of subsequent time-steps Δt.

Assuming that the values of the state variables are known for the time t_n, their value at time t_{n+1} can be calculated by integrating the governing equations on $\Delta t = (t_{n+1} - t_n)$.

Continuity equation (3.3.10) is integrated on the i-th node and timestep $(t_{n+1} - t_n)$. After the application of the Gauss theorem – omitted here for the sake of brevity – it reads:

$$\int_{t_n}^{t_{n+1}} \int_{V_i} \frac{\partial \rho}{\partial t} dV dt + \int_{t_n}^{t_{n+1}} \int_{S_i} \rho u dS dt = 0 \tag{3.6.1}$$

Momentum conservation equation (3.3.11) is integrated on branches instead. Its expression on the j-th branch reads:

$$\int_{t_n}^{t_{n+1}} \int_{V_j} \rho \frac{\partial u}{\partial t} dV dt + \int_{t_n}^{t_{n+1}} \int_{S_j} P dS dt = \int_{t_n}^{t_{n+1}} \int_{V_j} (\sigma_{fan} - \sigma_{loss})\, dV dt \tag{3.6.2}$$

Concerning energy conservation equation (3.3.12), it must also be integrated on nodes:

$$\int_{t_n}^{t_{n+1}} \int_{V_i} \rho c \frac{\partial T}{\partial t} dV dt + \int_{t_n}^{t_{n+1}} \int_{S_i} \rho c u T dS dt = \int_{t_n}^{t_{n+1}} \int_{V_i} \sigma_E dV dt \tag{3.6.3}$$

3.6.1 Interpolation schemes

In order to discretize the governing equations, it will be often necessary to assign values of a variable on fields where such variable is not defined. As an example, density values for the system branches may be required – although density field is only defined on nodes.

Therefore, it is worth to introduce some schemes which will be used for interpolating values from nodes to branches, and vice-versa. The operators for accomplishing such task can be conveniently expressed in matrix form. In the following examples:

$\boldsymbol{M}_{n\to b}$ will express the operator nodes to branches, of size $n_b \times n_n$;

$\boldsymbol{M}_{b\to n}$ will express the operator nodes to branches $n_n \times n_b$;

$\boldsymbol{h}_n$, $\boldsymbol{k}_n$ will express generic arrays defined on nodes, of length n_n;

$\boldsymbol{h}_b$, $\boldsymbol{k}_b$ will express generic arrays defined on branches, of length n_b.

The operators are defined so as to work as follows:

$$\boldsymbol{h}_b = \boldsymbol{M}_{n\to b} \cdot \boldsymbol{h}_n \tag{3.6.4}$$

$$\boldsymbol{k}_n = \boldsymbol{M}_{b\to n} \cdot \boldsymbol{k}_b \tag{3.6.5}$$

First, it may be noticed that the incidence matrix $\boldsymbol{A}$ may already constitute an operator for casting an array defined on branches (branches array) into an array defined on nodes (nodes array). Indeed, any $n_n \times n_b$ sized matrix could cast a branch array into a properly sized node array: the difference between the following options is the logic behind the mapping which they perform.

3.6.2 Incidence matrix and its transpose

Nodes to branches

$$\boldsymbol{M}_{n\to b} = \boldsymbol{A}^T \tag{3.6.6}$$

Keeping in mind the definition of incidence matrix previously given in Section 3.5, let's now investigate the effect of the scalar product between its transpose and a field defined on nodes. A row of $\boldsymbol{A}^T$ represents the connectivity of a branch. Therefore, only two elements on such row will be non-null:

- one, located the column corresponding to the starting node of the branch, will have value equal to 1;
- the other, located the column corresponding to the ending node of the branch, will have value equal to -1;

Therefore, analyzing the generic j-th element of the array resulting from the casting $\boldsymbol{h}_b = \boldsymbol{A}^T \cdot \boldsymbol{h}_n$, one has:

$$h_{b,j} = h_{n,start} - h_{n,end} \tag{3.6.7}$$

This operator will be particularly useful in the momentum conservation equation, as it will provide a very compact form for writing the pressure differences between the ends of each branch.

Branches to nodes

$$\boldsymbol{M}_{b\to n} = \boldsymbol{A} \tag{3.6.8}$$

The incidence matrix itself constitutes an useful operator for the management of nodal fluxes.

A row of $\boldsymbol{A}$ represents the connectivity of a node. Therefore, it will contain at least one (for boundary nodes) non-null element:

- the elements located the columns corresponding to branches that are exiting the node will have value equal to 1;
- the elements located the columns corresponding to branches that are entering the node will have value equal to -1;

Therefore, analyzing the generic i-th element of the array resulting from the casting $\boldsymbol{k}_n = \boldsymbol{A} \cdot \boldsymbol{k}_b$:

$$k_{n,i} = \sum_{out} k_{n,j} - \sum_{in} k_{n,j} \tag{3.6.9}$$

This operator will be particularly useful in all the cases (e.g. mass conservation equation) in which an algebraic sum between fluxes entering/exiting each node is needed.

3.6.3 Central differences

Nodes to branches

$$\boldsymbol{M}_{n\to b} = \frac{1}{2}\,|\boldsymbol{A}^T| \tag{3.6.10}$$

The central differences scheme simply calculates the value of a variable on a branch as the average of the values of such variable on the two nodes which are connected to such branch.

It is trivial to check the definition of the j-th element of the array after the casting:

$$h_{b,j} = \frac{1}{2}(h_{n,start} + h_{n,end}) \tag{3.6.11}$$

Branches to nodes

$$\boldsymbol{M}_{b\to n} = \frac{1}{2}\,|\boldsymbol{A}| \tag{3.6.12}$$

The casting from a branch field to a node field can be seen as partitioning a feature of each branch between the adjacent nodes: central differences performs an equal partition, that doesn't take into account flow condition on a branch. Each node will therefore receive one half of the values of each adjacent branch.

Again, it is trivial to check the definition of the i-th element of the array after the casting:

$$k_{n,i} = \frac{1}{2}(\sum_{connected} k_b) \tag{3.6.13}$$

3.6.4 Upwind

For numerical stability reasons, the central differences scheme may not be a choice for writing the balance equation of a transported variable in the problem of interest, especially if the advective transport prevails on the diffusive transport (this is the case of *Mont Blanc* tunnel).

The upwind scheme, while still having a very simple formulation, is able to take into account the actual direction of the flow through the branches. In particular, it basically enforces the transport of the variables following the flow direction as the only criterion.

Therefore, as an example, a branch will adopt the variable value from the node which is "upwind" with respect to the flow within such branch.

For this reason, although the accuracy is only first order (on the basis of the Taylor series truncation error) and it can cause a certain degree of numerical diffusion, the upwind method will be widely adopted within the following sections.

Nodes to branches

$$\boldsymbol{M}_{n\to b} = \frac{1}{2}\left[|\boldsymbol{A}^T| + \left(\boldsymbol{A}\,\frac{\boldsymbol{u}}{|\boldsymbol{u}|}\right)^T\right] \tag{3.6.14}$$

Analyzing the definition of the upwind $n \to b$ operator given in Equation (3.6.14), it is easy to acknowledge that the resulting matrix is composed only by 1 and 0 values. In particular, non-null values will be located where the condition $(\boldsymbol{u}\,\boldsymbol{A})^T > 0$ is respected. A

generic row, representing the connectivity of a branch, will therefore have only one element equal to 1, and this will correspond to the node which is upwind with respect to the flow direction within the branch.

Defining the j-th element of the array after the casting:

$$h_{b,j} = h_{n,upwind} \tag{3.6.15}$$

Branches to nodes

$$\boldsymbol{M}_{b\to n} = \frac{1}{2}\left(|\boldsymbol{A}^T| - \boldsymbol{A}\,\frac{\boldsymbol{u}}{|\boldsymbol{u}|}\right) \tag{3.6.16}$$

On the other hand, analyzing the definition of the upwind $b \to n$ operator given in Equation (3.6.16), it is still true that the matrix is composed only by 1 and 0 values. The difference with the previous operator is that non-null values will be located where the condition $\boldsymbol{u}\,\boldsymbol{A} < 0$ is respected.

A generic row, representing the connectivity of a node will therefore a number (zero is also possible) of 1 elements according to the number of adjacent branches in which the flow is directed towards the node.

This roughly means that the entire "contribution" of each branch is summed with other contributions in the downwind node only, so - differently from central differences - the node which is upwind with respect to the branch won't get any contribution from the branch.

Defining the i-th element of the array after the casting:

$$k_{n,i} = (\sum_{upwind} k_b) \tag{3.6.17}$$

3.6.5 Discrete equations

The integration of Equations (3.6.1), (3.6.2), (3.6.3), which leads to a discrete form that can be solved with iterative calculations, is based on further assumptions:

- the state variables values are uniform within each control volume;
- the state variables values are uniform on the interfaces between volumes;
- convective transport of mass, momentum and energy takes place only on the inlet and outlet surfaces (this point is included in the 1D flow assumption which was previously made);
- the time-integration of all the terms which only depend on space is performed *implicitly*: this means that, aside for the time-derivative term, each variable in the equation will be replaced by its value at time t_{n+1} (which is indeed the unknown value, and is to be determined).

Continuity equation (3.6.1) can be therefore rewritten for the i-th node as:

$$\frac{(\rho_{i,n+1} - \rho_{i,n})}{\Delta t} V_i - \sum_j a_{ij} S_j \left(\rho_j u_j\right)_{n+1} = 0 \tag{3.6.18}$$

The employment of the corresponding element ($a_{i,j}$) of the incidence matrix (characterized in Section 3.5) is useful for accounting the fluxes entering and exiting the control volume through its two end faces.

It is worth to point out that, although the equation is discretized on nodes, when calculating the flux through the volume interfaces the density value at the interface (ρ_j) is required. Since the interface between two adjacent nodes is located at the center of the branch which connects the two, and density field is only defined on nodes, an interpolation scheme is needed. For this instance of the numerical model, the *upwind* scheme was chosen.

The discretization is then applied to the momentum conservation equation (3.6.2), and both members are divided for S_j. For the j-th branch we obtain:

$$\rho_{j,n+1}\frac{(u_{j,n+1}-u_{j,n})}{\Delta t}L_j+\sum_i a_{ij}P_{i,n+1}=\left(\sigma_{fan,j}-\sigma_{loss,j}\right)_{n+1}L_j \tag{3.6.19}$$

It is more convenient to express now the source and sink terms at the second member in terms of total pressure difference:

$$\sigma_{fan,j}=\frac{\Delta P_{fan,j}}{L_j} \tag{3.6.20}$$

$$\sigma_{loss,j}=\frac{\Delta P_{loss,j}}{L_j} \tag{3.6.21}$$

Equation (3.6.19) may be therefore rewritten as:

$$\rho_{j,n+1}\frac{(u_{j,n+1}-u_{j,n})}{\Delta t}L_j+\sum_i a_{ij}P_{i,n+1}=\left(\Delta P_{fan,j}-\Delta P_{loss,j}\right)_{n+1} \tag{3.6.22}$$

A thorough description on the representation of source and sink terms will be provided in Section 3.9, for now it is sufficient to mention that they might depend on local velocity value and/or its square.

Concerning the application of boundary equations to the system formed by equations of the kind of 3.6.18 and 3.6.19, they theoretically concern a boundary node (as a boundary branch can not exist for how the graph has been defined). Since a node is an entity on which the velocity is not defined – therefore adding an equation of the form $u_i=\bar{u}_i, \quad \forall i\in I_{bu}$ would not make sense – it has been chosen to take into account conditions of this type by adding a source term in the continuity equation (3.6.18) of the concerned node. This will be fully explained in the next section.

On the other hand, if the pressure is known on boundary, such condition can be accounted by assigning to such nodes an equation of the form:

$$P_i=\frac{\rho_i u_i^2}{2}+\bar{p}_i+\rho g(z_i-z_o) \qquad \forall i\in I_{bp} \tag{3.6.23}$$

Note that the term u_i in this case is defined as:

$$u_i=\sum_j a_{ij}u_j \tag{3.6.24}$$

If i identifies a boundary node, the i-th row of the incidence matrix will contain only one non-null element. This implies that applying the equation (3.6.24) imposes that the velocity

value which is employed for calculating dynamic pressure on node i must correspond to the velocity value of the only concurrent branch.

The discretized form of energy conservation equation (3.6.3) is:

$$\rho c \frac{(T_{i,n+1} - T_{i,n})}{\Delta t} + \frac{1}{V_i} \sum_j a_{ij} \phi_{j,n+1} = \frac{\sigma_{E,i,n+1}}{V_i} \tag{3.6.25}$$

The heat flux through a branch is defined as $\phi_j = \rho_j c_j S_j u_j T_j$, where T_j, ρ_j, c_j are values which are naturally defined on nodes, and are therefore interpolated on the j-th branch using the *upwind* scheme.

Concerning boundary conditions in terms of temperature, they have to be imposed on the whole boundary node set $I_b = I_{bu} \cup I_{bp}$. For each boundary node, the temperature has to be imposed if the mass flow is entering the domain through such node. On the other hand, in case the mass flow is exiting the domain, it is important to set the temperature gradient to zero on such node. Such conditions can be compacted within just one expression:

$$T_i = \frac{1}{2} \sum_j \left[|a_{ij}| (\bar{T}_i + T_j) + a_{ij} \frac{u_j}{|u_j|} (\bar{T}_i - T_j) \right] \quad \forall i \in I_b \tag{3.6.26}$$

Notice how this expression, depending on the flow direction, can reduce either to $T_i = \bar{T}_i$ or to $T_i = \sum_j |a_{ij}| T_j$, where $\sum_j |a_{ij}| T_j$ is the temperature of the adjacent branch. It is also worth to point out that, due to the adoption of the upwind scheme, the temperature of the adjacent branch is equal to the temperature of the adjacent node, thus the temperature gradient on the adjacent branch is null.

3.7 Governing equations in matrix form

The discrete governing equations can be conveniently recast in matrix form. Mass conservation (Eq. 3.6.18) can be rewritten as:

$$(\boldsymbol{AM} - \boldsymbol{E})\, \boldsymbol{u} = \boldsymbol{b} \tag{3.7.1}$$

Where $\boldsymbol{u}$ is the array containing the velocity value of each branches at time t_{n+1}, and has therefore length n_b.

While $\boldsymbol{A}$ is the graph incidence matrix as usual and have shape $n_n \times n_b$, $\mathbf{M}$ is a diagonal matrix of shape $n_b \times n_b$: therefore their product has shape $n_n \times n_b$. The elements composing the diagonal of $\boldsymbol{M}$ are defined as:

$$\mu_{jj} = S_j \rho_{j,n+1} \tag{3.7.2}$$

$\boldsymbol{E}$ is a matrix of shape $n_n \times n_b$, functional to the correct processing of boundary nodes. Its elements are defined as follows:

$$e_{ij} = \begin{cases} -\sum_l a_{il} \mu_{lj} & \forall i \in I_b \\ 0 & \forall i \notin I_b \end{cases} \tag{3.7.3}$$

The array $\boldsymbol{b}$ has size n_n and its elements are defined as follows:

$$b_{ij} = \begin{cases} -\frac{(\rho_{i,n+1})-(\rho_{i,n})}{\Delta t} V_i + \bar{\dot{m}}_i & \forall i \in I_{bu} \\ 0 & \forall i \in I_{bp} \\ -\frac{(\rho_{i,n+1})-(\rho_{i,n})}{\Delta t} V_i & \forall i \notin I_b \end{cases} \tag{3.7.4}$$

$\boldsymbol{b}$ contains the time derivative term; the rest of its features are also designed for the compact application of boundary conditions. In case node i is a boundary node with imposed velocity (or, more likely, flow rate), the mass flux term is simply added to its continuity equation. The mass flux can be calculated according to the specific boundary condition provided:

$$\bar{\dot{m}}_i = \rho_{i,n+1} \bar{u}_i \sum_j a_{ij} S_j \tag{3.7.5}$$

$$\bar{\dot{m}}_i = \rho_{i,n+1} \bar{\dot{V}}_i \tag{3.7.6}$$

Notice that for the rows corresponding to boundary nodes with imposed pressure, the continuity equation loses its meaning as it is reduced to the identity $0 = 0$.

Concerning momentum conservation equation (3.6.22), it can be written as:

$$\boldsymbol{A}^T \boldsymbol{P} = \boldsymbol{Y}\, \boldsymbol{u} + \boldsymbol{k} \tag{3.7.7}$$

$\boldsymbol{P}$ is the array containing nodal total pressure values and has size n_n.

It is worth to anticipate that branch momentum sources (such as σ_{fan} and σ_{loss}) on will be from now on treated as composed by two terms. The first one is linear with the velocity value of the concerned branch, and has therefore the form $m_{M,j} u_j$. The second one is a constant term $k_{M,j}$. The values of $m_{M,j}$ and $k_{M,j}$ are features of every specific source: their values also determine the behavior of the latter, which will accordingly act as a source or a sink.

In case a branch hosts multiple momentum sources, the coefficients m_M and k_M of such branch can be summed up by type to constitute a couple $(m_{M,j}, k_{M,j})$ capable of representing the cumulative action of all the sources/sinks present within the branch.

$\boldsymbol{Y}$ is therefore a diagonal matrix of size $n_b \times n_b$; its elements are composed by the sum of two terms. The first one is meant to generate the first addend of the time derivative term concerning each branch: it is equal to $\frac{\rho_{j,n+1} L_j}{\Delta t}$. The second one is the source/sink linear coefficient $m_{M,j}$ pertaining to such branch. These terms, thanks to the multiplication of $\boldsymbol{Y}$ for the velocity array at current time step ($\boldsymbol{U}$), will provide the corresponding terms of equation (3.6.22).

The elements of the diagonal of $\boldsymbol{Y}$ can therefore be defined as:

$$\nu_{jj} = \frac{\rho_{j,n+1} L_j}{\Delta t} + m_{M,j} \tag{3.7.8}$$

The last term of the second member ($\boldsymbol{k}$) is an array of size n_b, and it is also composed of two terms. The first one is the array constituted by the constant term of the momentum source/sink concerning each branch ($k_{M,j}$). The second one represents the second addend of the time derivative term of equation (3.6.22); it contains the velocity value at the previous time step, which is known. Density of to the j-th branch is interpolated from the node-based density field by means of the upwind operator.

$$k_j = k_{M,j} - \frac{U_{j,n}\,\rho_{j,n+1}\,L_j}{\Delta t} \tag{3.7.9}$$

Energy conservation (Eq. 3.6.25) assumes the form: the

$$\boldsymbol{W}\,\boldsymbol{T} = \boldsymbol{s} \tag{3.7.10}$$

where $\boldsymbol{T}$ is the array containing nodal temperature values at time step t_{n+1}, of size n_n. The $n_n \times n_n$ matrix $\boldsymbol{W}$ is responsible for the generation of the terms that are multiplied by temperature at the current step in equation (3.6.25):

$$\boldsymbol{W} = \frac{\boldsymbol{\rho} * \boldsymbol{c} * \boldsymbol{V}_n}{\Delta t} * \boldsymbol{I} + \boldsymbol{A} \cdot \boldsymbol{\phi}_b * \boldsymbol{M}_{n\to b} + \boldsymbol{M}_{b\to n} \cdot \boldsymbol{m}_E * \boldsymbol{M}_{n\to b} \tag{3.7.11}$$

In order to obtain a more compact equation the symbol $*$ has been employed to indicate *element wise product*. When applied between one dimensional arrays, like $\boldsymbol{\rho} * \boldsymbol{c}_p * \boldsymbol{V}_n$ in the first term of the second member, the result is an array that has as elements the products between the corresponding elements of the input arrays. On the other hand, a term like $(\boldsymbol{\phi}_b * \boldsymbol{M}_{n\to b})$, which is the element wise product between a 1D array and a properly shaped matrix (it must have a number of rows equal to the number of elements of the array), has the same result as a scalar product between:

- a diagonal matrix $(n \times n)$ that has the input array $(n \times 1)$ as main diagonal;
- the input matrix (e.g. $n \times m$)

Keeping in mind that each row of $\boldsymbol{W}$ is responsible for the generation of the energy conservation equation of one node, it is worth to highlight the nature of the different terms that sum up in equation (3.7.11) to define $\boldsymbol{W}$. By applying the distributive property of matrix product, we can consider each term as post-multiplied by the $n_n \times 1$ array $\boldsymbol{T}$

The first term, which is a diagonal $n_n \times n_n$ matrix, is meant to represent the part of the time derivative term (see equation (3.6.25)) that involves temperature at the current time step (t_{n+1}). It is originated as an array, and it is then cast into a diagonal matrix by multiplying it (*element wise*) for a properly shaped identity matrix $\boldsymbol{I}$. As it should be expected, just one element of this kind will appear on each row.

The second term represents the advective heat fluxes entering or exiting the node. The array which constitutes the core of such term, $\boldsymbol{\phi}_b$, is an array defined on branches which indicates the thermal capacity flux for each branch. It is obtained as follows:

$$\boldsymbol{\phi}_b = \boldsymbol{M}_{n\to b} \cdot (\boldsymbol{\rho} * \boldsymbol{c}_p) * \boldsymbol{S} * \boldsymbol{U} \tag{3.7.12}$$

The product between $\boldsymbol{\rho}$ (node defined density array) and $\boldsymbol{c}$ (node defined specific heat array) is first interpolated to a branch-defined array (employing upwind method), and then multiplied (element wise) by the arrays representing the branches section ($\boldsymbol{S}$) and velocity($\boldsymbol{U}$).

Note that the obtained array ($\boldsymbol{\phi}_b$) is net of the temperature: it lacks a post-multiplication for $\boldsymbol{T}|_b = \boldsymbol{M}_{n\to b} \cdot \boldsymbol{T}$ to correctly represent the advective heat flux. The term, like the whole $\boldsymbol{W}$ matrix will be post-multiplied by $\boldsymbol{T}$: therefore $\boldsymbol{\phi}_b$ needs to be post-multiplied by the upwind operator. Such matrix will act as an interface between the thermal capacity flux – defined on branches – and the temperature – defined on nodes. Once the branch-defined

thermal flux array is obtained, it is sufficient to pre-multiply it by the incidence matrix in order to select the "tributary" fluxes for each node and fix their sign.

The third term is meant to assign the linear part of the heat sources, defined on branches, to the competing nodes. Starting with the definition of an array representing (the linear part of) the sources action on branches, in terms of energy loss (or gain):

$$\boldsymbol{Q}_{E,m} = \boldsymbol{m}_E * \boldsymbol{T}|_b = \boldsymbol{m}_E * \boldsymbol{M}_{n\to b} \cdot \boldsymbol{T} \tag{3.7.13}$$

Such an array has then to be correctly partitioned between the nodes. Only the energy provided by the branches which are adjacent to each node and provide an entering flux to the node should be introduced within the energy balance of the node.

As previously seen in Section 3.6.1, a pre-multiplication for the *branches to nodes* upwind operator ($\boldsymbol{M}_{b\to n}$) gives the desired result.

As already stated for the other terms, the temperature array ($\boldsymbol{T}$) does not need to be included into the term, so only the $n_n \times n_n$ matrix $\boldsymbol{M}_{b\to n} \cdot \boldsymbol{m}_E * \boldsymbol{M}_{n\to b}$ is added to $\boldsymbol{W}$.

The constant term ($\boldsymbol{s}$) of equation (3.7.10) is significantly simpler:

$$\boldsymbol{s} = \frac{\boldsymbol{\rho} * \boldsymbol{c} * \boldsymbol{V}_n}{\Delta t} * \boldsymbol{T}_n + \boldsymbol{M}_{b\to n} \cdot \boldsymbol{k}_E \tag{3.7.14}$$

$\boldsymbol{s}$ takes into account the part of the time derivative term which refers to the temperature value at the previous time step $\boldsymbol{T}_n$ – which is known therefore grouped among constants – and the constant contribution of the heat sources action – which is distributed to nodes in the same way employed for the linear contribution.

The coefficients matrix and constant term of equation (3.7.10), as obtained by the equations (3.7.11) and (3.7.14), work perfectly for the energy balances of internal nodes. In order to include boundary conditions, both of those must go through local changes, that will pertain only the rows corresponding to boundary nodes. These are briefly illustrated, using the symbols $\bar{w}_{ij}$ and $\bar{s}_i$ for indicating the elements of the $\boldsymbol{W}$ matrix and the $\boldsymbol{s}$ array as previously defined. Once again, special elements are defined for the management of boundary nodes:

$$w_{ij} = \begin{cases} \bar{w}_{ij} & \\ 1 & \forall i \in I_b \wedge i = j \\ 0 & \forall i \in I_b \wedge i \neq j \end{cases} \tag{3.7.15}$$

$$s_i = \begin{cases} \bar{s}_i & \\ \frac{1}{2} \sum_j \left[|a_{ij}| \left(\overline{T}_i + T_j \right) + a_{ij} \frac{u_j}{|u_j|} \left(\overline{T}_i - T_j \right) \right] & \forall i \in I_b \end{cases} \tag{3.7.16}$$

The above formulation for coefficients and known terms on boundary nodes implements an inlet-outlet condition for temperature:

- if the velocity field is such that the flow enters the domain through the boundary node node i, then its equation becomes $T_i = \overline{T}_i$;
- if the velocity field is such that the flow exits the domain through node i, the value of T_i is set to be equal to the temperature of the only adjacent node (this definition is enequivocal because boundary nodes are allowed to be connected to only one branch, that is in turn able to connect only two nodes).

3.8 Solution algorithm

Since density is assumed as independent from local pressure values, it is possible to decouple the calculation of pressure and velocity. Many methods, called *segregated*, have been developed to accomplish such task; among them, the *SIMPLE* (Semi-Implicit Method for Pressure Linked Equations) [79] may be the most widely used. Such methods are based on a "guess and correct" approach: the variables are determined by iterative correction of their values.

Equations (3.7.1), (3.7.7), (3.7.10) therefore are solved by means of a custom segregated algorithm. An example of implementation of a similar method on a network problem can be also found in [80].

The first concept that should be introduced in order to explain any segregated algorithm is the decomposition of velocity and pressure fields in two components: a guessed field ([$u*$] and [$P*$]) and a variable correction field ([u'] and [P']).

$$\boldsymbol{P} = \boldsymbol{P}^* + \boldsymbol{P}' \tag{3.8.1}$$

$$\boldsymbol{u} = \boldsymbol{u}^* + \boldsymbol{u}' \tag{3.8.2}$$

The iterative procedure starts from the guessed pressure field $\boldsymbol{P}^*$. As an example, for the first iteration a feasible $\boldsymbol{P}^*$ choice could be to set all the nodes (except for boundary nodes) pressure to a fixed pressure value p_{ref}. By introducing such field in the matrix form of momentum conservation equation (3.7.7), it is possible to determine the guessed velocity field $\boldsymbol{u}^*$:

$$\boldsymbol{u}^* = \boldsymbol{Y}^{-1}(\boldsymbol{A}^T\,\boldsymbol{P}^* - \boldsymbol{k}) \tag{3.8.3}$$

By introducing definitions (3.8.1) into Eq. (3.7.7), and subsequently simplifying it using Eq. (3.8.3), a correlation between pressure correction $\boldsymbol{p}'$ and velocity correction $\boldsymbol{u}'$ can be carried out:

$$\boldsymbol{u}' = \boldsymbol{Y}^{-1}\,\boldsymbol{A}^T\,\boldsymbol{P}' \tag{3.8.4}$$

Then, introducing Eq. (3.8.4) and Eq. (3.8.1) into the continuity equation (3.7.1):

$$(\boldsymbol{A}\,\boldsymbol{M} - \boldsymbol{E})\boldsymbol{u}' = -(\boldsymbol{A}\,\boldsymbol{M} - \boldsymbol{E})\boldsymbol{u}^* + \boldsymbol{b} \tag{3.8.5}$$

Then, rewriting $\boldsymbol{u}'$ by its definition (3.8.4):

$$(\boldsymbol{A}\,\boldsymbol{M} - \boldsymbol{E})\boldsymbol{Y}^{-1}\,\boldsymbol{A}^T\,\boldsymbol{P}' = -(\boldsymbol{A}\,\boldsymbol{M} - \boldsymbol{E})\boldsymbol{u}^* + \boldsymbol{b} \tag{3.8.6}$$

The former linear system, of unknown $\boldsymbol{P}'$, can be rewritten as:

$$\boldsymbol{\Lambda}\boldsymbol{P}' = \boldsymbol{\theta} \tag{3.8.7}$$

where the $n_n \times n_n$ matrix $\boldsymbol{\Lambda}$ is composed by elements of the form:

$$\lambda_{ij} = \begin{cases} \sum_l a_{il}\frac{S_l\rho_l}{m_{K,l}+\frac{\rho_l L_l}{\Delta t}}a_{lj} & \forall i \notin I_b \\ 1 & \forall i \in I_b \wedge i = j \\ 0 & \forall i \in I_b \wedge i \neq j \end{cases} \tag{3.8.8}$$

The known term $\boldsymbol{\theta}$ has elements of the form:

$$b_j = \begin{cases} \sum_j a_{ij} S_j \rho_{b,j} u_j - \frac{(\rho_{i,n+1}) - (\rho i)}{\Delta t} & \forall i \notin I_b \\ 0 & \forall i \in I_b \end{cases} \tag{3.8.9}$$

Note that, in equations (3.8.8) and (3.8.9), a suitable choice of null and unitary elements within the system allows for the application of boundary conditions: the rows referring to pressure boundary nodes are changed to the simple identity $P'_i = 0$.

Once the linear system is solved, pressure should be corrected, by adding the P' to its current value. Similarly, velocity should be corrected by adding u'.

After each predictor-corrector step of the algorithm, the energy equation (3.7.10) is solved with the updated fields, the sources coefficients are recalculated based on the updated fields, and density is finally updated as a function of the newly obtained node temperature field. The iterative procedure stops when the infinity norm of the pressure correction field $\|\mathbf{p}'\|_\infty$ lies within a specified tolerance.

For the simulation of unsteady scenarios, a time-step value Δt must be assigned. The iterative procedure must then be solved multiple times, incrementing time value by the time step each time the convergence is reached, therefore repeating the calculation for the instants $(t = 0, \Delta t, \Delta t, \dots)$. An approach for the advanced modelling of time-dependent features will be further discussed within the next sections.

On the other hand, for steady calculations a single run of the iterative procedure is sufficient. In this case, the time-dependent terms present in all the governing equations are zeroed out.

3.9 Treatment of source/sink terms

As it was mentioned while illustrating the matrix form of the governing equations, it has been chosen to represent all the branches source and sink terms as linear functions of the current velocity value of the concerned branch.

Taking as an example the momentum balance equation (3.6.22), the term $(\Delta P_{fan,j} - \Delta P_{loss,j})_{n+1}$ is rewritten as:

$$(\Delta P_j)_{n+1} = m_{M,j,n+1}\, u_{j,n+1} + k_{M,j,n+1} \tag{3.9.1}$$

Therefore, fan thrust and friction losses will be represented by the same kind of equation. It will be proven that, with an appropriate choice of the coefficients m and k, this simple linear model can conjugate a satisfactory representation of the original feature with the need not to add excessive complexity to the governing equations.

The very same linear model has been successfully employed for representing the heat sources (i.e. the exchange between the air and the tunnel walls):

$$(Q_{E,j})_{n+1} = m_{j,n+1}\, T_{j,n+1} + k_{j,n+1} \tag{3.9.2}$$

This representation is rather effortless for heat sources (related convective heat exchange), as their contribution to the energy equation linearly depends on the current temperature of the fluid in the branch.

On the other hand, momentum source and sink terms have a nonlinear dependence on local velocity. Those terms have been linearized anyway to the form of $m_M u + k_M$. Within the iterative solution loop described in the previous paragraph, velocity at a given iteration k is used to incorporate nonlinear terms in the coefficient m for the subsequent iteration $k + 1$.

Thanks to this device, the momentum conservation equation system remains linear. Of course, as it will be further illustrated within the description of the sources, the values of the $\boldsymbol{m}$ and $\boldsymbol{k}$ arrays will need to be recalculated at every iteration.

3.9.1 Friction

Starting with friction sources, their implementation is based on the following equation, which is widely accepted for turbulent flows:

$$\Delta P_j = \left(\frac{f_j L_j}{D_{h,j}} + \beta_j \right) \frac{\rho_j u_j \left| u_j \right|}{2} \tag{3.9.3}$$

Such definition includes:

- a friction factor (f_j) which is employed for accounting the pressure losses distributed through the whole branch, due to the interaction between the fluid and the walls.
- a concentrated loss factor (β_j) which is employed for accounting the pressure losses due to a particular feature or part of the channel (e.g. a bend or a sudden section change).

These different terms have been represented through different source objects. Although the overall mechanism is very similar, it has to be mentioned that β coefficients are mostly assumed as constant in literature. This is not as established for regarding friction factor f since the coefficient itself depends on Reynolds number, thus on velocity.

Of course momentum sources of different nature can be assigned simultaneously to a branch: it is enough to sum their m and k values.

Distributed losses

The values of m and k for a *distributed loss* momentum source are defined as:

$$m_{M,j,loss,n+1} = \rho_j \frac{f_j L_j}{D_{h,j}} \frac{\left| u_{j,n} \right|}{2} \tag{3.9.4}$$

$$k_{M,j,loss,n+1} = 0 \tag{3.9.5}$$

The only issue here, aside from updating $u_{j,n}$ at every iteration, is the update of the value of the f coefficient. The software implementation chosen here leaves the possibility of defining the *source object* (which is the code snippet that is in charge of fetching the updates of the source coefficients) based on the model of choice:

- constant friction factor model: in this case a value is assigned to f while building the model, and will not be changed;

- Colebrook-White friction model: in this case f value is calculated (iteratively) at every iteration by means of the Colebrook-White implicit formula [81];
- Swamee-Jain friction model: in this case f value is calculated at every iteration using the Swamee-Jain explicit approximation of the Colebrook-White formula [82].

Concentrated losses

The values of m and k for a *concentrated loss* momentum source are defined as:

$$m_{M,j,loss,n+1} = \rho_j \beta_j \frac{|u_{j,n}|}{2} \tag{3.9.6}$$

$$k_{M,j,loss,n+1} = 0 \tag{3.9.7}$$

A *source object* is also required – at least for updating $u_{j,n}$ at every iteration and then calculating the new m and k. Two different models are provided for beta:

- constant loss coefficient model: in this case a value is assigned to β while building the model, and will not be changed;
- directional loss model: in this case two different β values are defined during the initialization. The value will be chosen between two didderent values β_1 and β_2 according to the direction of the branch velocities.

The second model is particularly useful as it comes to defining a concentrated loss coefficient for the tunnel portals, due to the high asymmetry of the feature.

3.9.2 Centrifugal fans

AF (fresh air) fans

A set of characteristic curves at different rotation regimes is reconstructed from catalogue, for a reference density $\rho = 1.07$ kg/m^3.

$$\Delta p\,(Q, n) = c_3(n)Q^3 + c_2(n)Q^2 + c_1(n)Q + c_0(n) \tag{3.9.8}$$

Table 3.1: Coefficients in Eq. (3.9.8) as a function of n.

n [rpm]	c_3	c_2	c_1	c_0
250	1.2060×10^{-3}	-0.41939	9.5448	362.85
500	5.3954×10^{-4}	-0.41231	18.808	1462.2
750	3.7927×10^{-4}	-0.41861	28.506	3308.2
1000	2.8901×10^{-4}	-0-42326	38.513	5934.7
1250	2.1819×10^{-4}	-0.42275	48.182	9410.0

AV (extraction) and *relais* fans

A set of characteristic curves is reconstructed from catalogue, for a reference density $\rho = 1.0$ kg/m^3 and for a fixed regime $n = 1000$ rpm.

$$\Delta p\,(Q) = k_2 Q^2 + k_1 Q + k_0 \tag{3.9.9}$$

Table 3.2: Coefficients in Eq. (3.9.9) for AV and *relais* fans.

fan	k_2	k_1	k_0
AV	-0.57940	32.955	8271.9
relais	-0.60849	64.887	2449.9

Dimensionless curves

By using the following reduced coordinates:

- $\phi = \dfrac{Q}{nL_{ref}^3}$ reduced flow rate
- $\psi = \dfrac{\Delta p}{\rho n^2 L_{ref}^2}$ reduced pressure

all the above characteristic curves were reduced to a more compact, dimensionless quadratic form:

$$\psi = \gamma_0 + \gamma_1 \phi + \gamma_2 \phi^2 \tag{3.9.10}$$

Table 3.3: Reference length and coefficients of the reduced curve equation (3.9.10).

fan	$L_{ref}[m]$	γ_0	γ_1	γ_2
AF	2.245	4.027	4.068	-8.095
AV	2.0859	6.8442	4.1244	-10.9686
relais	2.0142	2.1740	7.8410	-10.0150

In the reduction process, the appropriate values (reported above) of n were used for each curve, whereas L_{ref} was chosen so as to ensure that $\psi = 0$ for $\phi = 1$. It should be noted that, in classical similarity theory for turbomachinery, the reference length should be equal to the rotor diameter D (which is unknown at present for the three fan models, but is estimated to be between 2-3 m by visual inspection). While the order of magnitude of the obtained values of L_{ref} matches the order of magnitude of the rotor diameter in all cases, by no means these curves could be used to represent "similar" fans with different rotors. If precise values of D will become available, the curves must be recalculated.

Curve adaptation

Now that all the fan curves have been defined and reduced to non-dimensional form, there is a further problem that needs to be tackled before defining the source coefficients that will allow to include the fans in the numerical model.

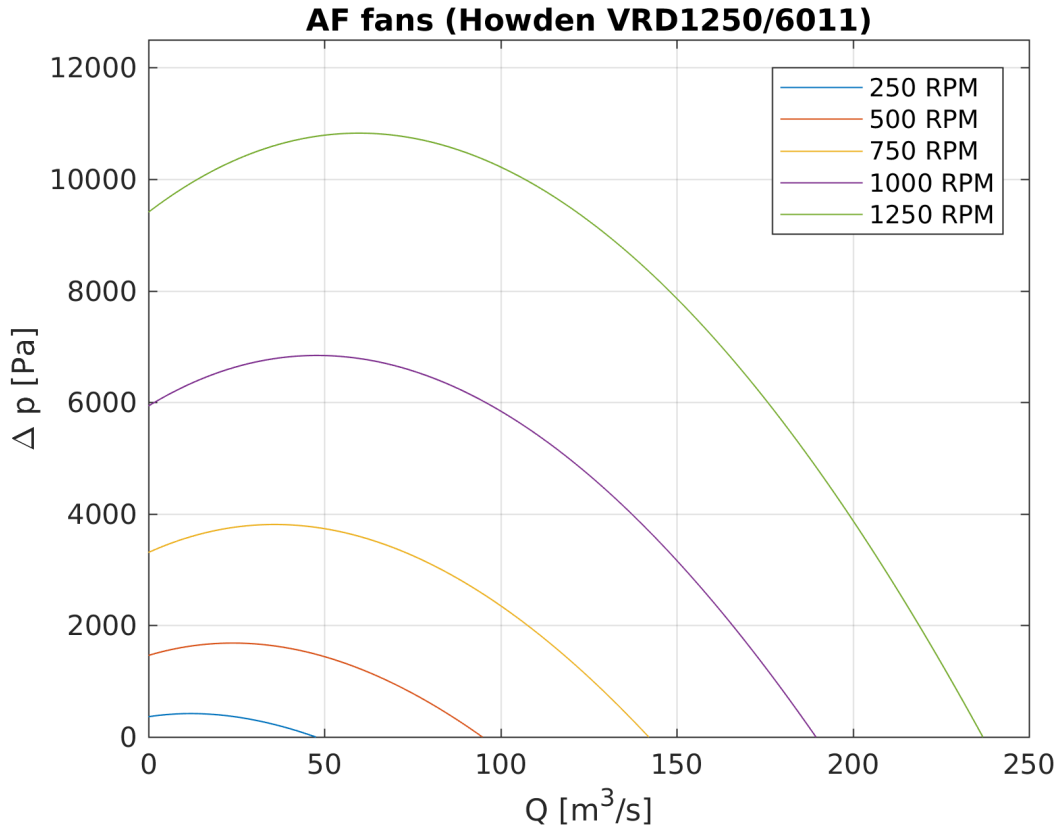

Figure 3.3: Dimensional characteristic curves of the AF fans at different RPMs for $\rho = 1.07$ kg/m^3.

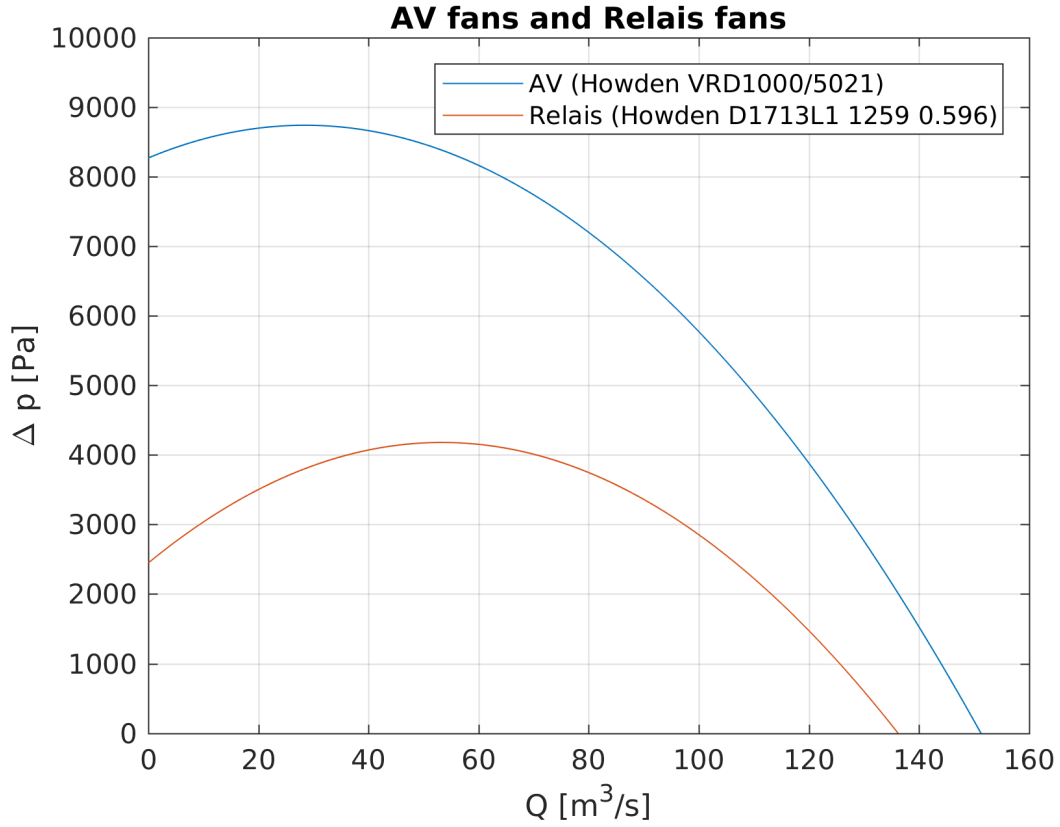

Figure 3.4: Dimensional characteristic curves of the AV and *relais* fans at $n = 1000$ rpm and for $\rho = 1.0$ kg/m^3.

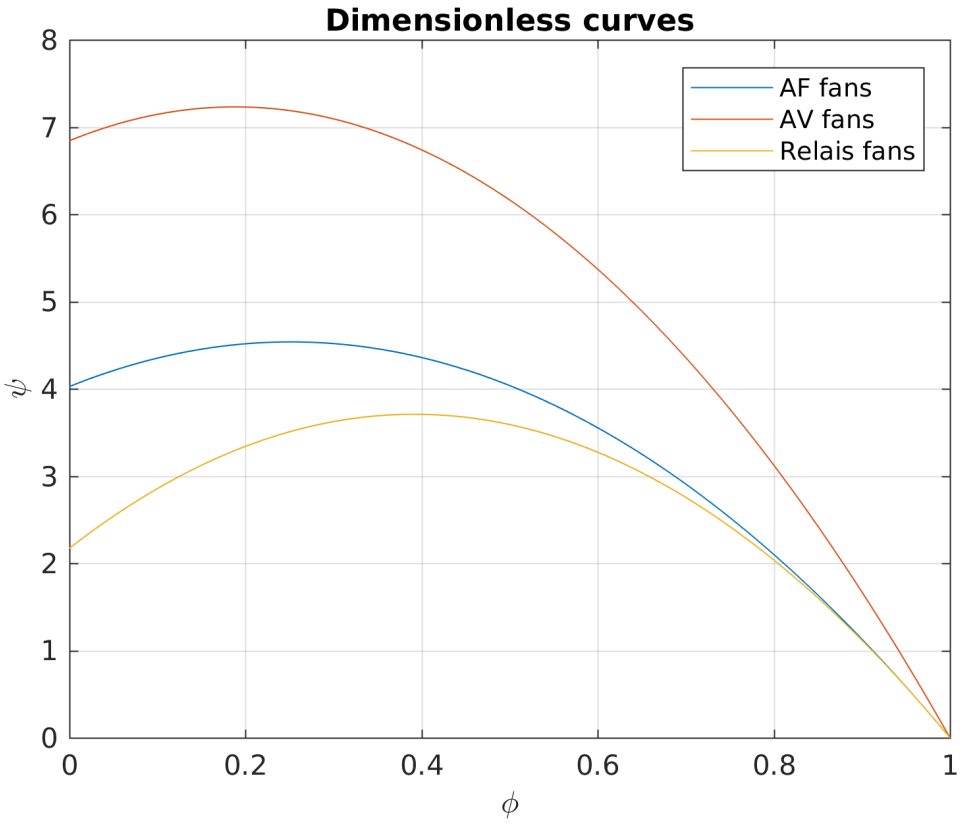

Figure 3.5: Dimensionless characteristic curves of the AF, AV and *relais* fans.

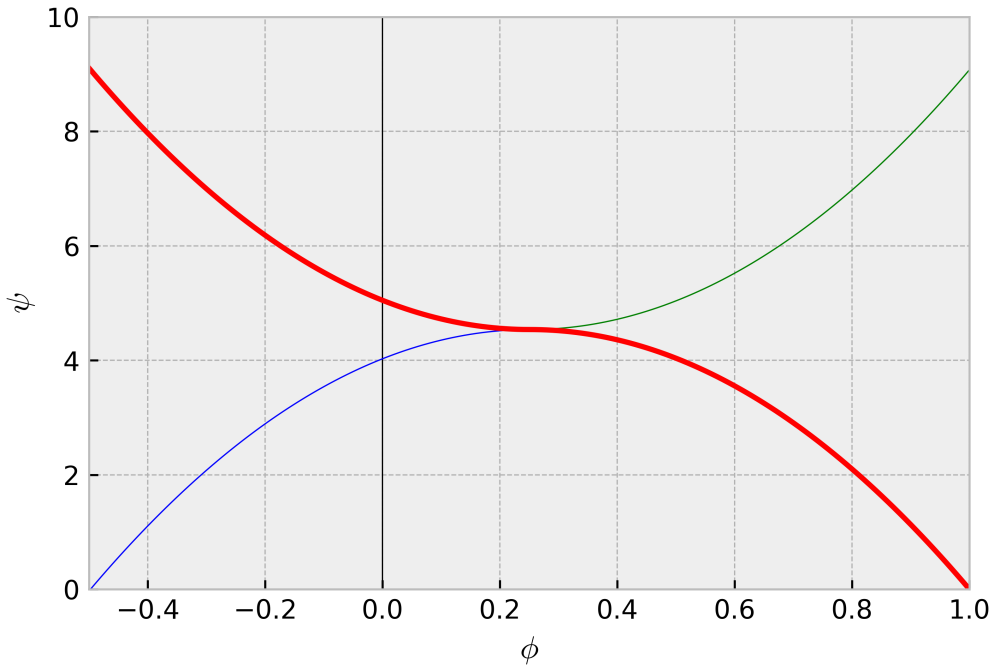

Figure 3.6: Adapted fan curve (red), original curve (blue), mirrored curve(green)

Since the numerical procedure is iterative and may start from very incoherent state variable fields (the pressure and velocity fields are initialized at a constant, uniform, value), the shape of the fan curve may not favour convergence of the calculation.

Moreover, the part of the curve that lays outside of the interval $\phi \in [0, 1]$ is not representative of the fan work. For example, in case of negative flow-rate, a non-return valve would avoid any flow: for this reason, a more accurate curve could be made by employing a vertical slope (or at least one with a very high and negative slope) for ϕ values close to zero, and using the normal curve for positive ϕ.

Unfortunately this is not feasible, as it will create an abrupt discontinuity in the derivative of the curve, thus possibly compromising the stability of the whole solution process.

The issue has been fixed by exploiting the fact that the curve $\psi = \gamma_0\phi^2 + \gamma_1\phi + \gamma_2$ has null slope in correspondence of its vertex. The vertex point is defined as ($\phi_V = -\frac{2\gamma_1}{\gamma_0}, \quad \psi_V = -\frac{\gamma_1^2}{4\gamma_0} + \gamma_2$).

As it can be appreciated in Figure 3.9.2, the original curve (blue) has been mirrored (green) with respect to its vertex. Then, a new curve is generated by selecting the original curve for $\phi > \phi_V$, and the mirrored curve for $\phi < \phi_V$.

The resulting curve is defined as:

$$\psi = \begin{cases} \gamma_0\phi^2 + \gamma_1\phi + \gamma_2 & \forall\phi \in [0, -\frac{\gamma_1}{2\gamma_0}] \\ -\gamma_0\phi^2 - \gamma_1\phi + \gamma_2 - \frac{\gamma_1^2}{2\gamma_0} & \forall\phi \in [-\frac{\gamma_1}{2\gamma_0}, 1] \end{cases} \tag{3.9.11}$$

Note that it doesn't present any first derivative discontinuity because the curves from which it is generated have the same value and same derivative at the junction.

Although the first part of the curve (for $\phi \in [0, \phi_V]$), which belongs to the interval of validity of the original curve, has been distorted, this doesn't represent a problem in practice since the fans are designed to work strictly with flowrates that $\phi > \phi_V$. The fans working point are to be checked after the simulation, in order to validate the results.

Source coefficients

Starting from the curve described by equation (3.9.11) and the coordinate system composed by $\phi = \dfrac{Q}{nL_{ref}^3}$, $\psi = \dfrac{\Delta p}{\rho n^2 L_{ref}^2}$ it is possible to define the usual m and k source coefficients.

First of all let's express the abscissa of the vertex in terms of velocity, so to be able to discern which curve equation to use as characteristic curve of the fan just by checking local velocity.

The velocity value that provide $\phi = \phi_V$ is defined as:

$$u_v = -\frac{nD_h^3}{A}\frac{\gamma_1}{2\gamma_0} \tag{3.9.12}$$

Now, let's separate the part of the source polynomial which depends on velocity ($\gamma_0\phi^2 + \gamma_1\phi$) from the constant term (γ_2):

$$\psi = \psi_1(\phi) + \psi_2 \tag{3.9.13}$$

Starting from the constant term, which is simpler:

$$k|_{n+1} = \begin{cases} -\rho(nD_h)^2 c & \forall u|_n \in [0, u_v] \\ -\rho(nD_h)^2(\gamma_2 - \frac{\gamma_1^2}{2\gamma_0}) & \forall u|_n \in [u_v, 1] \end{cases} \tag{3.9.14}$$

The source constant term k is basically the constant term ψ_2 (c in the original dimensionless curve), converted from the coordinate ψ to an effective ΔP. The sign has been converted to negative to match the sign convection for k and m dictated by the discretized governing equations.

Concerning the m term of the source, it has to be kept in mind that, at the current iteration, it will be further multiplied by the velocity (u_{n+1}) in the governing equations. It is convenient to start by calculating ψ_1/ϕ as a function of $u|_n$:

$$\frac{\psi_1}{\phi} = \begin{cases} -\frac{aA}{nD_h^3}u|_n - b & \forall u|_n \in [0, u_v] \\ \frac{aA}{nD_h^3}u|_n + b & \forall u|_n \in [u_v, 1] \end{cases} \tag{3.9.15}$$

Then, by converting the ψ coordinate to ΔP, $\frac{\Delta P}{\phi}$ is obtained:

$$\frac{\Delta P}{\phi} = \begin{cases} \rho n^2 D_h^3(-\frac{aA}{nD_h^3}u|_n - b) & \forall u|_n \in [0, u_v] \\ \rho n^2 D_h^3(\frac{aA}{nD_h^3}u|_n + b) & \forall u|_n \in [u_v, 1] \end{cases} \tag{3.9.16}$$

Finally, by multiplying such terms by $\frac{\phi}{u} = \frac{A}{nD_h^3}$ and changing their sign to match the sign convention of the governing equations, the m coefficient is obtained:

$$m|_{n+1} = \begin{cases} -\frac{\rho An}{D_h}(-\frac{aA}{nD_h^3}u|_n - b) & \forall u|_n \in [0, u_v] \\ -\frac{\rho An}{D_h}(\frac{aA}{nD_h^3}u|_n + b) & \forall u|_n \in [u_v, 1] \end{cases} \tag{3.9.17}$$

3.9.3 Jet fans

The thrust of a jet fan (or of a group of N fans) installed inside a larger duct (i.e. a tunnel) is redistributed on the whole duct cross section. The resulting Δp-Q relation, where Q is the flow rate in the duct, can be represented by the following equation:

$$\Delta p = \rho \eta N u_f \frac{A_f}{A_d} \left(u_f - \frac{Q}{A_d} \right) \tag{3.9.18}$$

The parameters in Eq. (3.9.18) are listed in Table 3.4 for the case of the *Mont Blanc* tunnel, as derived from the technical data sheet of the installed jet fans and on on-site measurements.

Table 3.4: Parameters for a jet fan couple in the *Mont Blanc* tunnel, Eq. (3.9.18).

symbol	quantity	value	unit
ρ	reference density	1.2	[kg/m^3]
η	installation efficiency	0.52	
N	number of fans in single group	2	
A_f	fan cross section	0.396	[m^2]
A_d	duct (tunnel) cross section	45.2	[m^2]
u_f	characteristic fan velocity	35.53	[m/s]

In order to reduce Eq. (3.9.18) and obtain a $\psi(\phi)$ form for which $\psi = 0$ for $\phi = 1$, the following choices for the reference rotational speed n_{ref} and length L_{ref} are appropriate:

$$L_{ref} = \sqrt{A_d} \qquad n_{ref} = \frac{u_f}{\sqrt{A_d}} \tag{3.9.19}$$

Eq. (3.9.18) is recast in dimensionless form as follows:

$$\psi = \Gamma \left(1 - \phi \right) \tag{3.9.20}$$

where:

$$\Gamma = \eta N \frac{A_f}{A_d} = 9.112 \times 10^{-3}$$

for the *Mont Blanc* tunnel case.

If Eq. (3.9.20) is compared with (3.9.10), one has:

$$\gamma_0 = \Gamma \qquad \gamma_1 = -\Gamma \qquad \gamma_2 = 0 \tag{3.9.21}$$

Source coefficients

Starting from the curve described by equation (3.9.20) and the usual coordinate system composed by $\phi = \dfrac{Q}{n L_{ref}^3}$, $\psi = \dfrac{\Delta p}{\rho n^2 L_{ref}^2}$, it immediate to define m and k source coefficients:

$$m|_{n+1} = \Gamma \rho n \frac{A}{D_h} \tag{3.9.22}$$

$$k|_{n+1} = -\Gamma \rho n^2 D_h^2 \tag{3.9.23}$$

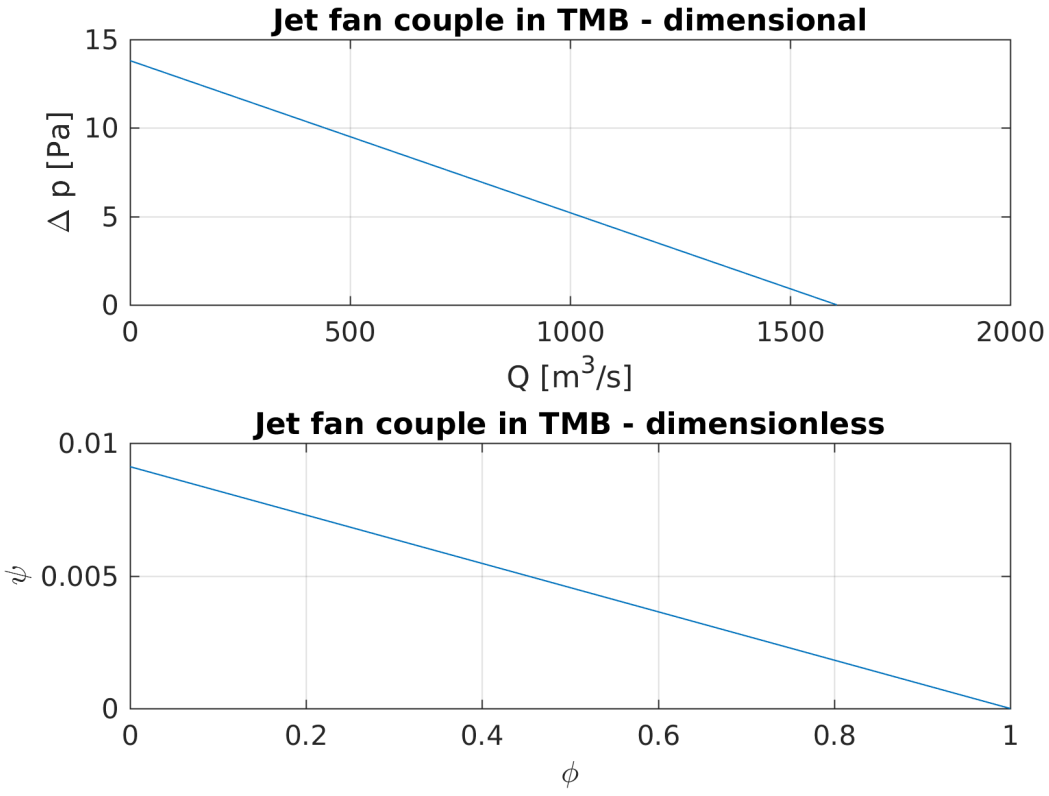

Figure 3.7: Dimensional and dimensionless characteristic curve of a jet fan couple as installed in the *Mont Blanc* tunnel.

3.9.4 Heat transfer

Refering to the equations (3.7.13) and (3.7.14), the equation representing the thermal energy gained/lost by the fluid while traversing the j-th branch can be written as:

$$\dot{Q}_{E,j} = m_{E,j} T_j + k_{E,j} \tag{3.9.24}$$

A *source object* is also required – at least for updating $u_{j,n}$ at every iteration and then calculating the new m and k. Two different models are provided for the representation of different kinds of sources, although other models could be easily added:

- fixed heat flux: in this case the energy of the fluid goes under an fixed increment/decrement, regardlessly of its temperature;
- convective exchange with tunnel walls: the fluid exchanges heat with a source which has fixed temperature. Therefore, the amount of heat gained/loss by the fluid depends on its temperature.

The m and k coefficients in charge of adapting the linear source of equation (3.9.24) to the aforementioned sources types are defined and briefly commented at the following sections.

Fixed heat flux

$$m_{E,j} = 0 \tag{3.9.25}$$

$$k_{E,j} = \dot{Q}_j \tag{3.9.26}$$

This very simple source requires no linear term.

Convective heat transfer

Convective heat transfer is relatively more complex to implement. Starting from the definition of heat transfer coefficient h and Nusselt number (expressed for internal flows) Nu:

$$\dot{Q} = h\, S\, \Delta T \tag{3.9.27}$$

$$Nu = \frac{h D_h}{\lambda} \tag{3.9.28}$$

With S identifying the heat transfer area, which in the present case is equal to $\pi D_{h,j} L_j$. Therefore, $\dot{Q}$ can be rewritten as:

$$\dot{Q}_{E,j} = \lambda_j Nu_j L_j \pi \left(T_j - T_\infty\right) \tag{3.9.29}$$

Therefore:

$$m_{E,j} = \lambda_j Nu_j L_j \pi \tag{3.9.30}$$

$$k_{E,j} = \lambda_j Nu_j L_j \pi T_\infty \tag{3.9.31}$$

The sign of k has been changed since it has been brought to the right hand side in equation (3.7.13).

The only issue here, aside from updating λ_j at every iteration, is the calculation of the Nusselt number (which must also be updated at every iteration). The code leaves the choice to define the *source object* based on the model of choice between:

- constant Nusselt number: in this case a value is assigned to Nu while building the model, and will not be changed;
- Dittus-Boelter equation: in this case Nu is calculated at every iteration by means of the Dittus-Boelter explicit formula, based on local Reynolds and Prandtl numbers.

3.10 Event based logic for transient simulations in the TMB

In order to simulate the complete management of an emergency event (see section 2.4.3) it is certainly useful to have governing equations capable of accounting inertial terms, and to have defined a solution algorithm capable of performing time-dependent simulations based on those equations. Nonetheless, this is not enough: it is necessary to take into account the sequence of events which include centrifugal fan regime changes, opening/closing of extraction vents, axial jet fans activation/deactivation.

All of these actions, which concern momentum sources, can be efficiently represented by changing one (or more) of the sources inner variables as these, in turn, affect the m and k coefficients calculated from the source itself.

Aiming at addressing at least a part of these occurrences, an *Events Manager* object has been created: this object performs its assignment at each time step just before the sources objects update, the algorithm run and the subsequent solution of the transported variables linear systems (which is only one in this case, represented by energy conservation equation). Unsurprisingly, the *Events Manager* object interacts directly with the sources so as to change the way they may respond once they are updated or directly called later.

As an example, the opening/closing of extraction vents is based on a instantaneous change of the corresponding source concentrated loss coefficient (β). Changing such a coefficient directly affects the m term related to the concerned branch (see Section 3.9.1). On the other hand, a change in a centrifugal fan regime changes the source inner equations which manage the update of m and k. Once the regime has been changed, the source still recalculates m and k based on local velocity once it is called for an update; nonetheless the functions in charge of the update, $m(u)$ and $k(u)$, have been changed so their evaluation leads to a different result.

To this extent, the *Events Manager* can be implemented with the help of conditional statements. Given an action to be performed, an identifier of its target source object, and the time at which the action should be performed, it is trivial to check if the time has passed, and to perform (or not) the action accordingly. This logic can be extended to multiple actions by creating a list of elements capable of representing these actions (each

element should contain all the previously mentioned details about the corresponding action, and can therefore be called *Event* object), then sorting such list based on the activation times.

Thanks to the availability of a sorted list of these newly defined *Event* objects, the *Events Manager* can easily operate, at each time step, by recursively repeating the following sequence (until its auto-deactivation):

- check if the event at the top of the list (which has the lowest activation time) should take place;
- if so, the corresponding action is performed and the event object is discarded from the list; if not, the *Events Manager* deactivates until the next time step.

3.10.1 Activation ramps

The only complication that still needs to be addressed is the fact that all of these actions do not happen instantly in the real tunnel: all of them follow transitions that can take a time in the order of seconds (e.g. opening extraction vents) or minutes (e.g. bringing an extraction fan from 0 to 1000 rpm). Moreover, the behavior of the controlled variable during the transient can significantly vary according to the kind of the source object.

For this reason, the idea of activation/deactivation ramps needs to be included. An activation ramp is a curve which expresses the dependence of the controlled variable (y) from time during the source transient. It is meant to bring the variable from an initial value (y_0) to a final value (y_f), within a well defined time interval ($t_f - t_0$). The ramp shape and characteristic time are properties of each source objects, which are inherited during the generation of the specific object and thus depend on the nature of the sources. Also, two different ramps may be provided for the increase and decrease of the controlled variable (e.g. the centrifugal fans show very different transients while being turned on or off).

So, having introduced the concept of activation ramp, the action of the *Events Manager* may be redefined: from now on every action corresponds to the initialization and activation of a ramp on a source object.

Also, after checking for events that may take place, the *Events Manager* is in charge of updating the sources objects according to the ramp objects which are active. It will therefore check if any source has an "active ramp" (i.e. is going through a transient), and then for each active ramp which is encountered:

- the source inner variable which is controlled by the active ramp is changed based on current time t, following the ramp logic;
- if the current time t exceeds the ramp end time (t_f), the transient is finished and the ramp is not needed anymore (as it would yield a constant value of y_f from t_f on) and it is therefore discarded.

3.10.2 Experimental data and modeled ramps

A database of a series of 12 events occurred in 2017 in the *Mont Blanc* tunnel has been analyzed to determine the transient variation of the rotational speed of AV and *relais* fans. For the 4 *relais* fans, all the cases where the fan speed was automatically reduced due

to the occurrence of adverse pressure gradients (*bridage*) were discarded. A case where a switch-off was operated was also present.

Concerning jet fans, laboratory measurements of thrust have been used to recover the characteristic times. For the switch-on phase between states 0 and 1, the model ramp is the so-called *smoothstep*:

$$n = \begin{cases} n_0 & \text{if } t < t_0 \\ n_0 + (n_1 - n_0)\left[3\left(\frac{t-t_0}{t_1-t_0}\right)^2 - 2\left(\frac{t-t_0}{t_1-t_0}\right)^3\right] & \text{if } t_0 \leq t \leq t_1 \\ n_1 & \text{if } t > t_1 \end{cases} \tag{3.10.1}$$

where $\tau_{on} = t_1 - t_0$ is the characteristic time of the switch-on phase.

For the switch-off phase from state o, an exponential decay (with characteristic time τ_{off}):

$$n = n_o e^{-\frac{t-t_o}{\tau_{off}}} \tag{3.10.2}$$

Obtained values for τ_{on} and τ_{off} for the different fan types are reported below:

	AV (0-50 ÷ 50-100)%	*relais*	jet fans
τ_{on} [s]	36 ÷ 64	175	1.4
τ_{off} [s]	84	213	2.2

In the following Figures the activation ramps employed in the model for the management of switch-on and switch-off, in the form of *smoothstep* functions and exponential decay functions respectively, are compared with the experimental data obtained from the events log. In particular, Figures 3.8 and 3.10.2 show the rotational velocity of AV fans in function of time, during the switch-on phase. The switch-on of AV fans is divided in two steps; the first one, which starts as soon as an *event presumption* configuration is required by the control center, raises the regimes of all the AV fans from 0 to 500 rpm (Figure 3.8). The second step (Figure 3.10.2) takes place as soon as the emergency event is confirmed, and raises the regime to 1000 rpm. Figure 3.10 concerns the switch-on phase of relais fans, which takes place in one single step to reach a final regime 1500 rpm. The switch-off ramps for AV and *relais* fans, are represented in Figures 3.11 and 3.12 respectively.

Figures 3.13 and 3.14 represent the activation ramps employed for axial jet fans (switch-on and switch-off respectively). The fan thrust has been represented on the y-axis instead of the usual rotational velocity: this is due to the fact that the data employed for fitting the jet fans activation ramps consist in laboratory measurements of thrust.

Regarding the change of regime of AF fans, from the inspection of the logs, it emerges that a variation of 70 rpm every 10 seconds can be assumed as reasonable. A more refined estimate goes beyond the resolution of the TMB acquisition system, and thus is deemed as not necessary.

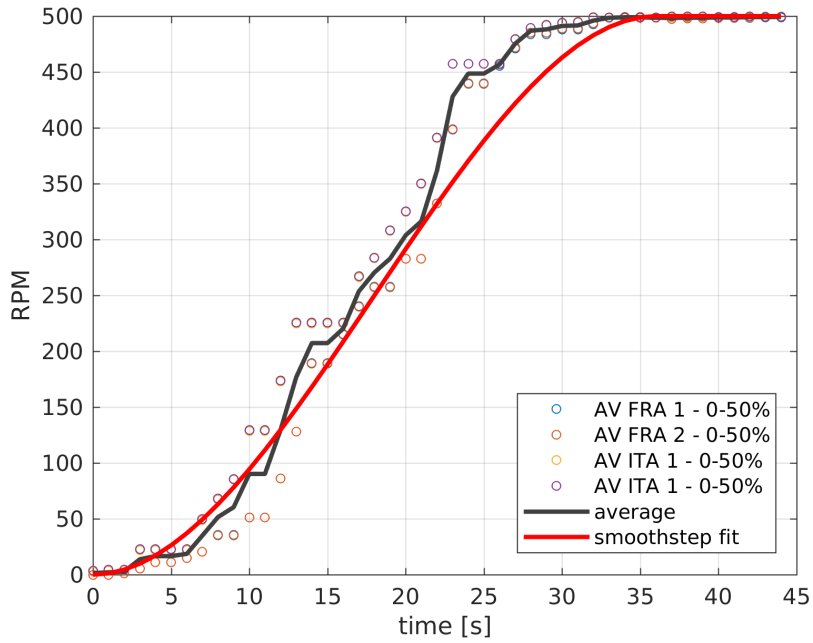

Figure 3.8: AV fans, 0-50% switch-on ramps: ensemble average and smoothstep function fit.

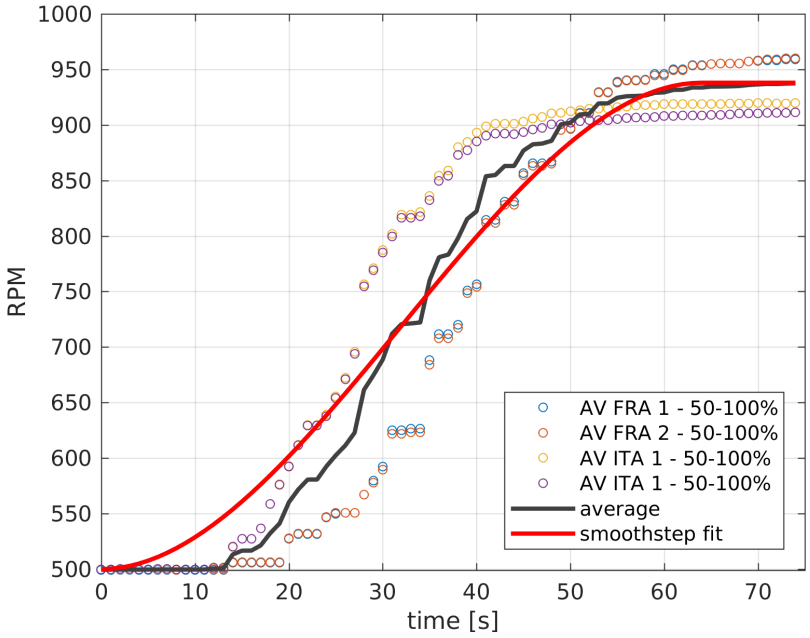

Figure 3.9: AV fans, 50-100% switch-on ramps: ensemble average and smoothstep function fit.

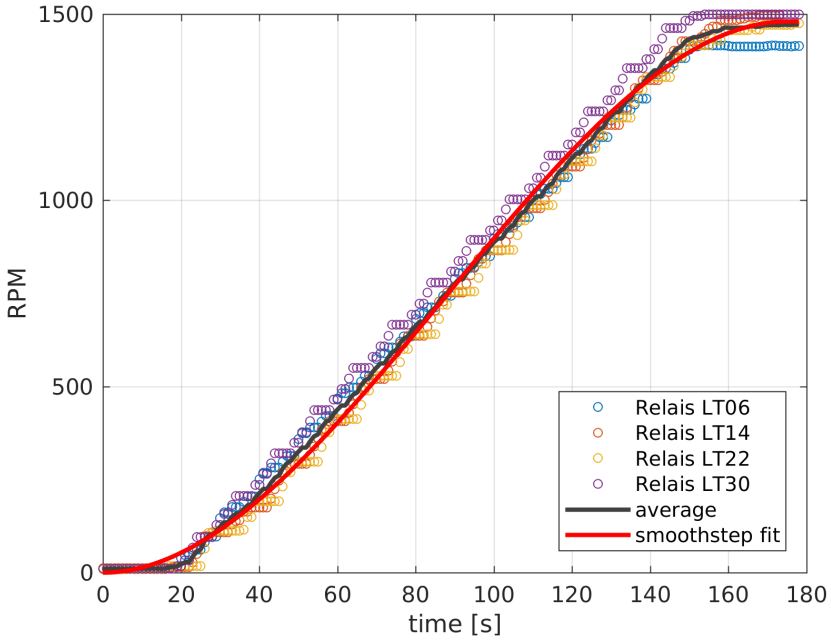

Figure 3.10: Relais fans switch-on ramps: ensemble average and smoothstep function fit.

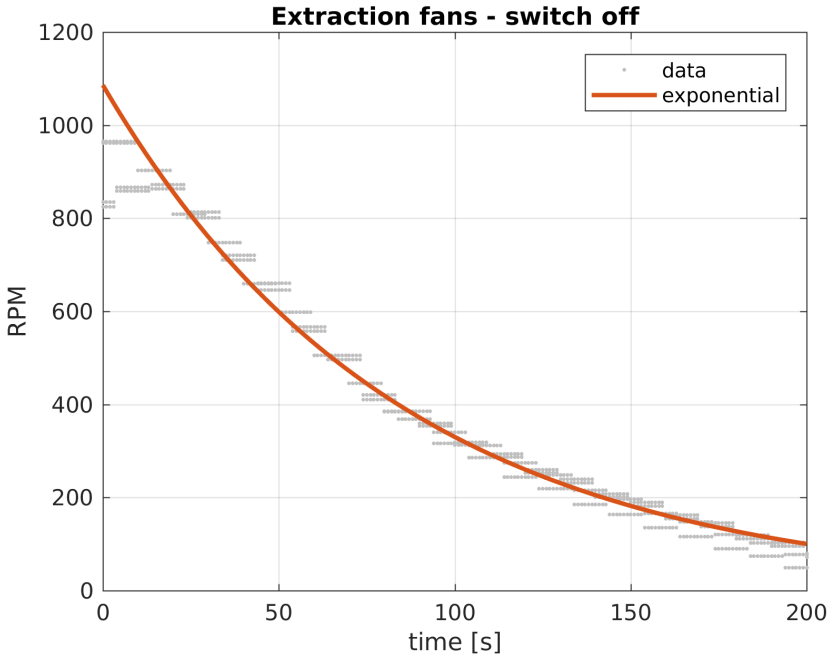

Figure 3.11: Switch-off data for the AV fans and exponential fit.

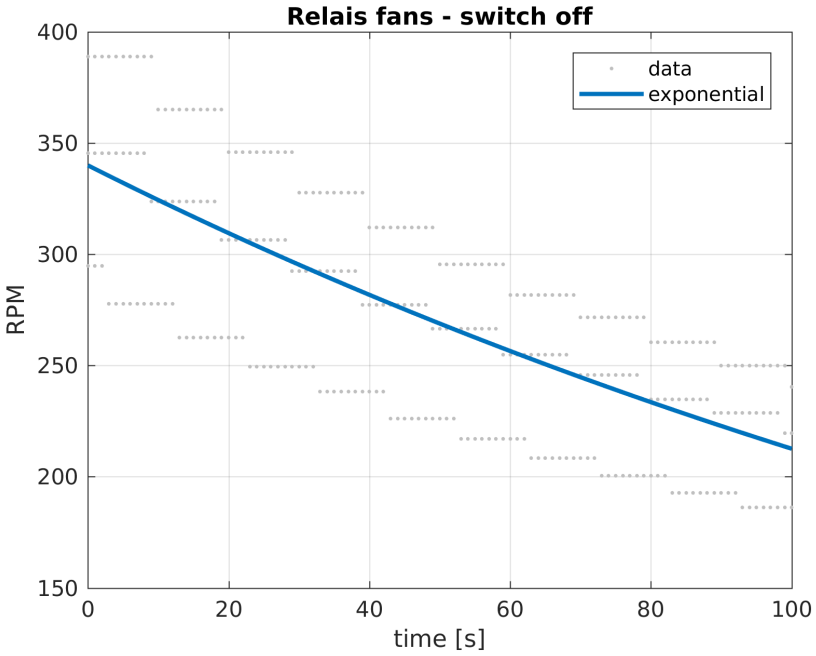

Figure 3.12: Switch-off data for the *relais* fans and exponential fit.

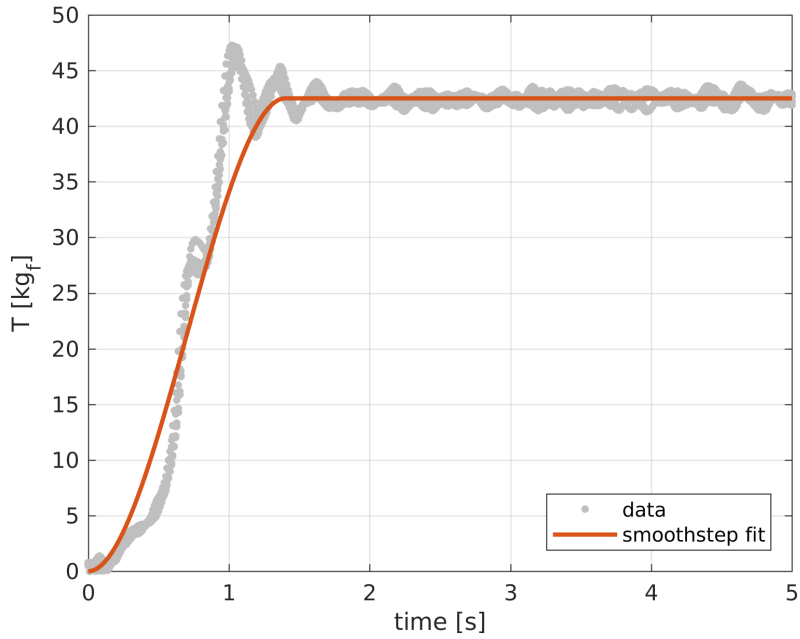

Figure 3.13: Switch-on data for the jet fans and smoothstep fit.

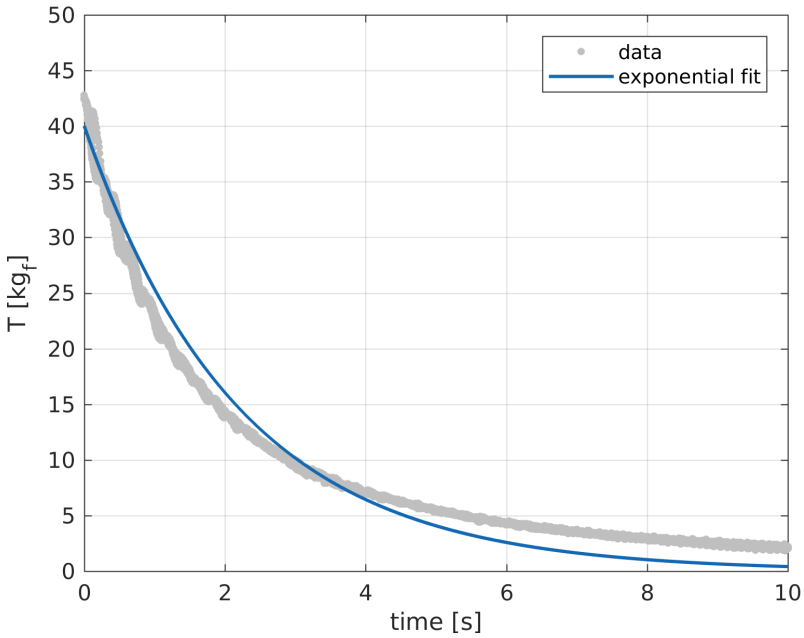

Figure 3.14: Switch-off data for the jet fans and exponential fit.

3.11 Some notes on model implementation

A complete explanation of the implementation of the numerical method goes beyond the scope of the present work. Instead, in this Section, a few insights and examples will be provided.

An object-oriented language (Python) has been chosen for the implementation. The main advantage of this choice is the possibility to define customized classes, that can be set to represent the variety of components that constitute the tunnel and its ventilation system. For example, the centrifugal fans can be defined as objects that influence the source term of the momentum conservation equation, based on local flow variables. This allows for a great code flexibility: in order to test a different fan model, it would be sufficient to rewrite the fan object (or just some internal parameters) and use it in a simulation.

Another example of the handiness of an object-oriented model can be found in the adaptability to the graph representation. For example, nodes and branches can be represented as classes on their own, namely `Node` and `Branch` objects. Each of these objects should store in its attributes all the information that compete to a single entity of the network: nodes should store location, and branches should store neighbours nodes and geometric features. Auxiliary attributes can be defined, in order to facilitate the access to specific elements: one or multiple *tags* (short strings) can be assigned to each element. For example, a branch could be provided with the tags "jetfan", "#31" and "tunnel".

Due to the number of elements constituting the network, a special container (namely the class `Graph`) can be defined to manage the storage and indexing of the `Branch` and `Node` instances which constitute the domain. The creation of instances of `Node` (or `Branch`) instances can be embedded in the Graph class, in the form of Python methods. For example a node addition method `Graph.addNode(x, y, z)` can be defined as follows:

- take spatial coordinates (x, y, z) as input;
- create a `Node` instance located as requested;
- storing a pointer to the newly created `Node` object into an internal container, namely a list `Graph.NodeList`: this implicitly assigns an identifying number to the node, corresponding to its position in the list.

This way i) any node of the network can be accessed by its unique index via the `Graph` object and ii) the variables defined on nodes can be stored into arrays of the same shape of `Graph.NodeList`, so that the variable value at any note can be accessed using its unique index.

An branch addition method `Graph.addBranch(start, end, ...)` can be defined as follows:

- take as input two node indices, as well as geometric features (length, cross section);
- create an `Branch` instance, which contains the information about geometric features and neighbour nodes indices;
- store a pointer to the newly created `Branch` object into an internal container, namely a list `Graph.BranchList`: this implicitly assigns an identifying number to the branch, corresponding to its position in the list.

The storage of the `Branch` instances into an indexed container guarantees the same benefits that were previously discussed for the case of the node container. Moreover, each `Branch` object contains information about the neighbour nodes.

Alternative methods can be also created for accessing the network elements via parsing `Graph.NodeList` or `Graph.BranchList`, e.g. based on the aforementioned *tags*.

Moreover, the `Graph` should be able to output some of the arrays required for the creation of the governing equations systems, i.e. the ones representing geometric features and connectivity. The creation of the branch-based arrays S (branches cross section), L (branches length), D_h (hydraulic diameter) is rather trivial as it is sufficient to access the corresponding attribute of each element contained in `Graph.BranchList`.

On the other hand, the generation of the incidence matrix $\mathbf{A}$ needs a slightly more complex process. For example, a method `Graph.incidence()` for the generation of the incidence matrix can be defined as follows:

- detect the length of the internal containers `Graph.NodeList` and `Graph.BranchList`, corresponding to n_n and n_b respectively;
- initialize a $n_n \times n_b$ matrix, assigning the value 0 to each element;
- cycle through the `Branch` instances stored `Graph.BranchList`;
- the processing of each branch consists in retrieving the neighbour nodes indexes, and change the incidence matrix accordingly: for the j-th branch, $i_{start,j}$ and $i_{end,j}$ are retrieved, then $\mathbf{A}(i_{start,j}, j)$ is set to 1 and $\mathbf{A}(i_{end,j}, j)$ is set to -1;
- return incidence matrix $\mathbf{A}$.

Auxiliary objects have been created also for storing the predicted values of the state variables, mapped on the competing entities set (branches for velocity U, nodes for total pressure P, temperature T and density ρ). Such objects, called `Field` objects, store the competing variable field, and can be asked to output it in the form of a `numpy` array. The values appear in the array in the same order as the corresponding branches (nodes) in `Graph.BranchList` (`Graph.NodeList`): these arrays are therefore ready to be employed in the governing equations system. The `Field` object has also been provided with an `update` method, which takes a properly shaped array as input and updates the `Field` internal values accordingly – optionally applying a pre-defined relaxation criterion, see [79] for details.

Source objects are also treated altogether by means of a customized list object: this contains the pointers to every single branch source object (see 3.9 for details) in the network. These pointers are grouped in sublists according to the branch they refer to, and the sublists are stored in the main object following the same order of the corresponding branches in `Graph.BranchList`. The sources list can manage the simultaneous update of every source, given the state variable arrays. Also, the sources list is able to ask each source for its m and k coefficients, sum those which compete to the same entity, and return a m and k lists which are ready to be employed in the governing equations.

As an example, the following Figures 3.15, 3.16, 3.17, 3.18 explain the interactions between the functions which constitute the core of the steady-state algorithm loop (see Section 3.8 for more details) and the auxiliary objects that were illustrated in the previous paragraphs.

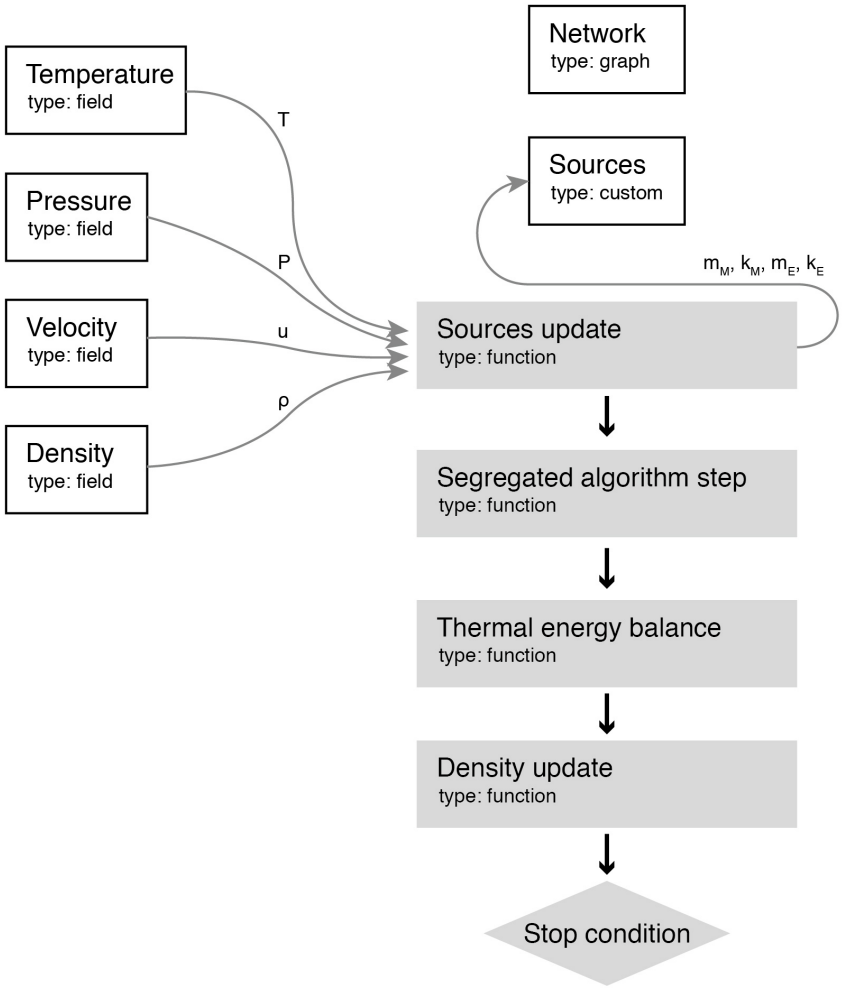

Figure 3.15: Steady solver loop flow chart: source object internal values are updated based on the current state variable arrays.

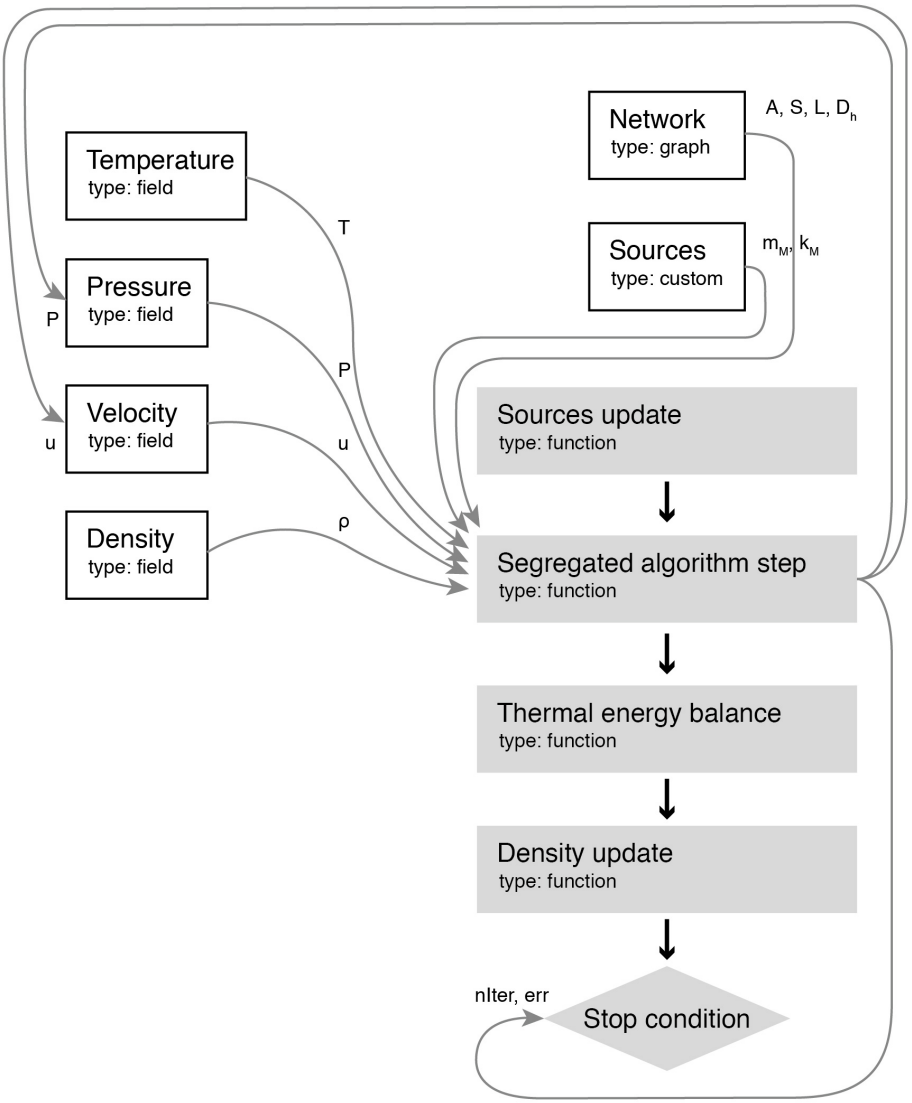

Figure 3.16: Steady solver loop flow chart: one step of the guess-correct procedure is performed. Pressure and velocity fields are updated accordingly and the magnitude of the correction is evaluated and recorded, along with the iteration count.

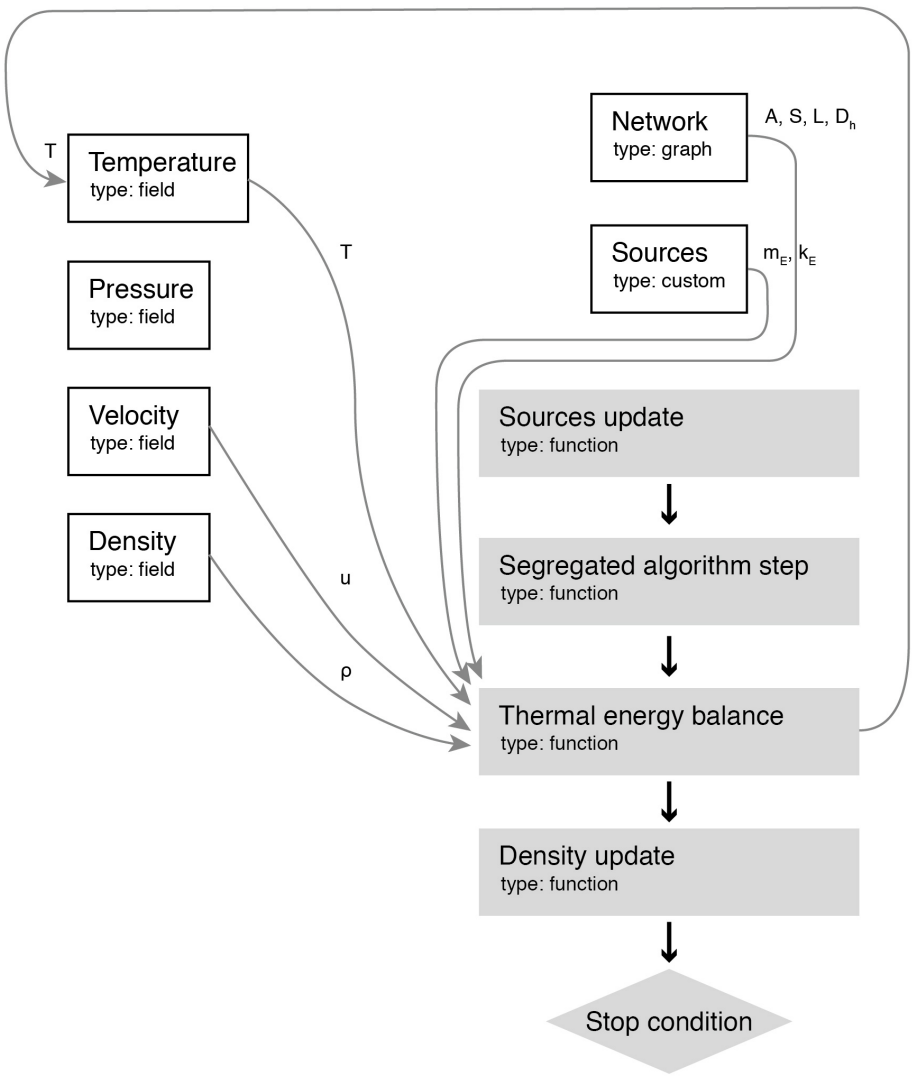

Figure 3.17: Steady solver loop flow chart: the energy balance is solved, and the temperature field is updated accordingly.

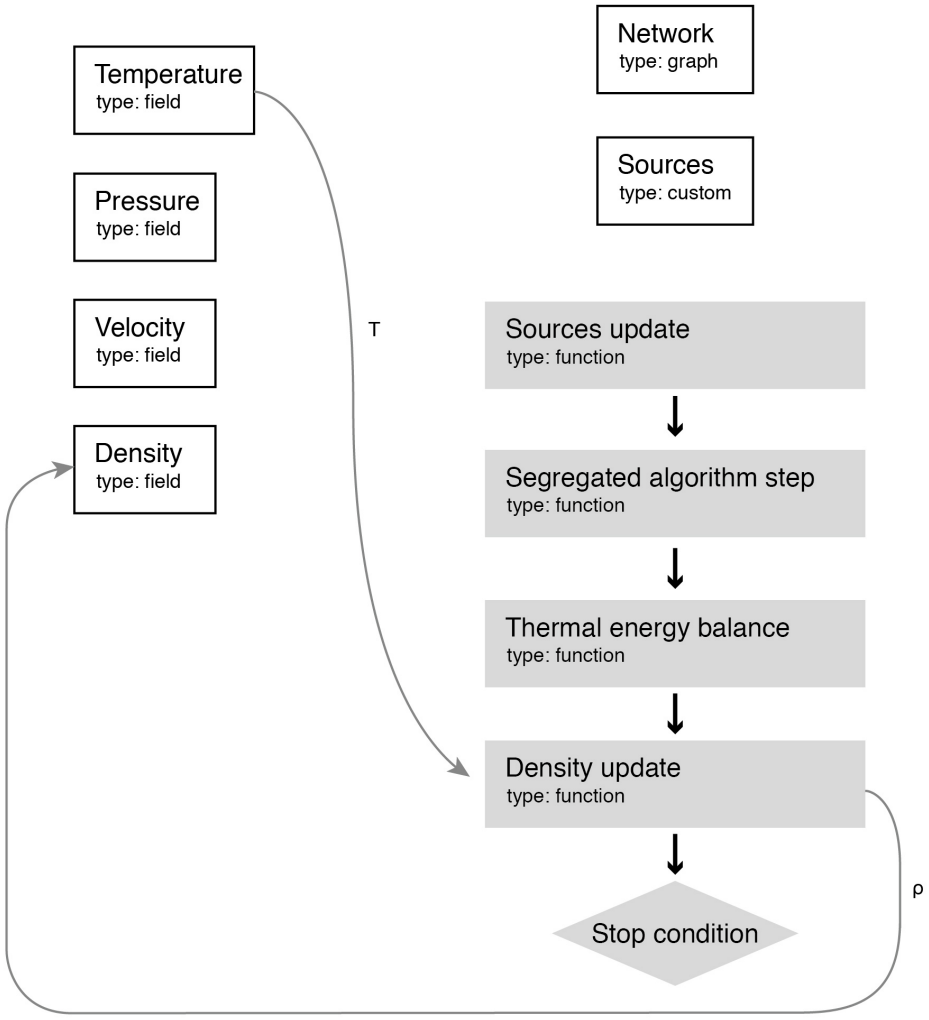

Figure 3.18: Steady solver loop flow chart: a density array is evaluated basing on the newly calculated temperature field, and used for updating the density field. Then, the stop criteria are evaluated basing on the segregated algorithm output, and the cycle is either repeated or stopped.

The object-oriented logic that was illustrated through the flow charts of Figures 3.15, 3.16, 3.17, 3.18 for the steady-state solver has been employed also for the time-dependent solver (the main differences have been highlighted in Section 3.8), as well as for the scheduling of events in transient simulations (as explained in Section 3.10). In Chapter 5, a further application of object-oriented programming will be integrated in the events scheduling logic: the modeling of the PID control action.

The current implementation, thanks to the segregation and encapsulation of the model parts, is applicable with relative ease to a large variety of similar systems. Indeed, every problem which can be represented by a network on which 1D (or 0D) transport equations are solved (e.g. heat transfer, pipe network flow, electronic circuits) could be tackled by adapting some parts of the current model to the specific application, while leaving the main object classes untouched.

Chapter 4

Model calibration

4.1 Introduction

The structure of the numerical model was thoroughly explained in the previous chapter. In order to adapt the final form of the governing equations (3.7.1), (3.7.7), (3.7.10) to the specific case of the *Mont Blanc* tunnel, the matrices and arrays composing the system have to be defined based on the corresponding features of the physical system.

Geometric features (length, section area and perimeter) of the system are known for every branch in the network, since they are relatively easy to measure and well documented. So are the characteristic curves of all the fans operating in the tunnel and in ventilation channels, as explained in Section 3.9.2. On the other hand, fluid dynamic characteristics such as friction loss coefficients are impossible to measure, at least directly. Therefore, these coefficients have to be determined by means of a calibration process, based on reliable physical data. Such process was developed on the basis of the ideas expressed in [83]. Through the next sections, the calibration process will be explained in depth:

- the parameter set to be calibrated will be chosen;
- the calibration data will be taken from the results of an extensive measurement campaign carried out by Levoni *et al.* in 2012 [14]. Such results will be also commented and post-processed to better charachterize the flow in the tunnel;
- the error, capable of evaluating the suitability of a single set of parameters values, will be defined;
- the optimization loop – in charge of guiding the generation and evaluation of new sets of values – will be set up, with a particular care on parallelization.

Lastly the results of two different calibration processes, based on two different friction models, will be discussed and employed for completing the numerical model.

4.2 Parameters choice

As explained in Chapter 2, the 1D network representing the *Mont Blanc* tunnel ventilation system is composed of 2639 nodes and 3904 branches.

The objective of the calibration is the assignment of proper friction factors to each branch of the network. However, the choice of a suitable set of parameters is a crucial issue, as increasing their number exponentially increases the number of tests necessary to obtain a proper sampling of the parameter space. For this reason the network branches have been divided in sets, so as to be able to assign a momentum sink to each branch of the network with a limited amount of conditions.

The following assumptions have been made:

- a unique friction factor value f_{tunnel} was assigned to all the branches representing the tunnel domain, in line with previous studies [78];
- a different friction factor was defined for each of the 8 AF channels ($\boldsymbol{f}_{AF}$) and for the AV channel (f_{AV}), and assigned to the corresponding branches;
- concentrated loss coefficients were defined for inlet vents (β_{vent}), open exhaust air vents (also called "traps", $\beta_{trap,open}$) and closed exhaust air vents ($\beta_{trap,shut}$) and assigned to all the corresponding branches connecting the ventilation channels to the main tunnel.

Hence, the overall number of parameters to be calibrated amounts to 13 loss coefficients.

Some additional observations on the choice of these parameters are in order. First, the definition of a concentrated loss coefficient in place of a friction factor for branches representing vents is due to the irregularity of these ducts, whose path, described in detail in Chapter 2, presents many bends and section changes, and is better represented by a single loss coefficient. Furthermore, the adoption of a loss coefficient for closed exhaust vents (which apparently sounds paradoxical) is necessary to capture the leakages occurring through these barriers, which were clearly revealed by the measured velocity profile in the last of the five measurements that will be illustred in the next Section 4.4.1. Lastly, although an estimate of the value of the friction factor of the tunnel, $f_{tunnel} = 0.0235$, had been previously estimated by Levoni *et al.* [78], such parameter has been added nevertheless to the calibration space, in order to allow for an increased flexibility of the optimization algorithm.

4.3 An alternative approach: equivalent roughness

Before committing to the use of the constant f friction model for the whole domain, a different path has been explored. An additional calibration process has been carried out, following a slightly different approach: a more complex model has been employed to dynamically calculate f during the simulation, based on local velocity. In this case, the parameter set has been chosen to be of the form:

- a unique friction factor value f_{tunnel} was assigned to all the branches representing the tunnel domain, in line with previous studies [78];
- a different equivalent roughness (ϵ) was defined for each of the 8 AF channels ($\boldsymbol{\epsilon}_{AF}$) and for the AV channel (ϵ_{AV}). Momentum sinks are created on the basis of the Swamee-Jain model, defined using ϵ and local hydraulic diameter, and then assigned to the corresponding branches;

- concentrated loss coefficients were defined for inlet vents (β_{vent}), open exhaust air vents (also called "traps", $\beta_{trap,open}$) and closed exhaust air vents ($\beta_{trap,shut}$) and assigned to all the corresponding branches connecting the ventilation channels to the main tunnel.

The momentum sinks are assigned to each branch of the network as described in section 3.9. The difference lies in the choices that were made for representing the friction losses within the ventilation ducts: in this case, the simplified constant friction factor model was put aside in favor of the Swamee-Jain equation based model. Therefore, the overall number of parameters to be calibrated is still 13, but f is calculated at every iteration, based on local velocity, for all the ventilation channels branches.

The adoption of this particular model was considered due to its higher degree of adherence to the actual physical situation. Moreover, it accounts for the section shape changes which are encountered in almost all the channels. Indeed, the Swamee-Jain formula bases on the $\frac{\epsilon}{D_h}$ ratio: assigning the same equivalent roughness (ϵ) to the whole channel would lead to a non uniform distribution of $\frac{\epsilon}{D_h}$ along the channel.

Two calibration processes, one for each set of parameters, have been carried out. Since the only difference between the process is only represented by the source object that was chosen for the ventilation channels, the upcoming discussion concerning data set, error and optimization algorithm is valid for both the calibration processes. The differences between the results of the two processes will be highlighted in the last section.

4.4 Reference data

In order to be able to perform the calibration process, the availability of a detailed and reliable dataset – capable of representing the response of the real system – is crucial. To this aim, the longitudinal velocity data set resulting from an experimental campaign previously carried out by Levoni *et al.* [14] was chosen.

4.4.1 Measurement facility

In the case of the *Mont Blanc* tunnel, and, more generally, in long mountain tunnels equipped with hybrid ventilation systems, a spatially accurate sampling of the longitudinal velocity can hardly be achieved by displacing a stationary survey rake at different locations. The variability of weather conditions at the portals could complicate the reconstruction of the correspondence between the ventilation parameters and the actual flow, since the acquisitions at different stations would be the result of different, largely unsteady boundary conditions. Moreover, such measurement campaigns are typically performed in the occasion of dedicated traffic closures, which, at best, last only a few hours, only allowing for the exploration of a limited number of positions for a single ventilation configuration.

For this reason, back in 2012, Levoni *et al.* [14] deviced a moving measurement facility which allowed for a continuous pointwise acquisition of the longitudinal velocity component over the entire tunnel length, based on the principle of aerodynamic reciprocity. The T.A.L.P.A. (Tunnel Aerolab for Longitudinal Profile Acquisition) facility, was realized by mounting the array of vane anemometers previously constructed and tested in [78] (Figure 4.1) on the chassis of a small, electrically powered go-kart (Fig. 4.2(a)), which had a negligible frontal area with respect to the tunnel section. The vehicle was equipped with a

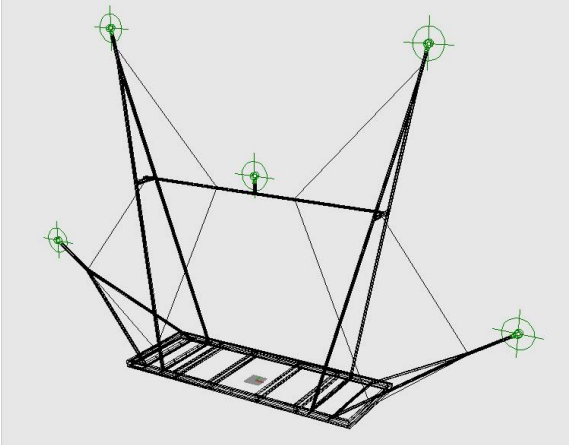

Figure 4.1: 3D mathematical model of the survey rake (from [78])

(a)  (b) 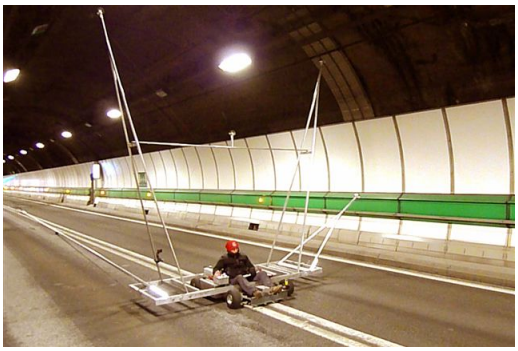

Figure 4.2: (a) The vehicle in its final layout (b) The T.A.L.P.A. facility traveling through the *Mont Blanc* tunnel during the measurement campaign. tunnel during the measurement campaign. (from [14])

very accurate cruise control system, ensuring strict constancy of the advancement speed, and with a servo-assisted steering rack, connected to a non-proportional joystick, allowing for a precise direction control.

4.4.2 Measurement campaign

The first measurement campaign performed with the T.A.L.P.A. experimental facility took place at the *Mont Blanc* tunnel the night between January 21st and 22nd, 2012 (Fig. 4.2(b)). Throughout a time span of 8 hours, five runs along the tunnel were completed. Detailed information on the five tests is reported in Tab. 4.1.

The five ventilation configurations tested were chosen so as to collect meaningful data for calibration of a simplified fluid dynamic model and to build a sufficient basis for the characterization of a number of important parameters of the ventilation system, such as the flow rate distribution and pressure loss coefficients of fresh air inlet and extraction vents, and the extent of local air jets due to the operation of axial fans. During test 1, the flow was induced by the transverse ventilation system, adding to the significant influence of the pressure difference between the tunnel ends; the rotational velocity of fans providing

Test no.	**1**	**2**	**3**	**4**	**5**
Start time [hh:mm]	23:02	00:26	01:38	02:40	04:09
Test duration [s]	2308±1	2311±1	2308±1	2311±1	2308±1
Vehicle speed [m/s]	5.031±0.002	5.024±0.002	5.031±0.002	5.024±0.002	5.031±0.002
weather data					
p_{F} [Pa]	87578±9	87581±10	87542±8	87512±7	87483±13
p_{I} [Pa]	86074±8	86045±18	85999±5	86004±10	86005±7
T_{F} [°C]	0.1±0.1	0.1±0.1	0.1±0.1	0.1±0.1	0.7±0.1
T_{I} [°C]	4.4±0.1	5.4±0.1	5.4±0.1	5.2±0.1	4.8±0.1
ventilation data					
Δp_{eff}	407±12	403±15	447±8	375±15	373±15
U_{nat} [m/s]	4.56±0.07	4.50±0.08	4.77±0.04	4.35±0.09	4.35±0.09
fresh air supply	on	on	on	on	off
setting	$n_{\mathrm{AF}} \approx 650$ rpm		$Q_{\mathrm{in,ch}} \approx 43 \div 44$ m^3/s		-
$Q_{\mathrm{in,tot}}$ [m^3/s]	371.2±3.9	374.7±5.7	344.8±5.1	351.6±6.7	-
air extraction	off	on	off	on	on
extraction stretch [m]	-	835 ÷1435	-	835 ÷1435	9035 ÷9635
$Q_{\mathrm{out,tot}}$ [m^3/s]	-	261.2±10.1	-	287.0±34.7	285.4±1.1
active jet fans	off	off	off	off	$4_{\mathrm{F}\to\mathrm{I}} + 4_{\mathrm{I}\to\mathrm{F}}$

Table 4.1: Details of the five experimental tests including average pressure and temperature values at the portals, net pressure gradient and natural draught velocity, total flow rates through the ventilation channels (inlet and outlet), settings for fresh air supply, reference metric points for the opening of extraction vents, number of active jet fans and their direction.

transverse fresh air inlet in the tunnel was kept at a constant value $n_{\mathrm{AF}} \approx 650$ rpm, with all jet fans and air extraction deactivated. Test 2 was performed with the same configuration, but with air extraction activated along a 600 meters long tunnel stretch, located in the vicinity of the French portal. Test 3 and 4 were conducted in a similar fashion, but keeping the fresh air flow rate $Q_{\mathrm{in,ch}}$ roughly constant, between 43 and 44 m^3/s, with air extraction once again activated only in the second of the two tests, i.e. test 4, along the same tunnel stretch considered for test 2. A radically different configuration was instead tested in the last run: the fresh air supply fans were completely switched off, four couples of jet fans were operated (two in each direction), and air extraction was activated along a segment 600 m long, 2 km far from the Italian portal.

4.4.3 Velocity profiles

Figures 4.3 to 4.7 report the acquired velocity data for all the five tests, after appropriate post processing. The collected time series were suitably transformed into spatial distributions by simply multiplying the time coordinate by the vehicle advancement speed. Signals of the five anemometers were then averaged, and absolute air velocity values were then obtained by subtracting the advancement speed itself. Consistently, the uncertainty strips reported in the graphs refer to the measured velocity values, and not to the absolute air velocity, which is an indirect product of the measurement process. It is worthy to point out that the device seems to be extremely responsive to local conditions, as the profiles show the appearance of regularly spaced troughs, corresponding to local enlargements of the tunnel section in presence of safety garages.

All the graphs in Figures 4.3 to 4.7 reveal the presence of a regular flow, coherent with

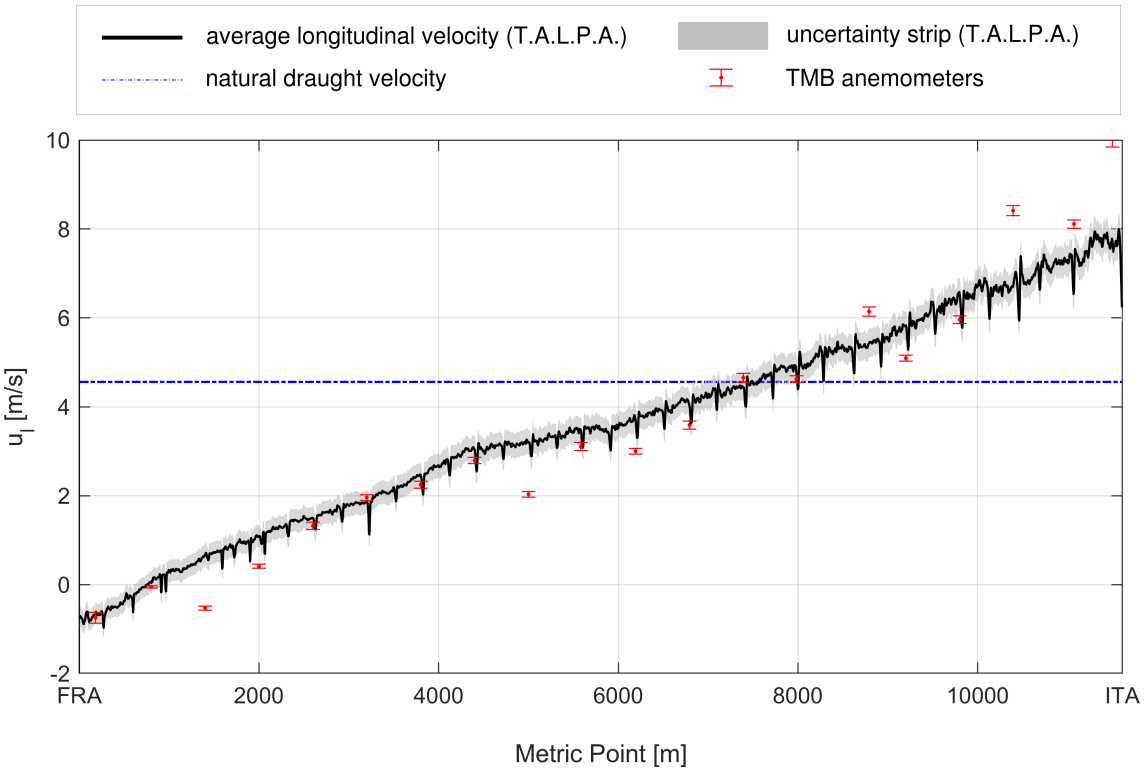

Figure 4.3: Velocity profile as a function of the longitudinal tunnel coordinate (Metric Point, PM) reconstructed for test n. 1. An uncertainty strip for present measurement is added to the graph, as well as the estimated natural draught and the velocity values measured by the 20 ultrasonic anemometers of the TMB S.C.A.D.A. system.

the specific settings of the ventilation systems and the environmental conditions outlined above. In tests 1 and 3 (Fig. 4.3 and 4.5), the flow entering through the air vents mixes with the main tunnel flow and then exits at both tunnel openings, approximately 10% out of the French side and 90% out of the Italian exit. The velocity profiles are coherent with the specific ventilation settings adopted: in test 1 (Fig. 4.3), constant rotational velocity of the fresh air fans induces different flow rates in different tunnel segments, hence different slopes in the velocity profile are in order. In test 3 (Fig. 4.5), rough constancy of the fresh air flow rate determines a more homogeneous slope of the whole velocity profile. In both tests, due to the strong pressure gradient between the two portals, the "zero velocity point" is located very close to the French exit. On the contrary, as a consequence of the activation of air extraction devices, in tests 2 and 4 (Fig. 4.4 and 4.6) the longitudinal flow is always directed towards the Italian exit and progressively accelerating, except where extraction vents are opened. As for test 5 (Fig. 4.7), the absence of transverse ventilation causes the velocity profile to be roughly constant along the whole tunnel length, with a small decrease in the direction France-Italy, due to the fact that, when the vitiated air extraction fans are switched on, a fraction of the flow rate leaks through the closed air vents. As it will be shown in part II of the present twofold work, the detection of such leakages and their correct representation in the frame of a 1D flow model is of extreme importance for the accuracy of the numerical tool itself. The regularity of the velocity profile is interrupted

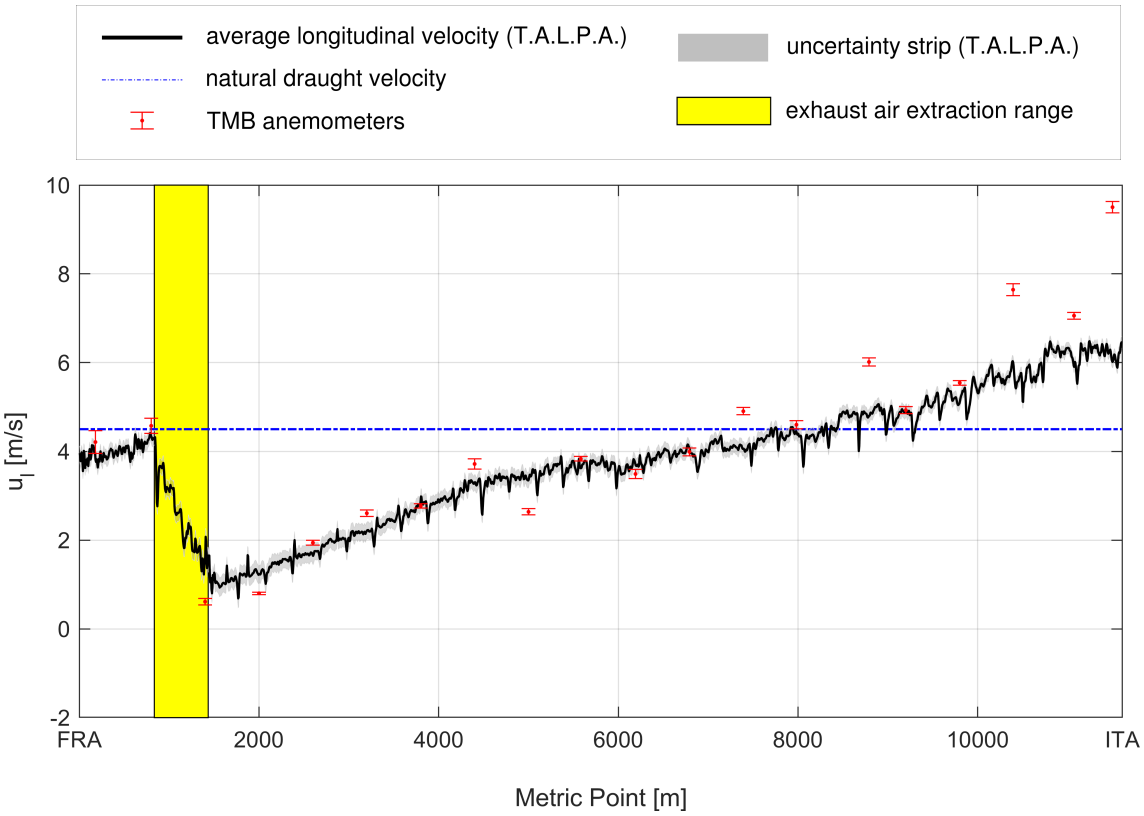

Figure 4.4: Velocity profile as a function of the longitudinal tunnel coordinate (Metric Point, PM) reconstructed for test n. 2 (see also the caption to Fig. 4.3). The tunnel stretch where air extraction takes place is highlighted in the plot.

in the air extraction area only, where, as already mentioned, velocity changes its sign, and air is drafted in from the Italian portal. Hence, it appears evident that the activation of jet fans has a significant influence only on the overall flow and not on the local average velocity values, as also observed in [78].

Figures 4.3 to 4.7 also bring forth a comparison between the present measurements and longitudinal velocity values acquired simultaneously by the 20 ultrasonic anemometers of the TMB S.C.A.D.A. (Supervisory Control And Data Acquisition) system, installed on the tunnel ceiling [78]. The two data sets present a satisfactory general agreement, both in terms of global trend and of local values. However, some of the TMB data show significant deviations with respect to the overall tendency depicted by present tests. In some cases, such deviations are systematic and do not depend on the specific ventilation configuration. These local discrepancies have already been discussed in [78], where they were ascribed either to inaccuracy of the probes or to a peculiar installation position (such as in the wake of protruding objects). In some cases, it is the complexity of the flow on the specific sections which could cause a bias in the measurements of the TMB anemometers: this is the case of test 5, where active jet fans determine a local increase in the longitudinal velocity near the tunnel ceiling, which is captured by the ultrasonic anemometers (Fig. 4.7), but it is not representative of the actual mean flow.

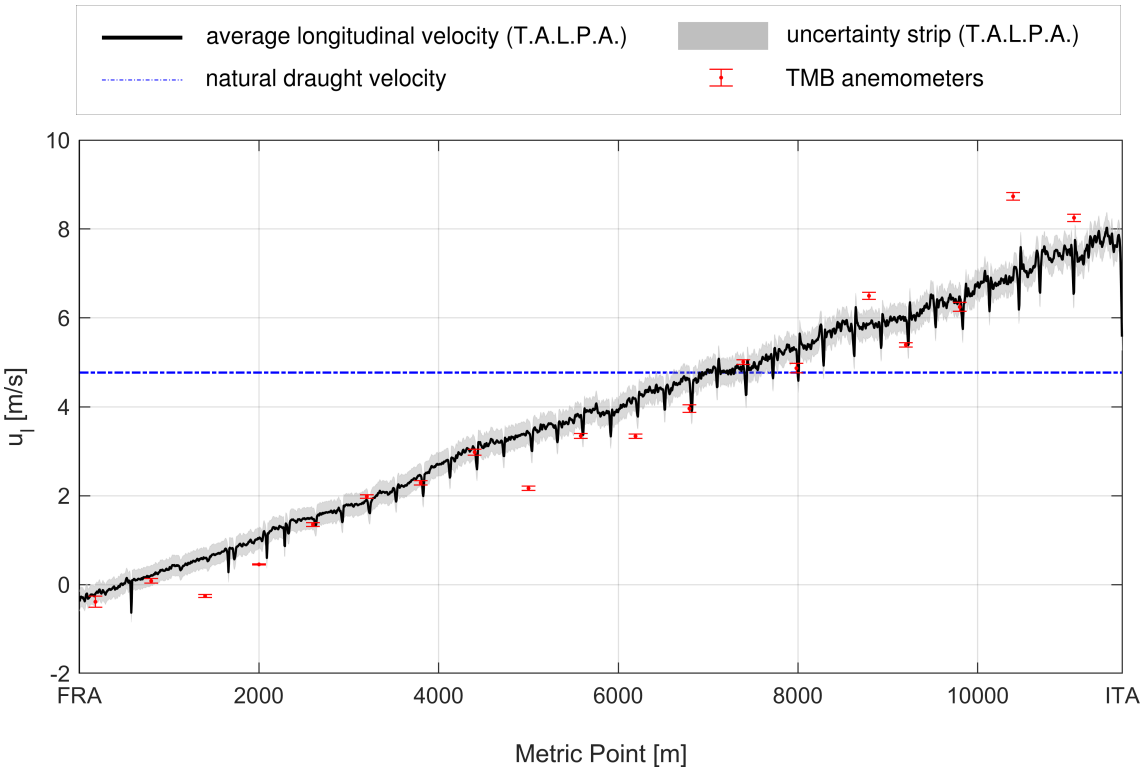

Figure 4.5: Velocity profile as a function of the longitudinal tunnel coordinate (Metric Point, PM) reconstructed for test n. 3 (see also the caption to Fig. 4.3).

4.4.4 Natural draught

As reported in Tab. 4.1, the barometric pressure recorded at the two portals remained fairly constant during each test, with deviations of less than 15 Pa. On the other hand, the weather conditions during the measurement night were such that a significant natural draught ensued in the tunnel. As it will be shown, such a flow component crucially influenced the resulting velocity profiles established for each of the five tested configurations. Thus, an a posteriori estimate was carried out to evaluate the average velocity that would establish in the tunnel during each test, due to the sole effective pressure gradient Δp_{eff}. The latter can be defined as the pressure difference between the two tunnel ends minus the overall hydrostatic load [78]:.

$$\Delta p_{\text{eff}} = p_{\text{F}} - p_{\text{I}} - g \int_0^{L_t} \rho \sin\theta dx \tag{4.4.1}$$

where p_{F}, p_{I} are the absolute pressure values measured by the weather stations at the portals, $g = 9.798$ m/s^2 is the gravitational acceleration, θ is the slope angle of the tunnel, L_t the tunnel length and x the longitudinal coordinate (also called Metric Point or PM throughout the present discussion). The calculated values of Δp_{eff} are reported in Tab. 4.1 and range between 373 Pa (test n.5) and 447 Pa (test n.3). Such values amount approximately to 50-60% of the limit value (750 Pa) beyond which traffic is stopped at the *Mont Blanc* tunnel and, thus, confirm the presence of a strong natural flow component. The resulting natural velocity was calculated by using the 0D model for longitudinal ventilation

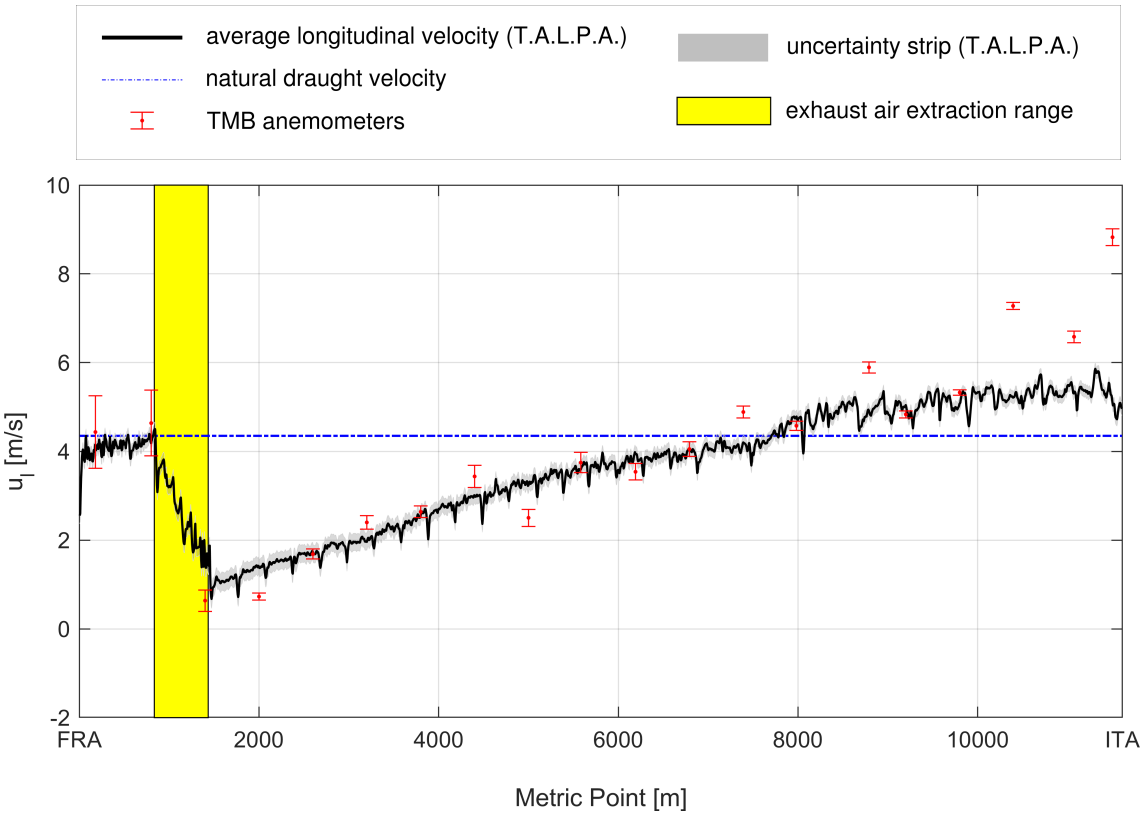

Figure 4.6: Velocity profile as a function of the longitudinal tunnel coordinate (Metric Point, PM) reconstructed for test n. 4 (see also the caption to Figures 4.3 and 4.4).

derived in [78], by assuming steady-state conditions:

$$u_{nat} = \sqrt{\frac{2\Delta p_{\text{eff}}}{\rho_{\text{ave}}\left[\frac{\rho_{\text{ave}}}{\rho_{\text{in}}}(k_{\text{in}}+1)+\frac{fL_t}{D_h}\right]}} \tag{4.4.2}$$

where: k_{in} and f are the concentrated loss coefficient at the inlet and the tunnel friction factor, respectively; D_h is the hydraulic diameter of the tunnel; ρ_{ave} and ρ_{in} are the density values calculated at the average temperature in the tunnel and at the tunnel end where the natural flow enters the tunnel (in the present case, the French portal), respectively. Values of friction coefficients f and k_{in} have been taken from the results of Levoni *et al.* [78]. Concerning the calculation of density, the ideal gas law with a fixed reference pressure was used (see again [78]). While a broad estimate of the temperature profile inside the tunnel could be a reasonable choice for the estimation of the average density [84] and, also, of the integral term of (4.4.1), a more accurate calculation was made possible by the continuous acquisition of temperature by means of a thermocouple mounted aboard the T.A.L.P.A. vehicle. The acquired temperature profiles during all the five tests are displayed in Fig. 4.8.

The velocity values associated with natural draught are reported in Tab. 4.1, and plotted along with the measured velocity profiles in Figures 4.3 to 4.7. Calculated values range from a minimum of 4.35 m/s (test n. 4 and 5) to a maximum of 4.77 m/s (test n. 3). It is worth to note that the temperature distributions, which have a crucial impact on the

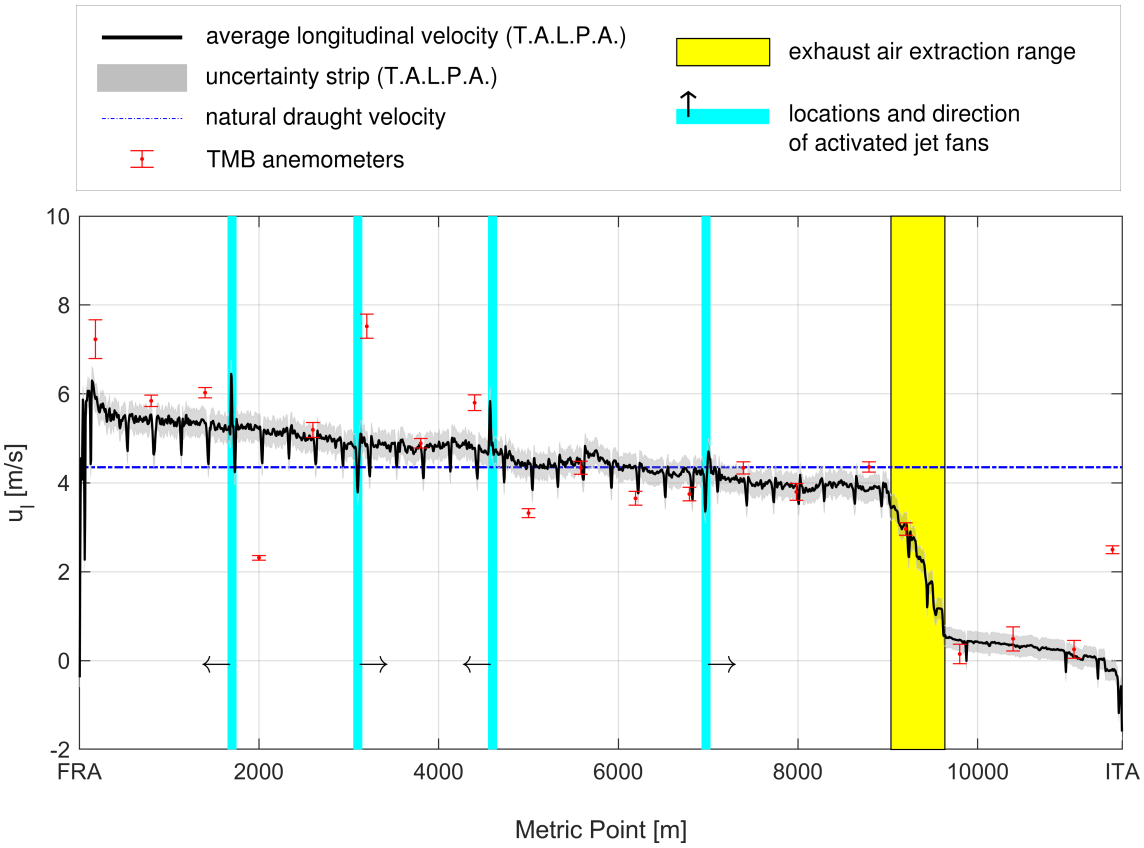

Figure 4.7: Velocity profile as a function of the longitudinal tunnel coordinate (Metric Point, PM) reconstructed for test n. 5 (see also the caption to to Figures 4.3 and 4.4). Locations and direction of activated jet fans are also added to the plot.

entity of the hydrostatic load, are significantly influenced by the ventilation configurations. For instance, Fig. 4.8 clearly shows that in test 1 and 3, where, as shown in Figures 4.3 and 4.5, air exits from both portals, temperature at both tunnel ends is higher than the outside temperature. This is due to the fact that the air blown by fresh air fans is preheated while passing through the AF channels (see Fig. 2.1) before entering the tunnel. On the other hand, during tests 2 and 4, air enters from the French portal and exits from the Italian portal (see Figures 4.4 and 4.6): hence, air temperature at the inlet section is closer to the value recorded at the portal, and increases almost monotonically along the longitudinal coordinate, with only a slight decrease due to mixing with cooler fresh air near the Italian exit. Finally, the absence of fresh air supply in Test 5, adding up to the air extraction, causes the air to enter the tunnel at both portals (Figures 4.7); this results in a sharper temperature distribution, the values at tunnel ends being closer to those recorded by the TMB weather stations.

Despite the evident connection between the available temperature data and the ventilation setup, which does not reflect, in general, the temperature profile one would obtain with the sole contribution of natural draught, such data were equally used to estimate natural flow velocity for each test. Nevertheless, these estimates can be considered as equally representative of the natural draught effect and be useful to interpret the velocity

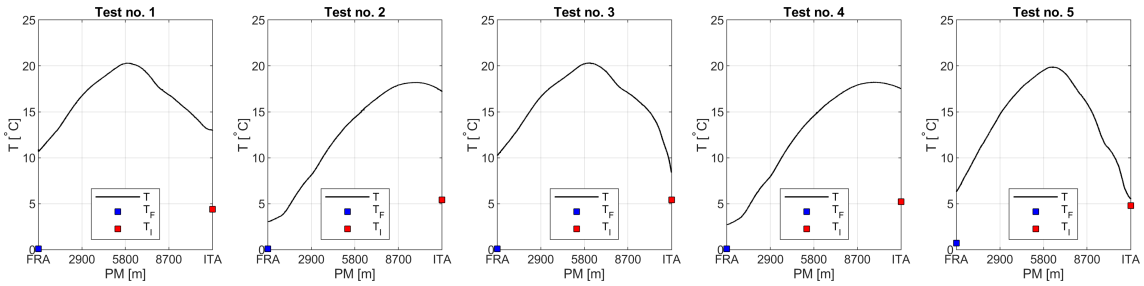

Figure 4.8: Temperature profile as a function of the longitudinal tunnel coordinate (Metric Point, PM) recorded during the five T.A.L.P.A. runs.

distributions resulting from the different ventilation configurations.

4.5 Error definition

The idea behind the definition of the objective function (which the optimization process will aim to minimize) is to compute the sum of square deviations between the calculated and measured velocity values on 1161 points uniformly spread along the main tunnel. In this case the number of points of comparison is dictated by the refinement of the partition of the main tunnel in the numerical model.

As the experimental data (presented at the previous section) refer to the five different acquisitions, the test suite has been set up such that, given a set of values of 13 parameters, five subsequent calculations are run. Then the error is calaculated on the results of each simulation, and then summed to represent an overall error value. The calibration process is then carried out as an optimization aimed at finding the set of parameters which minimizes such value.

$$\sum_{i=1}^{5}\sum_{j=1}^{1161}(U_{j,exp}-U_{j,calc})_i^2 \tag{4.5.1}$$

It has to be taken into account that some parameter sets may lead to divergent systems – this happens, for example, in presence of a connected path with very low friction losses which connects the two portals. In case of missed convergence of a simulation the function was set to output to the value 10^8 (while randomly chosen sets of parameters lead to errors of the order of $10^3 \div 10^4$) to disadvantage the parameter set through which caused the problem. Such a strategy, although having been proven successful to eliminate invalid parameters sets during the very first iterations, introduces irregular peaks in the evaluations of the objective function.

4.6 Algorithm and hyperparameters choice

Being the error far from linear, and likely to show a number of local minimum points, gradient methods ought to be excluded. Moreover, possible discontinuities due to occasional missed convergence of the calculations would compromise the correct evaluation of gradients.

Hence, the problem solution should employ a stochastic method, at least for a first phase of space exploration; to this aim, DES (derandomized evolution strategy) is a suitable choice, thanks to its versatility. Since evolutionary methods rely on the mutation operator rather than on cross-over and thus promote an explorative behaviour, these are convenient tools if a wide scan on the possible parameter combinations is a priority.

A Latin Hypercube Design of Experiments (DOE) [83] has been set up first to generate an initial population of 120 individuals, i.e. 120 sets of the input parameters to be calibrated. The range of values the variables can assume in the initial DOE is restricted and generally small, and it can be changed for the subsequent optimization process, if needed.

The design space, represented by the ranges of variability of each calibration parameter, is reported in Table 4.2 for the two calibration processes. The ranges chosen for the generation of the initial population have been extended for the optimization process to allow a wider exploration.

After the initial population has been generated, the optimization procedure starts. At each step, the algorithm selects a number of sets made of a main parent (its attributes

Variable	DOE range	Optimization range
$\boldsymbol{f}_{AF}$	[0.001, 0.01]	[10^{-6}, 1]
f_{AV}	[0.001, 0.01]	[10^{-6}, 1]
$\beta_{trap,open}$	[1, 40]	[0.1, 150]
$\beta_{trap,shut}$	[10^3, 10^4]	[500, 15000]
β_{vent}	[1, 40]	[0.1, 150]
f_{tunnel}	[0.01, 0.05]	[0.001, 0.1]

Variable	DOE range	Optimization range
$\boldsymbol{\epsilon}_{AF}$	[0.0001, 0.01]	[10^{-8}, 1]
ϵ_{AV}	[0.0001, 0.01]	[10^{-8}, 1]
$\beta_{trap,open}$	[1, 40]	[0.1, 150]
$\beta_{trap,shut}$	[10^3, 10^4]	[500, 15000]
β_{vent}	[1, 40]	[0.1, 150]
f_{tunnel}	[0.01, 0.05]	[0.001, 0.1]

Table 4.2: Parameters range for DOE and optimization processeses.

Parameter	Value
f_{AF-1F}	1.93×10^{-2}
f_{AF-2F}	9.42×10^{-3}
f_{AF-3F}	1.50×10^{-3}
f_{AF-4F}	1.29×10^{-1}
f_{AF-1I}	4.67×10^{-5}
f_{AF-2I}	4.96×10^{-3}
f_{AF-3I}	1.42×10^{-2}
f_{AF-4I}	1.90×10^{-2}
f_{AV}	3.97×10^{-2}
$\beta_{trap,open}$	13.3
$\beta_{trap,shut}$	1.96×10^{3}
β_{vent}	72.6
f_{tunnel}	2.55×10^{-2}

Case id	RMS deviation [m/s]
1	0.20
2	0.31
3	0.17
4	0.29
5	0.30

Parameter	Value
ϵ_{AF-1F}	1.02×10^{-2}
ϵ_{AF-2F}	1.12×10^{-8}
ϵ_{AF-3F}	1.00×10^{-8}
ϵ_{AF-4F}	2.60×10^{-1}
ϵ_{AF-1I}	1.01×10^{-8}
ϵ_{AF-2I}	1.01×10^{-8}
ϵ_{AF-3I}	1.16×10^{-3}
ϵ_{AF-4I}	5.01×10^{-3}
ϵ_{AV}	2.82×10^{-2}
$\beta_{trap,open}$	13.0
$\beta_{trap,shut}$	2.11×10^{3}
β_{vent}	43.8
f_{tunnel}	2.54×10^{-2}

Case id	RMS deviation [m/s]
1	0.21
2	0.31
3	0.17
4	0.29
5	0.29

Table 4.3: Calibrated parameter set (left), RMS deviation for each of the 5 cases (right).

vector being called x_i) and three other individuals (x_a, x_b, x_c), and proceeds to the creation of mutant individuals v_i of the form:

$$v_i = x_i + K(x_a - x_i) + F(x_b - x_c) \tag{4.6.1}$$

Within equation (4.6.1), two perturbations are applied to the parent individual attributes: one based on the difference, in terms of each attribute, calculated between the parent and another individual of his generation, and another based on the comparison of two other individuals of the same generation. The magnitude of such perturbations is controlled by two coefficients: F – called scaling factor – and K – combination factor. Both K and M were set to 0.8.

In order to create the new individual, then, v_i undergoes a cross-over with its parent x_i, with the cross-over constant C being the probability that the mutant phenotype will be chosen. C was set to 0.9.

The probability for a sample of being selected for generation is proportional to its fitness function. The chosen selection method follows a roulette wheel approach: the probability of being selected for the best individual in the population is P times larger than that for the worst. P, called roulette wheel selection probability bias, has been set to 3 for the first 120000 individuals and was then increased to 3.5. This is due to the fact that it is better – at an initial stage – to privilege space exploration, while favouring the fittest individuals at an advanced stage may help reaching an optimum solution quicker. The procedure stops after a prescribed number of total individuals evaluated is reached, and the optimum solution is singled out based on the values of the objective function.

4.6.1 Parallel implementation

It is worth to mention that at each generation step, within the optimization process, the most computationally demanding part is the evaluation of the fitness of the individuals. Such evaluations are independent from each other, thus a parallel implementation of the process led to notable savings in terms of computational time. Since the rest of the operations at each step are computationally very light, employing 120 CPUs one full optimization step would take almost the same time of the slowest of steady calculation processes it involves.

The current implementation derives from the simplification and parallelization of a the DES implementation integrated in the software *Optim*, a Python multischeme optimization algorithm devised and developed by Cavazzuti [83].

4.7 Calibration Results

Both the calibration processes has taken 2,500 generations of 120 individuals each, for a total of 300,000 evaluations of the objective function. Each evaluation, in turn, required five simulation runs.

The best fits of the parameter sets, as determined by the optimization algorithm, are reported in Table 4.3. RMS deviations from experimental data, for each of the five simulations associated to the experimental tests, are added on the side of the parameters tables.

Figures 4.9 to 4.13 show the longitudinal air velocity profile, as predicted by the calibrated models, for each of the five benchmark cases considered, alongside with the velocity

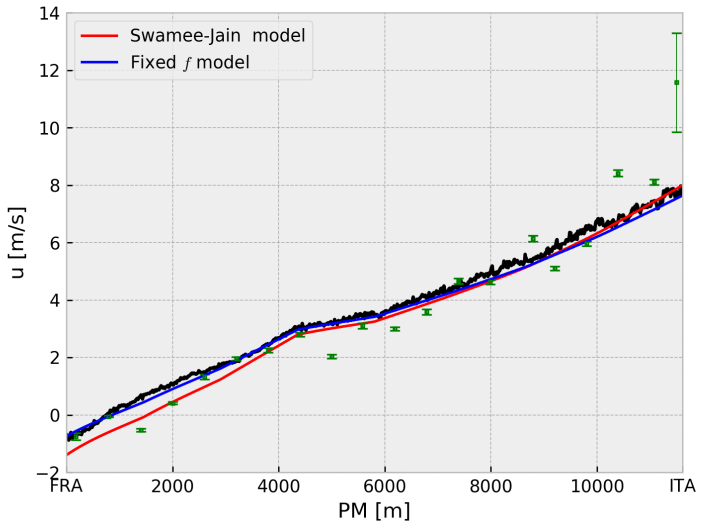

Figure 4.9: Comparison between velocity profiles in Test 1: calculated with constant f model (blue), calculated with Swamee-Jain model (red), measured (black). Pointwise velocity measurements taken by the tunnel anemometers (green) are also plotted.

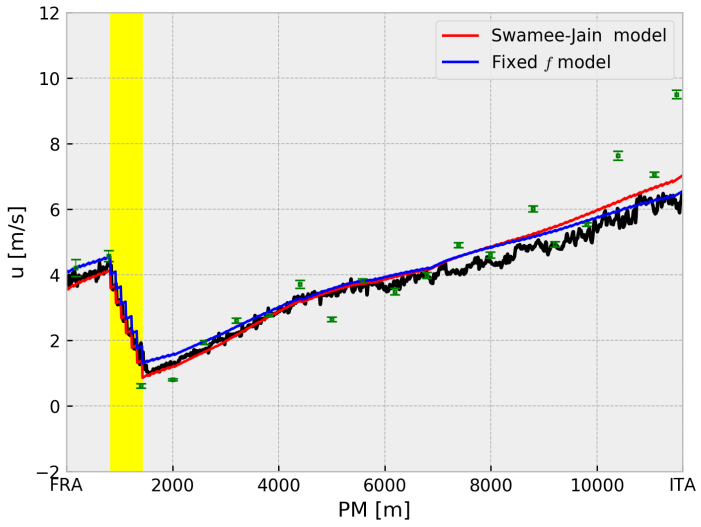

Figure 4.10: Comparison between velocity profiles in Test 2: calculated with constant f model (blue), calculated with Swamee-Jain model (red), measured (black). Pointwise velocity measurements taken by the tunnel anemometers (green) are also plotted.

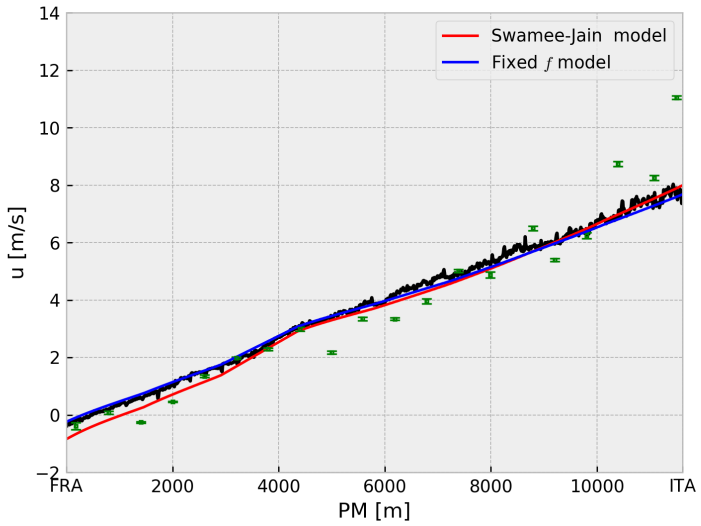

Figure 4.11: Comparison between velocity profiles in Test 3: calculated with constant f model (blue), calculated with Swamee-Jain model (red), measured (black). Pointwise velocity measurements taken by the tunnel anemometers (red) are also plotted.

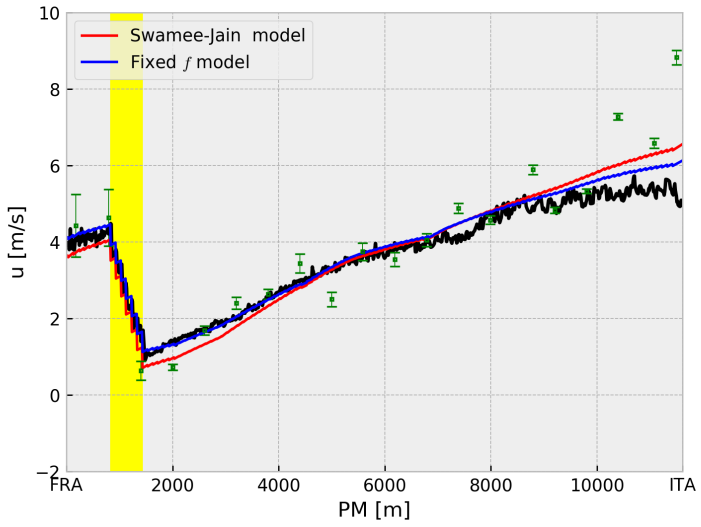

Figure 4.12: Comparison between velocity profiles in Test 4: calculated with constant f model (blue), calculated with Swamee-Jain model (red), measured (black). Pointwise velocity measurements taken by the tunnel anemometers (green) are also plotted.

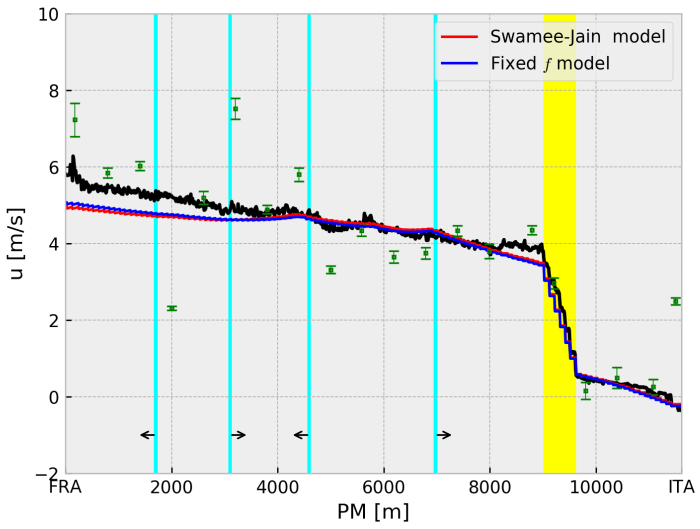

Figure 4.13: Comparison between velocity profiles in Test 5: calculated with constant f model (blue), calculated with Swamee-Jain model (red), measured (black). Pointwise velocity measurements taken by the tunnel anemometers (green) are also plotted.

profiles measured by the T.A.L.P.A. facility. Velocity data simultaneously measured by the fixed anemometers permanently installed in the tunnel are also added to the graphs for further reference.

The background is coloured in yellow along the 600 m section in which the extraction vents are open, in case the extraction system is active.

The tunnel streaks where a jet-fan couple is active are highlighted by a blue background, along with an arrow indicating its direction.

Both model responses to the calibration process can be viewed as satisfactory, according to the results reported in Figures 4.9 to 4.13. Although slight differences between calculated and measured profiles can be observed, especially for the cases where the extraction system was turned on (tests 2, 4 and 5), the overall profile shape and slope changes are captured accurately.

As it can be seen in Table 4.3, the differences between the performances of the two calibrated models are really small and they would eventually balance out if an overall performance was to be calculated on the 5 tests.

It is worthy to point out that velocity measurements close to the Italian portal ($x = 11611$) have been found to be affected by a greater degree of noise: this can be also evinced by the significant deviation that can be observed between present experimental data and the values given by the TMB fixed-point anemometers. Unsurprisingly, the highest deviation between numerical results and benchmark measurement data also generally occurs in that region.

The tunnel friction factor f_{tunnel} as estimated by the optimization process is in both cases consistent with the result obtained in a previous calibration of a 0D model [78]. In fact, the calibrated value, $f = 0.0255$, differs by less than 8% from the result of the previous study, $f = 0.0235$, thus corroborating the validity of the chosen modeling and calibration

approach.

For concerning the values of the parameters composing the optimal sets, $\beta_{trap,shut}$, $\beta_{trap,open}$ e f_{tunnel} are consistent within the two optimization processes. On the other hand, when employing the Swamee-Jain model, the optimal equivalent roughness of four of the ventilation channels is of the order of 10^{-8} – which is the minimum value allowed by the previously established parameters limits.

Since the coefficient values resulting from the calibration which employed the constant f model are better contained into the calibration range, it is reasonable to adopt this model for the numerical representation of the *Mont Blanc* tunnel.

This model, despite its relative simplicity, represents the behavior of the real tunnel with the same accuracy of the more complex Swamee-Jain equations. It is also true that for flows with high Reynolds numbers $f(Re, \epsilon/D_h) \approx f(\epsilon/D_h)$. The flows within the most of the domain, given the order of magnitude of the hydraulic diameters and the average operation flowrates, are usually highly turbulent. Hence it is reasonable to assume that the choice of f over ϵ as a friction parameter implies negligible differences.

4.8 Steady state validation tests

The numerical results obtained on the benchmark calibration cases are surely encouraging, but do not prove thoroughly the reliability of the model on the full spectrum of working conditions which can take place in the physical tunnel. An extra pool of data, *unknown* to the model, is required for a proper model validation. The tunnel control system keeps a record of the flow and boundary conditions, as measured during emergency events or extraction system trial runs: such data constitutes an ideal choice for full model validation.

To the extent of the present study, the comparison has been performed only between steady-state numerical simulations and velocity measurements taken from the *Mont Blanc* tunnel database, collected at selected dates and times. Such are chosen according to the velocity profile changes encountered while comparing the velocities with the values measured at the previous and subsequent instants, privileging the steadiest. More details on the experimental data can be found in Table 4.4.

As it can be observed in Fig. 4.14, the numerical model provides a satisfactory approximation if the calculated velocity profile is compared to the local values measured by the tunnel anemometers. Comparing then the output of the numerical model with the velocity profile as calculated by the tunnel control system *SCADA* (which uses the flow rates measured in the ventilation ducts for obtaining the profile shape, and then fits the profile based on the values collected by the anemometers), although small local deviations are present, the overall trend is always successfully captured.

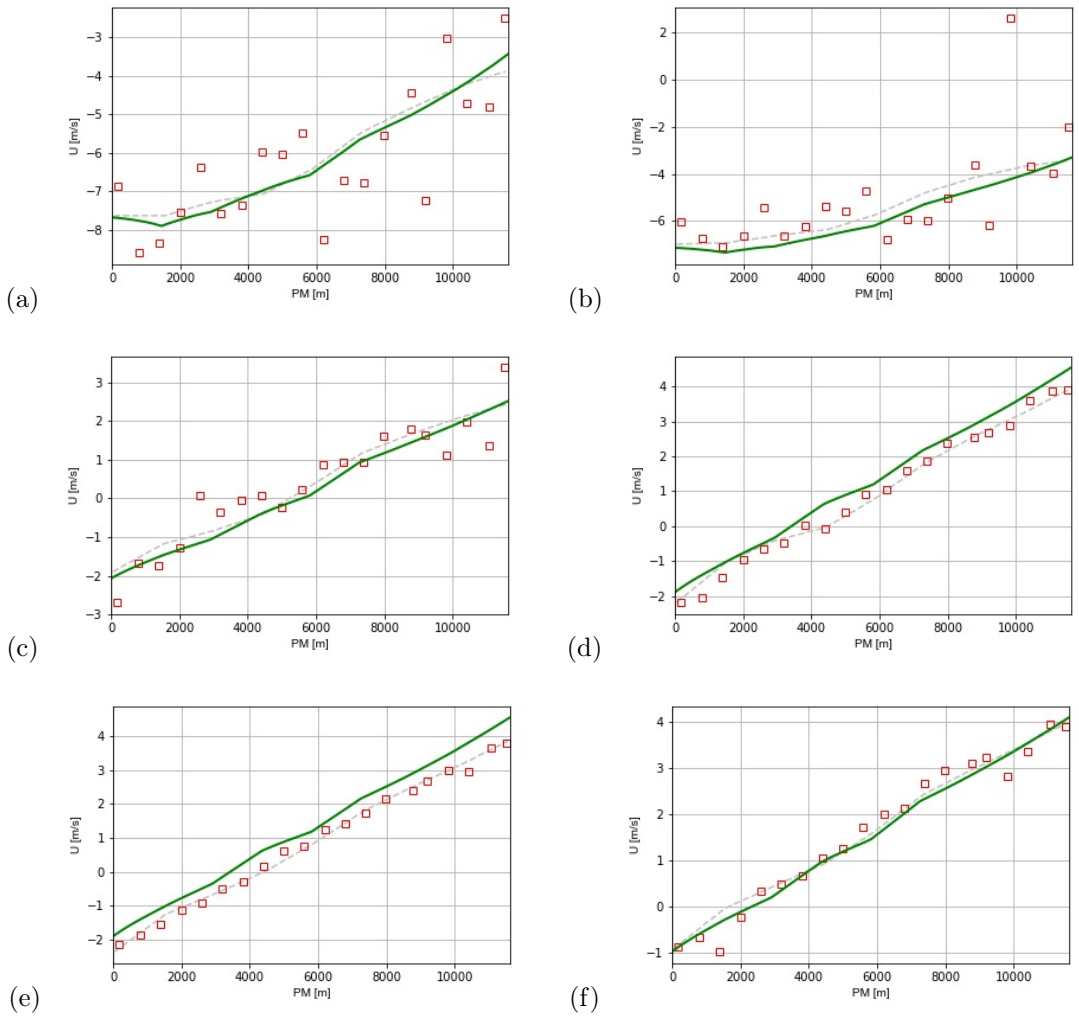

Figure 4.14: Validation of the algorithm against experimental data provided from the fixed sensors installed in the tunnel, on different occasions. Green line: calculated velocity profile. Gray dotted line: velocity profile as calculated by the tunnel control system (SCADA). Red squares: local velocity as measured by fixed anemometers. (a) 2018-03-01 03:37:00, $\Delta p = -850.59$ Pa (b) 2018-03-01 06:12:41, $\Delta p = -746.49$ Pa (c) 2018-10-07 14:15:30, $\Delta p = 29.59$ Pa (d) 2019-04-09 05:40:45, $\Delta p = 117.21$ Pa (e) 2019-05-16 16:13:46, $\Delta p = 116.69$ Pa (f) 2019-05-27 23:29:27, $\Delta p = 117.46$ Pa

Test no.	**1**	**2**	**3**	**4**	**5**	**6**
Date [yyyy-mm-gg]	2018-03-01	2018-03-01	2018-10-07	2019-04-09	2019-05-16	2019-05-27
Time [hh:mm:ss]	03:37:00	06:12:41	14:15:30	5:40:45	16:13:46	23:29:27
ventilation data						
Δp_{eff} [Pa]	-850.59	-746.49	29.59	117.21	116.69	117.46
$n_{AV,F}$ [rpm]	0	0	0	0	0	0
$n_{AV,I}$ [rpm]	0	0	0	0	0	0
$n_{AF1,F}$ [rpm]	0	0	329	478	479	378
$n_{AF2,F}$ [rpm]	300	250	250	400	399	299
$n_{AF3,F}$ [rpm]	378	329	330	480	479	379
$n_{AF4,F}$ [rpm]	702	706	692	805	805	705
$n_{AF1,I}$ [rpm]	330	280	278	432	428	329
$n_{AF2,I}$ [rpm]	338	289	288	441	439	341
$n_{AF3,I}$ [rpm]	330	330	330	479	478	379
$n_{AF4,I}$ [rpm]	598	599	600	700	699	600

Table 4.4: Details of the data base events that were chosen for the validation.

Chapter 5

Validation in unsteady condidions

5.1 Introduction

Following the process explained in the previous chapters a numerical model of the TMB tunnel was implemented, and calibrated on the base of reliable data aquired from the physical network. Steady-state simulations were employed for the definition of a test unit, which in turn constitutes the "probe" employed by the calibration algorithm: this is called, within the main optimization cycle, to evaluate the response of the model to parameter changes.

Once the friction coefficients are calibrated and the model is therefore capable of making accurate predictions on known steady scenarios, unsteady simulations may be run as well. Arguably, no further parameter calibration is required in order to extend the simulation in the time domain.

The time derivative terms defined within the governing equations (their final forms (3.7.1), (3.7.7), (3.7.10) may be found in Chapter 3), that were neglected for the steady-state simulation, are in charge of accounting the system inertia.

A dynamic approach was developed for controlling the time dependent behavior of some of the sources and sinks in the system (Chapter 3, Section 3.10). Such an approach is adequate for representing the activation of centrifugal fans, as well as the opening and closing of extraction vents: it almost covers the whole gap between steady and unsteady simulations.

Yet, one matter still needs to be addressed in order to fully represent the system behavior in emergency conditions: as explained in Chapter 2 the activation of jet fans is automatically determined on the run by a PID control.

5.1.1 PID control

A proportional-integral-derivative controller (PID controller) is a widely used control loop feedback mechanism. It calculates an *error value* $e(t)$ as the difference between a measured process variable and a desired setpoint. The controller attempts to minimize the error by adjusting one of the process control inputs. A good example of application of a similar control is an oven thermostat: given a desired set temperature, according to the measured internal temperature of the oven, the control can set the power delivered to a resistive heater.

The PID controller calculates its *correction value* $y(t)$ employing a relatively simple equation:

$$y(t) = K_P e(t) + K_I \int_0^t e(t')dt' + K_D \frac{de(t)}{dt} \tag{5.1.1}$$

where K_P, K_I and K_D are non negative coefficients for the proportional, integral and derivative terms. Such coefficients fully define the PID control and must be chosen carefully according to the application.

In the case of the *Mont Blanc* tunnel the process value sent to the PID control is the velocity value at the fire event location, which is estimated by the SCADA based on the values of flow rates within the ventilantion channels and the measurements of 20 fixed anemometers. The set point employed for the calculation of the *error value* is defined as null velocity at the event location.

The *correction value* calculated by the PID control represents the requested amount of working jet fan couples; its sign represents the working direction of such fans (by the usual convention assigning positive sign to FRA $\rightarrow$ ITA and negative sign to FRA $\leftarrow$ ITA).

As previously stated in Chapter 2, Levoni *et al.* [75] established that jet fans don't have a significant local influence on the flow; instead, they influence the overall velocity profile of the tunnel by shifting it upwards or downwards. For this reason, a PID control – which only outputs an signed integer number – is enough to address the issue: it is not relevant which ones of the 38 couples of axial fans are activated (as long as they are not located in the proximity of the event).

The coefficients of the PID control embedded in the *Mont Blanc* tunnel ventilation system were optimized on the basis of numerical simulations performed by means of the 0D model developed by Levoni *et al.* [75]. The values of such coefficients are not reported in the present work as they are intellectual property of GEIE TMB. Nonetheless, it can be said that the derivative coefficient K_D is much smaller than the proportional and integral K_P e K_I ones, in order to limit the effect of spurious fluctuations of the input value $e(t)$ (the estimated velocity at the fire location) on the output of the PID control. Therefore, the overall action of the PID control employed in the *Mont Blanc* tunnel resembles more that of a proportional-integral (PI) control.

5.1.2 Jet fans management in the numerical model

The event based logic explained in Chapter 3, Section 3.10, has been implemented in the present numerical model by means of an object that has been defined as *Event Manager*, which incorporates a numerical PID controller. The *Event Manager* takes action at the very beginning of each iteration of the time cycle: right after the "ticking" of the imaginary clock, and right before the start of any calculation for the current time step. The action simply consists in checking if any *event* is scheduled for the current timestep: if so, it triggers the events.

So, given a sorted sequence of events equipped with their activation time, a relatively simple object can perform pre-defined actions at the correct time. In order to account the automatic activation of jet fans, which is decided on the run based on the system state, this approach requires the introduction of one further object. Such object will be from now on called *Jet Fans Manager*, as it is in charge of receiving a command (which is only

consisting of an integer value in our case) from an external control, and applying it on the jet fan group.

The *Jet Fans Manager* has been designed to include a list of pointers: each pointer gives access to a specific source object corresponding to each of the jet-fans. The event metric point is provided to the *Jet Fans Manager* during the initialization, allowing it to exclude from the list the fans that are located within the tunnel stretch with open extraction vents.

The *Jet Fans Manager* takes action right before the *Event Manager*, so it is now the first object that is called within an external iteration. In the case of the TMB tunnel the PID controller produces a new output every 10 seconds: therefore the first task of the *Jet Fans Manager* is to check, according to the current time, if the external controller should be queried.

Each time the numerical PID control is queried, the *Jet Fans Manager* receives a signed integer number, representing the requested amount of working jet fan couples. The *Jet Fans Manager* evaluates the state of each fan couple included in its internal list of pointers. At this point, a number of jet fans need to be turned on or off to match the difference between the requested jet fan amount and the current jet fan amount. For enforcing the activation commands, the *Jet Fans Manager* creates instances of *event* objects, containing the information about the nature of action to be performed and its target. The resulting *events* are scheduled for the current time, and added on top of the event list administrated by the *Event Manager*. As soon as the *Jet Fans Manager* ceases its action for the current timestep, the upcoming action of the *Event Manager* addresses the newly created events, thus completing the application of the jet fans management logic.

Some limits can be enforced in the modeled version of the control system in order to match it better with the control system of the TMB tunnel. For example, a limit is set on the number of jet fans that can be activated within a certain time interval: the *Jet Fans Manager* changes the activation times of the generated *events* accordingly, distributing the activation *events* within the time interval ending with the next PID action.

5.2 Experimental data set

In order to attempt at a validation, or at least evaluation, of the unsteady numerical model, a data pool representing the transient behavior of the system is needed. As explained in Chapter 4, the model was calibrated thanks to the availability of large database containing information on the longitudinal velocity in the tunnel. Such data were recorded along with the boundary conditions and ventilation settings that produced it, and sampled with an optimal spatial resolution. Unfortunately, the approach employed for the measurement is only capable of recording field data in steady-state conditions. The whole idea of displacing a stationary survey rake through the road tunnel can not be applied in unsteady scenarios, either in its classic (moving a stationary survey rake to different locations, e.g. [78]) of modern (continuous displacement, high sampling rate, e.g. [14]) conception.

A proper measurement campaign, aimed at recording the longitudinal velocity profile at multiple instants during an emergency management simulation, would require resources that are not affordable in practice. The local average velocity would need to be evaluated, strictly simultaneously, by measurement stations set at multiple locations. Imagining each measurement station as composed by a rake supporting five anemometers (the measurement facility employed in [78]), and considering the number of measurement locations

required in order to have a sufficient profile resolution on the whole 11610 m, it is easy to figure out that such an experiment would require an unattainable economic effort. Moreover, the setup of the measurement facility would be rather difficult and require long dedicated road closures.

Therefore, to the extent of the present study, the numerical model has been compared with measurements taken from the *Mont Blanc* tunnel database, collected during real or simulated emergency events by the embedded measurement system. The calculated velocity profile is compared to the local velocity values measured by the tunnel anemometers at 20 locations, with a frequency of 1 Hz. The velocity profile as calculated by the tunnel control system *SCADA* is also recorded in the database, and it is therefore added to the comparison to draw conclusions on the differences between the applications of the two prediction methods.

5.3 Applications

Two unsteady simulations were run on the basis of the boundary conditions and fan regimes as described within two different event records, contained in the TMB database. The first one is characterized by a huge pressure difference between the two portals, which doesn't allow the system to reach its desired condition of null velocity at the event location, despite the activation of all the available jet fans. The database record spans over 1340 seconds, over which the emergency ventilation setup is always enforced. The second record testifies an event that was better addressed: the pressure delta is much lower, and the null velocity condition at the event location is quickly reached thanks to the PID action. The record concerns 600 seconds and includes the deactivation of the emergency configuration: within the last minute the extraction fans are turned off and the extraction vents are closed.

The details concerning the activation and regime changes of the centrifugal fans are read from the event database: corresponding *events* and relative activation *ramps* (see Chapter 3 for details) are generated and assigned during the initialization of the unsteady simultation, in order to reproduce the event sequence that took place in the real system.

Although information about the PID output and jet fans activations is also present in the database, the control mechanism of the ventilation system has been fully simulated. Therefore, beside the obvious comparison of longitudinal velocity profiles at multiple instants, it is also interesting to compare the action of the actual PID controller – embedded in the TMB tunnel – with that of its digital twin, which is characterized by the same coefficients but bases its error evaluation only on the calculated velocity field.

The simulations were run with a time step of 0.5 seconds. Some preliminary simulations, concerning limited time intervals, were run employing smaller time step values such as 0.1 s and 0.2 s: the differences between the obtained velocity profiles were too small to justify lengthier calculations. For similar reasons a relatively loose tolerance criterium has been established for evaluating the convergence of the internal cycle: the iterations stop as soon as the maximum absolute value of pressure correction applied is lower than 0.1 Pa.

5.4 Results

The comparison between the tunnel velocity profile as calculated by the numerical model and the measured data supplied by the TMB database is brought forward in Figures 5.1

and 5.2.

In general, the velocity profile resulting from the numerical model (green line) shows satisfactory consistency with the local velocity data as registered by the anemometers (red squares).

During Test 1, the pressure delta between the tunnel ends (as recorded in the TMB data base) undergoes a significant variation: the pressure delta, during the last part of the transient scenario, is around 60 Pa smaller with respect to the first measurement. On the other hand, the whole transient simulation is run leaving unchanged the pressure boundary conditions which are set at the beginning of the simulation, since a tool for the treatment of time dependent boundary conditions has not been implemented yet. The slight offset which can be noticed in Test 1, especially towards the last frames (Figure 5.1 (g) (h)), may be due to such pressure variation, which is not accounted for by the numerical model.

The model result (green line) and the velocity profile as predicted by the TMB control system SCADA (dotted gray line) have very different shapes for the most part of both tests. This is due to one of the main assumptions on which the SCADA software bases its prediction method (see Chapter 2 for details): all the exhaust air flow rate measured at the extraction fans is considered as coming strictly from the tunnel stretch in which the extraction vents are open. The air leakage through closed extraction vents is therefore neglected from SCADA.

On the other hand, the present 1D model considers the aforementioned leakage, directed from the main tunnel to the depressurized extraction channel: this partially compensates the fresh air intake, leading to a less steep longitudinal velocity profile whenever the extraction fans are active. The leakage also cause the extracted flow rate in the vicinity of the event (responsible of the abrupt "gap" in the velocity profile plot) to be lower in the numerical model, hence leading to a smaller gap.

In most cases, the local velocities recorded by the anemometers suggest a shape and a "gap" magnitude which are closer to the model results than to the profile predicted from the SCADA.

Figure 5.3 shows a comparison between the PID action as predicted by the numerical model (blue) and the recorded data concerning the behavior of the PID control embedded in the system (red). The dotted lines represent the number of active jet fans requested by the PID at a certain time (updated every 10 seconds), while the solid lines represent the actual number of active jet fans.

Despite not being completely overlapped, the plotted signals show an encouraging agreement. In Test 1 (Figure 5.3(a)), both PIDs quickly turn on all the available jet fan couples, which are 31 (3 were excluded because of being located within the tunnel stretch with open extraction vents, while 4 more were under maintainance at the time). In Test 2 (Figure 5.3(b)), both PID controls turn on 10 fan couples and then start deactivating them gradually. The difference between the signals which is evident after time step 500 is due to the fact that the PID embedded in the TMB is turned off once the emergency is successfully managed, and the jet fan couples count is therefore set to 0. The possibility of abruptly turning the PID off has not been implemented yet in the numerical model.

A constraint on the fan activations number within a limited time was set in the PID model to simulate the impossibility, for electrical reasons, to activate large batches of jet fans at the same time which delays the action of the PID control embedded in the TMB. Nonetheless, such criterion (10 fan activations every 10 seconds) should be revised as the requests of the simulated PID are actually quicker in all cases.

All in all, despite the limited extent of this preliminary validation of the model on transient scenarios, the results are considered as satisfactory.

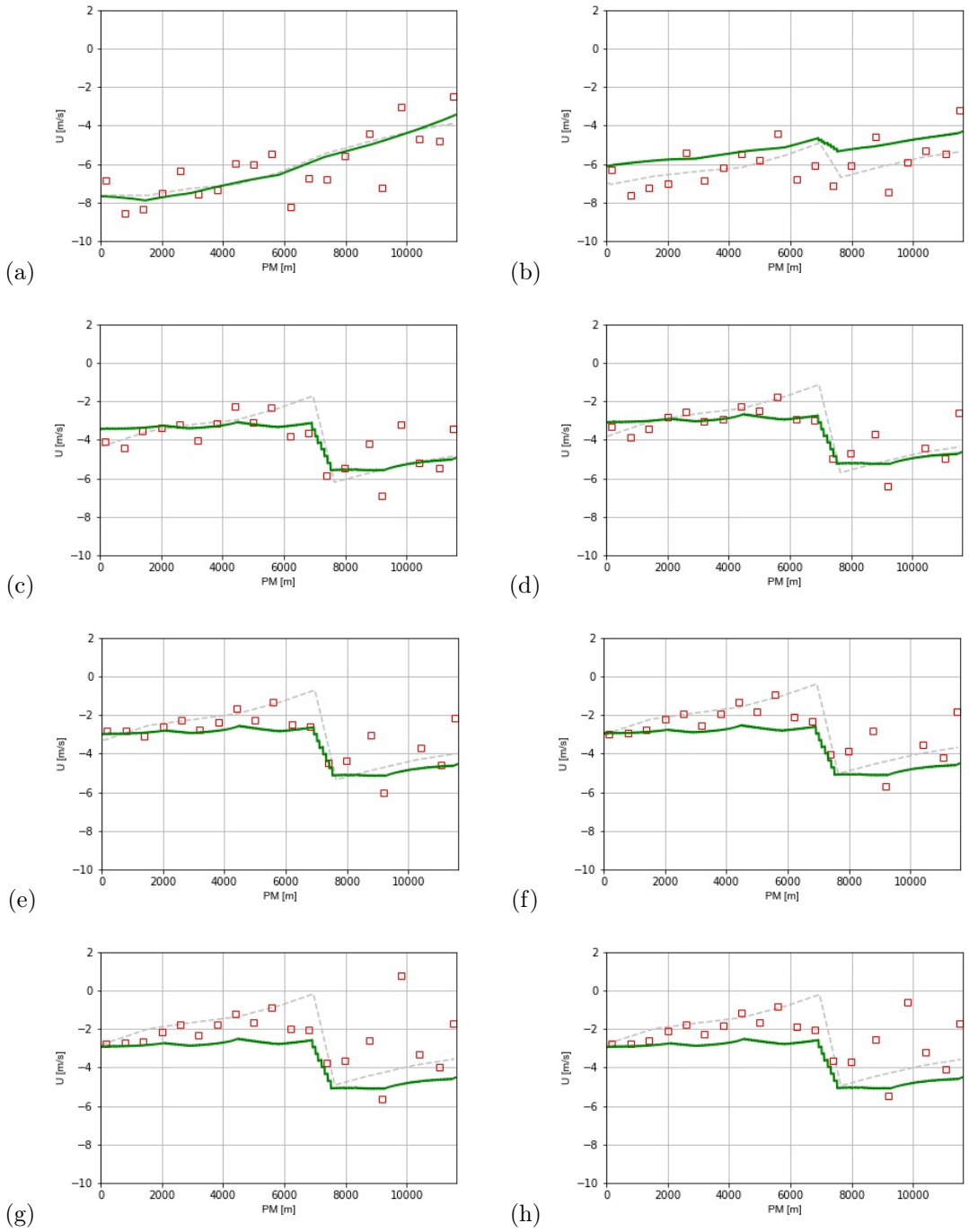

Figure 5.1: Validation of the unsteady solver results against experimental data recorded from the emergency system test performed on 2018-03-01, with initial $\Delta p = -850.59$ Pa. Green line: calculated velocity profile. Gray dotted line: velocity profile as calculated by the tunnel control system (SCADA). Red squares: local velocity as measured by fixed anemometers. The frames concern different instants, identified by their distance in seconds from the simulation start time 03:37:00. (a) 0 s (b) 100 s (c) 200 s (d) 300 s (e) 400 s (f) 500 s (g) 900 s (h) 1300 s

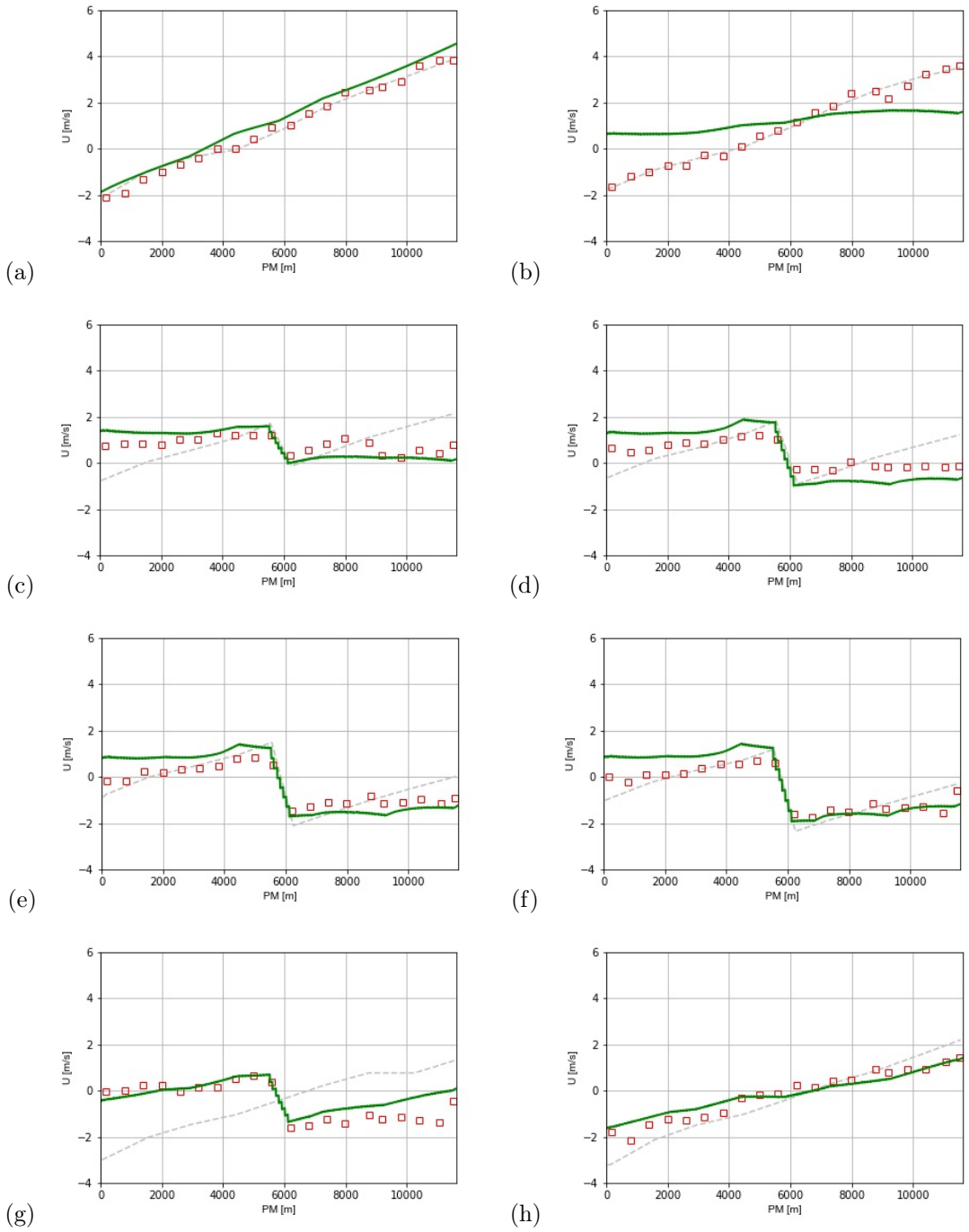

Figure 5.2: Validation of the unsteady solver results against experimental data recorded from the emergency system test performed on 2019-04-09, with initial $\Delta p = 117.21$ Pa. Green line: calculated velocity profile. Gray dotted line: velocity profile as calculated by the tunnel control system (SCADA). Red squares: local velocity as measured by fixed anemometers. The frames concern different instants, identified by their distance in seconds from the simulation start time 05:40:45. (a) 0 s (b) 100 s (c) 150 s (d) 200 s (e) 300 s (f) 500 s (g) 540 s (h) 580 s

(a)

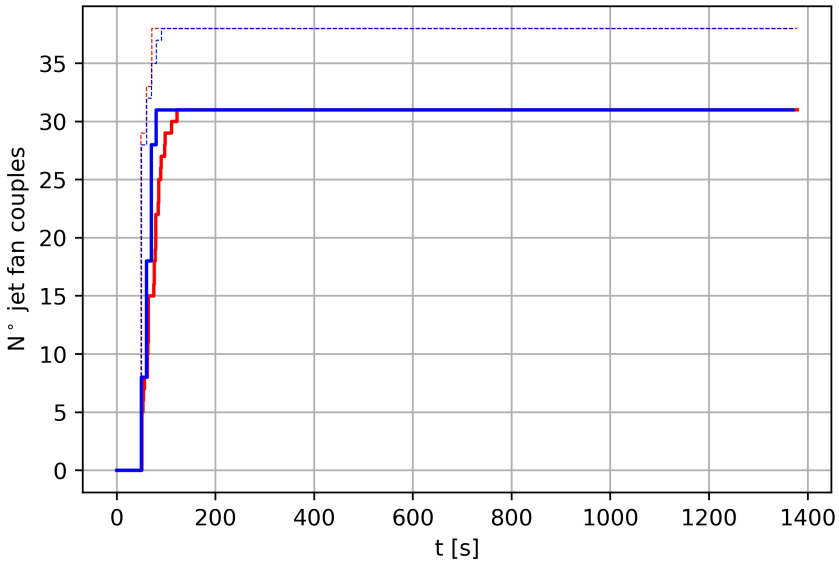

(b)

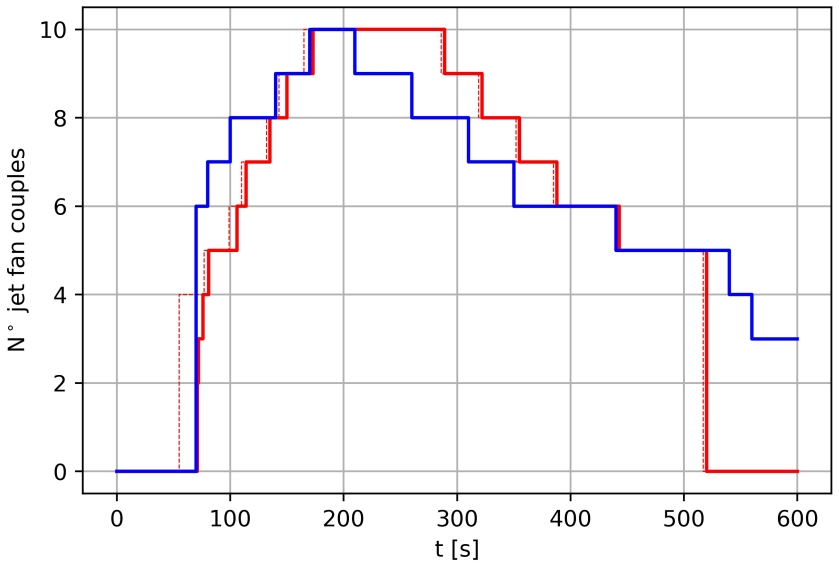

Figure 5.3: Comparison of the modeled PID action (blue lines) and the recorded data concerning the behavior of the PID control embedded in the system. Dotted line: number of active jet fan couples, as requested by the PID control. Full line: effective number of active jet fan couples in the TMB tunnel. The frames concern two different events: (a) 2018-03-01 03:37:00, $\Delta p = -850.59$ Pa (b) 2019-04-09 05:40:45, $\Delta p = 117.21$ Pa

Chapter 6

Experimental verification of smoke confinement

6.1 Introduction

Within all the previous part of this work, the criterion which was employed for attesting the success of an emergency event management was completely based on the profile of the longitudinal velocity along the main tunnel. As explained in section 2.4.3, the aim of the extraction system is to obtain a null longitudinal velocity value at the emergency location.

In such emergency conditions, the extraction system operates at full power and, thus, an abundant airflow leaves the tunnel at the event location. Therefore it is intuitive to guess that, if longitudinal velocity is null at the event point, it means that the longitudinal air flows in both the adjacent tunnel strethces are directed towards the event.

This condition has always been regarded as satisfactory from the very early stages of the design and development of the ventilation system controller of the *Mont Blanc* tunnel, and is commonly adopted for this kind of problems. The recurrent emergency simulations that take place in the tunnel give the empirical proof of the validity of this approach.

Nonetheless, in order to better understand the limits (or margins) of this assumption, an experiment in a scaled tunnel has been set up in collaboration with the Laboratoire de Mécanique des Fluides et d'Acoustique (LMFA). The experimental facility is located at the Ecole Cetrale de Lyon (France), and it was created by Salizzoni *et al.* and employed for a number of studies through the last decade [28, 29, 30, 31]. The experimental model, as it will be further explained at next section, does not present a full similarity with the *Mont Blanc* tunnel in terms of cross section. Nonetheless, it also sports a transverse ventilation system, and – within certain limits – it is possible to simulate the presence of a natural pressure gradient within the tunnel.

Therefore, the experiment presented through this chapter is meant to shed more light on the local behavior of a buoyant smoke plume.

The experiment is qualitative, as the smoke distribution – made visible by the seeding of a tracer in the buoyant flow which represents the smoke plume – is evaluated by the operators: the discerning of a "containment" condition is left to human decision. The experiment also allows to investigate about the stratification (or destratification) of the buoyant flow, and to define in which conditions – for example – it is not possible to contain the smoke without causing its destratification.

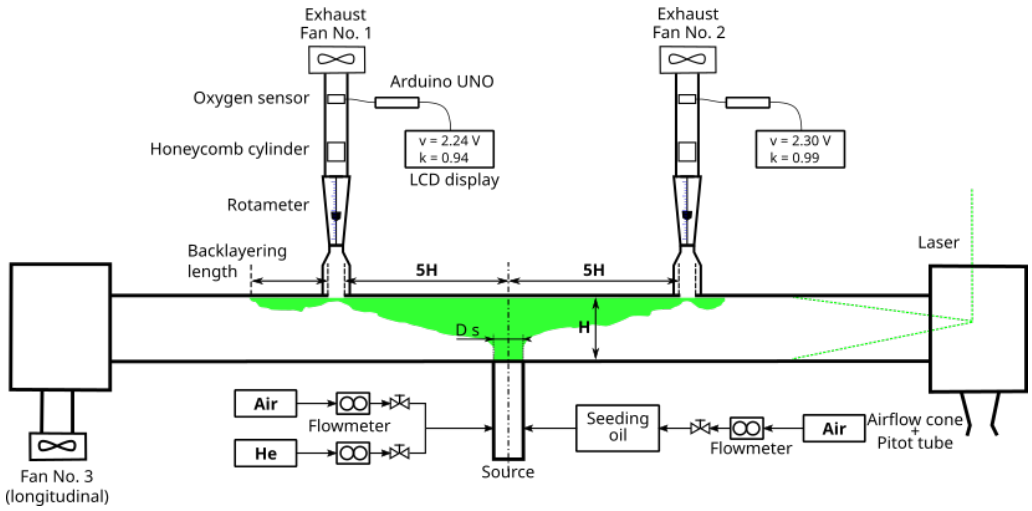

Figure 6.1: Schematic of the experimental facility.

6.2 Experimental facility description

The experimental facility, a 1/25 reduced scale model of a road tunnel (which resembles to the Frejus tunnel for its rectangular cross section), has been developed by Laboratoire de Mecanique des Fluides et Acoustique (LMFA), Ecole Centrale de Lyon.

A schematic view of the full experimental setup is presented in Figure 6.1. It includes:

- the main body, which is a 8.4 m long tunnel model with a rectangular cross section of width 0.36 m and height 0.18 m. In order to allow for flow visualization, one of the lateral walls of the tunnel is made of transparent toughened glass. The floor, ceiling and the remaining lateral walls are made of plywood and painted black;
- two extraction vents on the tunnel ceiling, which are equipped with a flow rate measurement system. The vents are connected to the inlet section of a centrifugal fan by means of a flexible circular pipe;
- an additional centrifugal fan which is connected to one of the tunnel ends, and is in charge of creating a longitudinal pressure gradient;
- an airflow cone equipped with a Pitot tube, connected to the remaining end of the tunnel, in charge of the measurement of the flow rate entering the tunnel;
- a laser beam which is projected to illuminate the longitudinal symmetry plane of the tunnel, by means of lenses located in correspondence of the tunnel inlet;
- a circular source which is located on the tunnel floor, and it is connected to a system in charge of mixing and seeding a controlled buoyant flow.

Fire-induced smoke is modeled by releasing a mixture of air and helium seeded with oil drops, into ambient air. The resulting buoyant flow is illuminated by a laser plane, and is visible thanks to the suspended oil.

The system which provides the buoyant flow is composed by three flow meters that allow to control the proportions of the buoyant mixture. The most part of the flow is

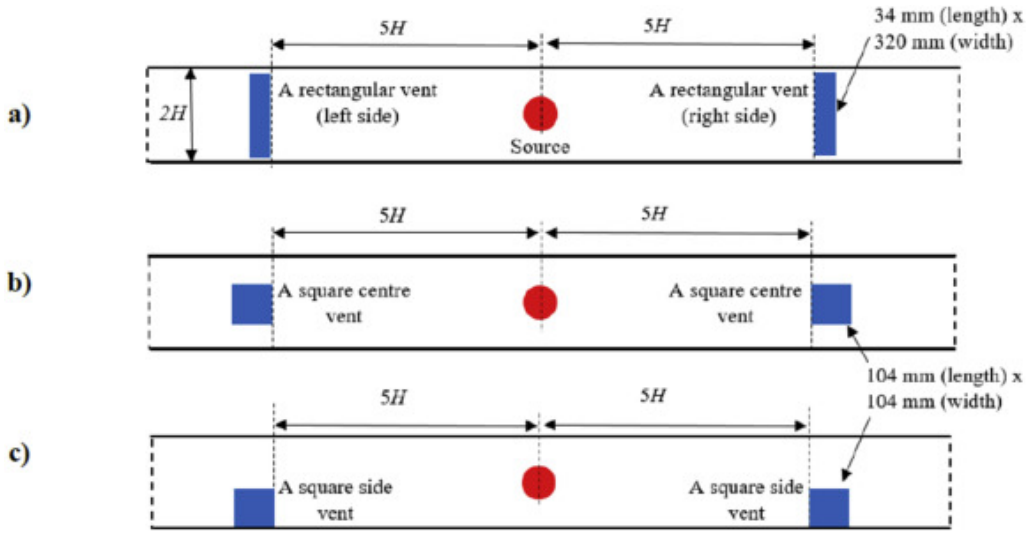

Figure 6.2: Different extraction vents shapes. (from [31])

delivered by just two of these devices, which are capable of providing up to 200 and 500 l/min. They control the helium and air flow, respectively. The flows converge and mix in a long pipe, and are subsequently joined by an additional air flow before being injected in the plenum. Such flow is delivered from a smaller flow meter (20 l/min) through a bubbling oil tank, where it is seeded with nebulised oil; the resulting mixture is then added to the main flow. The mixture is then injected in the plenum at floor level through a central, circular shaped source of diameter 0.1 m.

Two extraction vents are placed on the ceiling, one on each side of the source. The distance between each vent and the source is 5H, where H is the height of the tunnel.

A flow meter directly follows each vent, based on a rotameter (variable area flow meter) with a range from 16 to 160 m^3/h. The position of the cursor of this latter on a linear scale indicates the volumetric flow rate passing through the rotameter, assuming that the fluid is air. However, the buoyant flow which the extraction system is meant to capture is lighter than air; therefore the flow rate value, as read on the instrument linear scale, needs to be corrected according to the actual density of the processed fluid. To this aim, a calibrated oxygen sensor is integrated downwind with respect to each rotameter. With the measurement of the concentration of oxygen within the exhaust smoke flow, it is possible to evaluate the ratio between air and helium in the mixture, therefore to calculate its real density. A honeycomb cylinder is placed before the oxygen sensor to protect it from oil particles that could stick to the sensor surface compromising its efficiency in the long run.

The part of the tunnel ceiling which hosts the vent is designed to be easily replaceable, so that the vent shape and extension is adjustable. The opening is followed by a nozzle which ensures a uniform flow velocity at the rotameter entrance, so as to avoid fluctuations of the floating cursor.

The extraction flow is ensued by centrifugal fans, one for each vent. The rotation speed of both fans is adjustable by means of a potentiometer wired to each of them. Each fan is capable of extracting an air flow in the range 5 150 m^3/h. A similar fan is employed for the longitudinal flow.

Three different damper shapes were employed through the experiment, all sharing the

same cross section of approximately 0.011 m ^{2} . Refering to figure Figure 6.2, the employed shapes are:

- a transverse rectangular shape, of size 0.32 m × 0.034 m, that will be referred to as "RSD" (a);
- a centered square damper, of size 0.104 m × 0.104 m, referred to as "SSD-PC"(b);
- an off-centered square damper, which has the same shape of the previous one but is located on one side of the tunnel, creating a longitudinal asymmetry, referred to as "SSD-PS" (c).

The last component that has been employed during the experiment is constituted by two planar barriers, to be hung at the ceiling in the proximity of the vent in order to enhance the vent capture efficiency. Their height is H/3 and their width is equal to the width of the tunnel (therefore 2H). The barriers are sufficiently rigid to withstand the aerodynamic forces developed by the tunnel flow.

6.2.1 Rotameter correction

As previously mentioned a rotameter is a form of variable area flow meter consisting of a tapered tube, which has to be set in vertical position, hosting a floating cursor.

In order for the gas flow to pass through the rotameter, it must first raise the float held within. Considering any buoyancy effect as negligible (as the density of the float is too high with respect to the density of the gas passing through the device), when the flow goes through the device, the forces acting on the cursor are mainly:

- pressure force, due to differential pressure across the cursor, directed upwards;
- gravity force, directed downwards.

As the cursor moves up through the tube – because of the tapered nature of the tube – the annular opening separating the two increases. As this increases the differential pressure across the float decreases, thus decreasing the upward force. The floating cursor stabilises when its weight is in equilibrium with the upward force being exerted by the fluid or gas. Assumuing the fluid density as fixed, the height of the cursor is linearly dependent on the flow rate through the device. Therefore, a calibrated scale is printed onto the tube itself, giving a volumetric flow reading (in litres per minute), which is valid for air at standard temperature and density.

Since the fluid that flows through the rotameters in the present case is a mixture of air and helium, the flow rate value as read on the devices go through a correction in order to take into account the different fluid density. The rotameter had already been calibrated in [31]: values of the corrective coefficient β are known for a number different density ratios ρ/ρ_0, ranging from 0.5 to 1.0 (see Figure 6.3).

As a definition of the function $\beta(\rho/\rho_0)$, a piecewise linear function connecting the known points is chosen.

It is therefore possible to write:

$$q_i = \beta(\rho/\rho_0)q_r \tag{6.2.1}$$

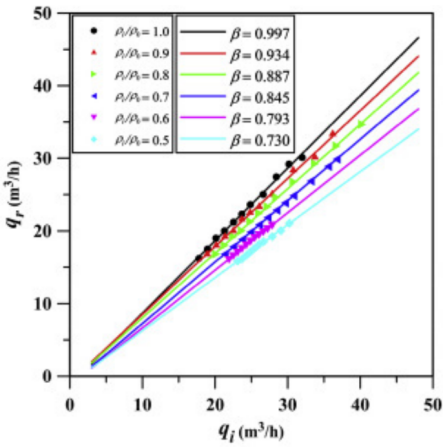

Figure 6.3: Calibration of the rotameter (from [31])

where q_i is the effective flow rate value and q_r is the value as read on the device. β is a known function of ρ/ρ_0, valid in the range $\rho/\rho_0 \in [0.5, 1]$.

To measure ρ/ρ_0, an electrochemical oxygen sensor has been added downstream of each rotameter. The density ratio of the gas mixture can be therefore estimated as a function of the voltage output of the oxygen sensor. The voltage value is acquired by an Arduino UNO board, which converts it to a value of ρ/ρ_0, and displays the corresponding correction factor β on a digital screen (Grove - LCD RGB Backlight). The condition $\rho/\rho_0 \in [0.5, 1]$ is also checked within the Arduino board, and the digital screen backlight is set to red color if the density ratio falls outside the validity range.

In order to investigate the relationship between the voltage output of the sensor and the density ratio, a calibration process was carried out, by feeding the sensor a flow which is known in terms of density.

For this process, two flowmeters are connected to a mixing pipe section, and the sensor is mounted at the end of the pipe. By controlling the flow rates of air and helium that are injected in the system, the sensor is tested for density ratio values ranging from 0.5 to 1. The corresponding voltages are recorded, defining known couples of voltage and density ratios.

Two polynomials are therefore defined to interpolate the points provided by the tests on the two sensors (as their responses are similar, but do have slight offset), and loaded to the corresponding Arduino boards.

The actual flow rates can therefore be quickly evinced by reading the value on the rotameter, then multiplying it for the corrective coefficient shown in real time on the corresponding LCD display.

6.3 Governing parameters and flow conditions

There are many adjustments, which directly influence the tunnel flow, that can be made thanks to the design of the experimental facility:

- the buoyant jet density can be adjusted by changing the ratio between helium and air components;

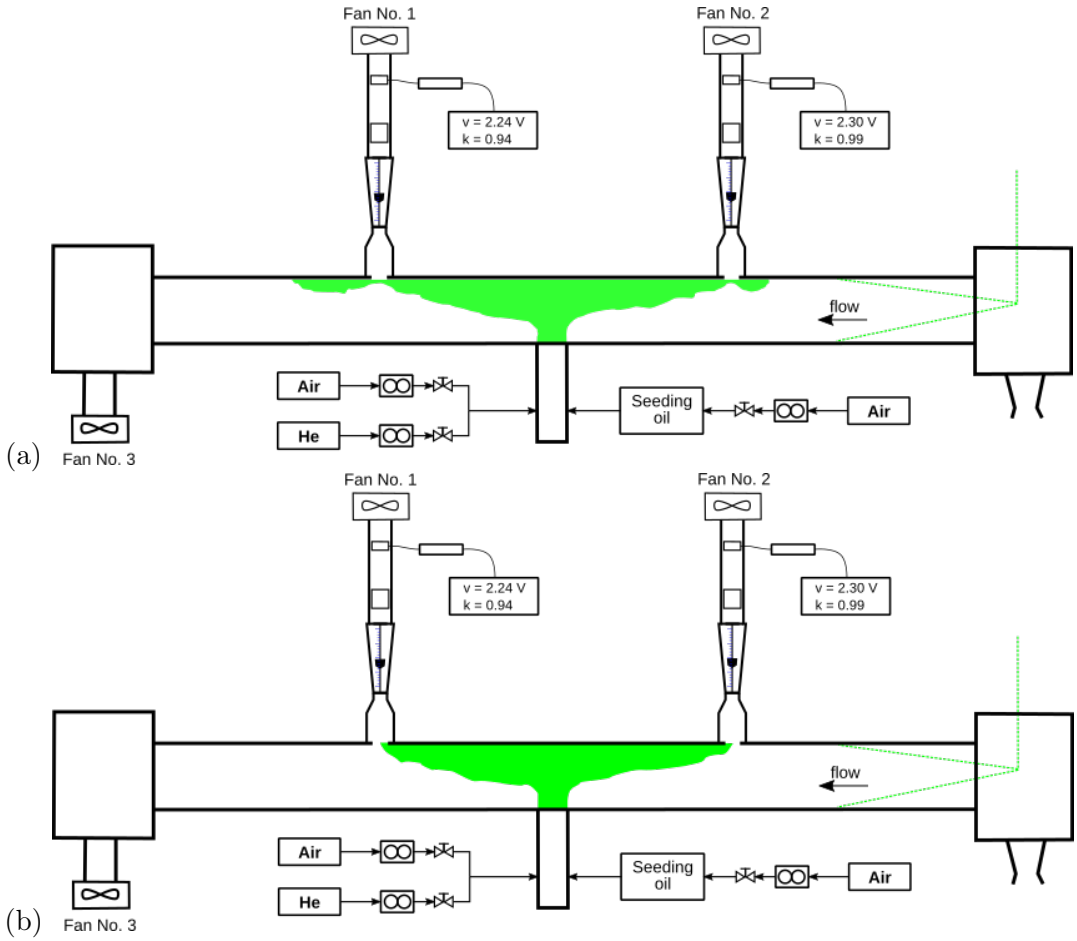

Figure 6.4: Different flow regimes: smoke distribution in absence (a), and in presence (b) of the confinement condition.

- the buoyant jet initial velocity can be adjusted by changing the total flow rate of the source;
- the three fans regimes can be adjusted by changing the frequencies of their electrical input;
- the shape of the exhaust vents can be changed;
- solid vertical barriers can be included or excluded.

As it will be further explained within the next section, a set of controlling parameters – capable of fully identifying the experimental facility configuration – can be defined.

The aim of this experiment is to allow for the evaluation of configurations, which can be expressed as sets of the controlling parameters. Each configuration can lead to what will be called *confinement* condition, or not. Any configuration which allows the buoyant flow to surpass the extraction vents (as in Figure 6.4 (a)) is defined as not confined. On the other hand, if the buoyant flow remains confined between the two extraction vents, the configuration is defined as confined (Figure 6.4 (b)).

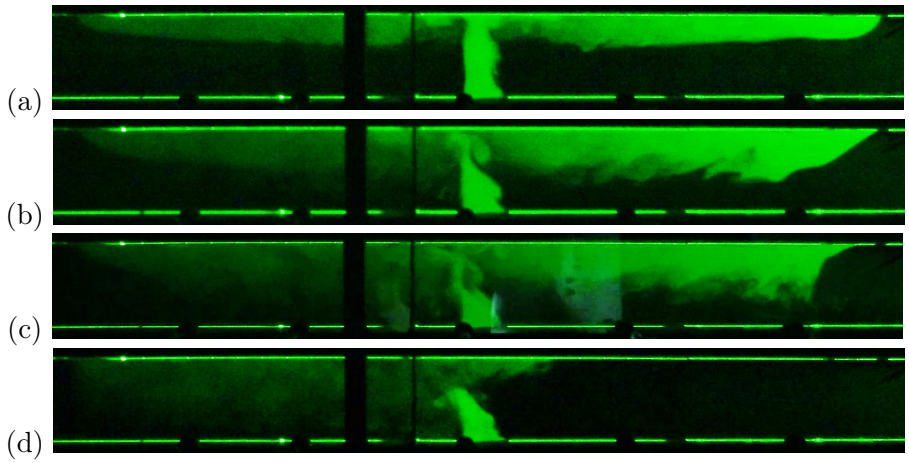

Figure 6.5: Examples of stratification patterns of the smoke in the tunnel.

One further classification can be performed over the possible configurations, based on the criteria of stratification:

- the flow can be stratified, meaning that buoyancy prevails over turbulent mixing, therefore the smoke is still clearly separated from the air and close to the tunnel ceiling (Figure 6.5 (a));
- the flow can be destratified, meaning that turbulent mixing prevails over buoyancy, therefore the smoke mixes with the tunnel air and it is present all over the tunnel section (Figure 6.5 (c)).

Since the configurations that are going to be analyzed are not symmetrical with respect to the buoyant sources, mixed configurations are also expected:

- the flow can be stratified at one side of the source, and destratified on the other (Figure 6.5 (b));
- for configurations with strong longitudinal component, the smoke can be present only on the downwind side of the source (Figure 6.5 (d)).

6.4 Dimensional analysis

As previously mentioned, the fire source within the tunnel is modelled by means of the injection of a mixture of helium and air. As shown by Jiang *et al.*. [85] in experiments with longitudinally ventilated tunnel, these densimetric plumes reliably reproduce the buoyant behaviour of hot combustion products. On the other hand any dynamic and thermal effect induced by conductive or radiative heat transfer (e.g. with tunnel walls) are intrinsically ignored.

Considering an infinitely long tunnel with fixed cross section, it has been asserted that the smoke back-layer length depends on the source charachteristics, on the induced longitudinal velocity [86] and on the vents charachteristics. Since in our case the longitudinal

velocity is due to both the extracted flow rate (induced) and the presence of a fan which depressurizes one end of the tunnel, both longitudinal velocity and velocity at the extraction vents (which will be kept equal for the two extraction vents all along the experiment) need to be included among the governing parameters.

Adopting basic dimensional arguments [85] and assuming negligible diffusive effects, the dimensionless length of the smoke back-layer can expressed as:

$$\frac{L}{H} = f\left(\Gamma, \frac{\rho_s}{\rho_0}, \frac{D_s}{H}, \frac{A_D}{H^2}, S_D, P_D, \frac{u_t}{u_s}, \frac{u_e}{u_s}\right) \tag{6.4.1}$$

Γ is the *plume Richardson number*, defined as:

$$\Gamma_s = \frac{5}{16\alpha}\frac{(\rho_0 - \rho_s)g}{\rho_0}\frac{D_s}{u_s^2} \tag{6.4.2}$$

where $\alpha = 0.12$ is a reference value for the "top-hat" entrainment coefficient [87].

All the variables referred to with the subscript S refer to quantities measured at the source, while the subscript 0 refers to measurements at the tunnel entrance. Subscript D refers to the dampers: S_D and P_D represent shape and and position of the dampers respectively.

The buoyancy flux at the source is defined as:

$$B_s = g u_s A_s \frac{\rho_0 - \rho_s}{\rho_0} \tag{6.4.3}$$

with g being the gravitational acceleration.

Given that the extraction fans are adjusted so that the volumetric flow rates at the exhaust air vents are equal, we can define *confining velocity* as the minimum velocity at the extraction vent that guarantees the confinement of the smoke. On the base of this definition, by imposing a null length of the smoke back-layer (equation (6.4.1)), a dimensionless form of confining velocity $u_{e,c}$ can be written as:

$$\frac{u_{e,c}}{u_s} = f\left(\Gamma, \frac{\rho_s}{\rho_0}, \frac{D_s}{H}, \frac{A_D}{H^2}, S_D, P_D, \frac{u_t}{u_s}\right) \tag{6.4.4}$$

Previous studies [88, 86] have shown that, considering highly buoyant releases, i.e. for $\Gamma_s > 1$, the relations expressed within equations (6.4.1) and (6.4.4) can be highly simplified. In these conditions the back-layering length and the confinement velocity do not show any clear dependence on a single source parameter. Nonetheless, these parameters do affect the flow as far as they induce variations in the source buoyancy flux B_s (equation (6.4.3)).

Therefore, for the scope of the present work, equation (6.4.1) can be reduced to:

$$\frac{L}{H} = f\left(\frac{A_D}{H^2}, S_D, P_D, \mathrm{Fr}_t, \mathrm{Fr}_e\right) \tag{6.4.5}$$

where dimensionless velocities are expressed by means of Froude numbers Fr, which express the ratios between the inertia forces induced by the ventilation flow and the buoyancy forces:

$$\mathrm{Fr} = \frac{u}{(H/B_s)^{1/3}} \tag{6.4.6}$$

Equation (6.4.4) can be, in turn, reduced to:

$$\mathrm{Fr}_{e,c} = f\left(\frac{A_D}{H^2}, S_D, P_D, \mathrm{Fr}_t\right) \tag{6.4.7}$$

Lastly, since the section area of the dampers openings is kept constant within the whole experiment, equation (6.4.7) can further reduced:

$$\mathrm{Fr}_{e,c} = f\left(S_D, P_D, \mathrm{Fr}_t\right) \tag{6.4.8}$$

The present study investigates the family of curves described by equation (6.4.8), with a focus on:

- proving the independence of the curves $\mathrm{Fr}_{e,c}\left(\mathrm{Fr}_t\right)$ from the sources parameters Γ_s and ρ_s/ρ_0;
- determining the dependence of the curves from dampers shape and position.

6.5 Experimental protocol

Let us first define the basic unit of the experiment as a *test*. A *test* is the procedure that allows, starting from a governing variables set (shape and position of the dampers, velocity and density at the source), for the evaluation of the relationship between the values of the *confining velocity* and the longitudinal velocity at the inlet.

A test starts by turning on all the fans at minimum regime. Once the longitudinal velocity at the tunnel inlet has reached stability, the flow meters which control the buoyant flow are also turned on: they are set so that the source charachteristics correspond to those defined by the governing parameters set.

Therefore, the buoyant plume is added but the extraction fans regimes are still so low that the smoke is not confined (Figure 6.4 (a)). The extraction fan regimes are slightly increased, then the balance of the volumetric flow rates at the dampers is checked. If needed, the extraction fans regimes are adjusted in order to balance the two flow rates.

This procedure is repeated until the smoke is contained in the tunnel stretch within the vents (Figure 6.4 (b)), and the velocities at the dampers are equal. Once this confining condition is reached, the velocity value at the dampers is recorded, along with the velocity value as measured at the tunnel inlet. This couple of measurements will constitute a point of the curve which describes the relation between the relation between the values of the *confining velocity* and the tunnel longitudinal velocity.

In order to define further points of the curve, the regime of the longitudinal fan is increased and the procedure is repeated. The exploration of each curve is stopped as soon as the flow rate at the extraction vents exceeds the rotameter measurement range.

Each time the confining condition is reached, the flow at the depressurized end of the tunnel (Q_a) is also determined by means of the continuity equation. Refering to figure 6.5, volumetric flow rates at the dampers Q_1 and Q_2 are measured, as well as the corresponding densities ρ_1 and ρ_2. As the velocity at the tunnel inlet is measured by the Pitot tube, and the inlet section area is known, Q_d is also known; the corresponding density is equal to that of environment air, ρ_0. Q_S is known as Γ_s and ρ_s/ρ_0, which are are fixed for each test, fully define that quantity.

Q_a can be therefore calculated:

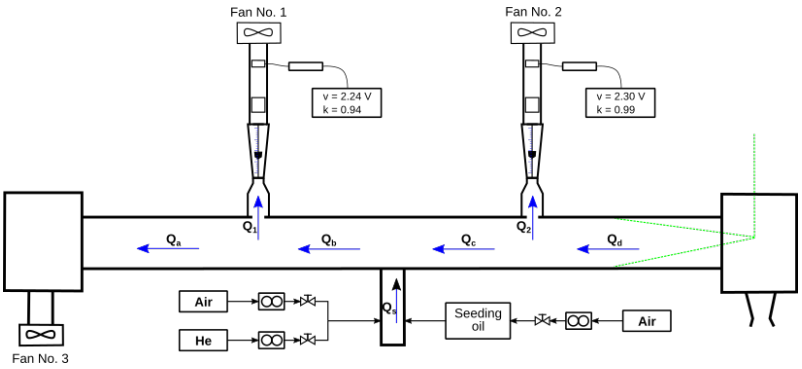

$$Q_a = \frac{1}{\rho_a}\left(\rho_0 Q_d - \rho_1 Q_1 - \rho_2 Q_2 + \rho_s Q_s\right) \tag{6.5.1}$$

Since this equation is applied in confining condition, we can consider the smoke as absent within the tunnel stretch marked by the subscript a. Thus, for $\rho_a = \rho_0$:

$$Q_a = Q_d + \frac{1}{\rho_0}\left(\rho_s Q_s - \rho_1 Q_1 - \rho_2 Q_2\right) \tag{6.5.2}$$

6.6 Design of experiments

The experimental campaign can be divided into two parts, aimed at the determination of the influence of different governing parameters on the confining velocity curves:

- the first part investigates the effect of the source characteristics;
- the second part investigates the effect of the dampers characteristics.

Concerning the first part, the first test was run with a plume Richardson number $\Gamma_s = 4$ and density ratio $\rho_s/\rho_0 = 0.7$. Two further tests have been run changing the value of plume Richardson number Γ_s to 8 and 16 respectively, while leaving the density ratio unvaried. Then, with a fixed value of plume Richardson number $\Gamma_s = 4$, two different density ratios were tested: $\rho_s/\rho_0 = 0.4$ and $\rho_s/\rho_0 = 0.2$.

During these five tests, which constitute the first part of the campaign, the rectangular shaped dampers were employed.

On the other hand, during the second part, plume Richardson number and density ratio have been fixed to $\Gamma_s = 4$ and $\rho_s/\rho_0 = 0.7$ respectively. The tree available dampers shapes were tested, both in absence and in presence of solid barriers of height $H/3$ attached to the tunnel ceiling.

6.7 Results

6.7.1 Influence of the source parameters

Figure 6.6 shows the results of the first part of the experimental campaign. The points which constitute the curves (which are differentiated by color) have been plotted in different

shapes, according to the stratification pattern shown by the smoke. A classification of those patterns can be found in section 6.3.

As it can be appreciated in Figure 6.6, changing source parameters within the selected range of $\Gamma \in [4, 16], \rho/\rho_0 \in [0.2, 0.7]$ does not change significantly the curve shape. All the points constituting the curves lay on the same straight line, suggesting a proportionality between confining extraction velocity and the velocity value as measured at the tunnel inlet.

The result from [31] has also been added to the plot and is in good agreement with the results of the present study. The main difference between [31] and the present study is the presence, in the latter, of a longitudinal fan: in fact, U_c and U_0 could not be considered a-priori as proportional in this case.

6.7.2 Influence of the dampers characteristics

Figure 6.7 shows the results of the second part of the experimental campaign. The colors and shapes of the points have been assigned similarly to the previous Figure 6.7.

The findings of [31] are reported with crosses, coloured based on the belonging curve. Due to the presence of the longitudinal fan, the confined condition is often found only at higher Fr-values in the present study. Nevertheless, the deviation between the confinement velocities should remain small, at least on the lowest point of the curve. Therefore, previous data show a good agreement only on the curves related to rectangular dampers.

However, the bigger deviations on the other curves are mostly due to the different criterion that was adopted in [31] for the evaluation of confinement condition: "We therefore consider that the confinement condition will be attained when $L/H = 0$ (i.e. total confinement) for the rectangular shaped dampers (RSD) and when $L/H = 1$ for the square shaped dampers (SSD)."

With respect to the changes of the source parameters, the shape and position of the damper have a signicant impact on the shape and extension of the curves.

The most extreme example is the off-centered square damper: the smoke confinement was only possible at very high velocity values, way above the value causing the smoke to destratify. On the other hand, agreeing with previous findings, the rectangular shaped damper leads to the best performance.

Vertical barriers in proximity of the dampers have been found helpful, especially on the square shaped dumpers. Their action is less evident on rectangular shaped dampers, as their opening already covers the whole width of the tunnel. It is interesting how the presence of a vertical barrier leads to a curve which resembles to the one of a better performing shape: the off-centered square, with vertical barriers, presents a curve which resembles to the one registered for the centered square. The centered square, in turn, behaves as if it was rectangular thanks to the vertical barrier.

6.7.3 Flow rate at the depressurized end

The velocity in correspondence of the depressurized end of the tunnel (the one which is under the most direct influence of the longitudinal fan) has been calculated for all the tests. The resulting flow rates, divided for the total extracted flow rate, are reported in Figures 6.8 and 6.9. It is immediate to notice that in all cases, such flow rate is negative: this means that the flux is directed towards the center of the tunnel – the opposite with respect to the flow that would be induced by the longitudinal fan alone.

This is due to the relatively high extraction fan regimes which are required for confining the smoke despite the action of a longitudinal fan, even if this latter works at very low regimes.

It is therefore evident that the two flows at the external sides of the dampers (Q_a and Q_d) must be directed towards the smoke source (thus be opposite in sign) in order to guarantee confinement condition. This confirms the assumption taken during the design of TMB ventilation system: the point with null average flow rate (and velocity) must be located in the close proximity of the smoke release for the system to work properly.

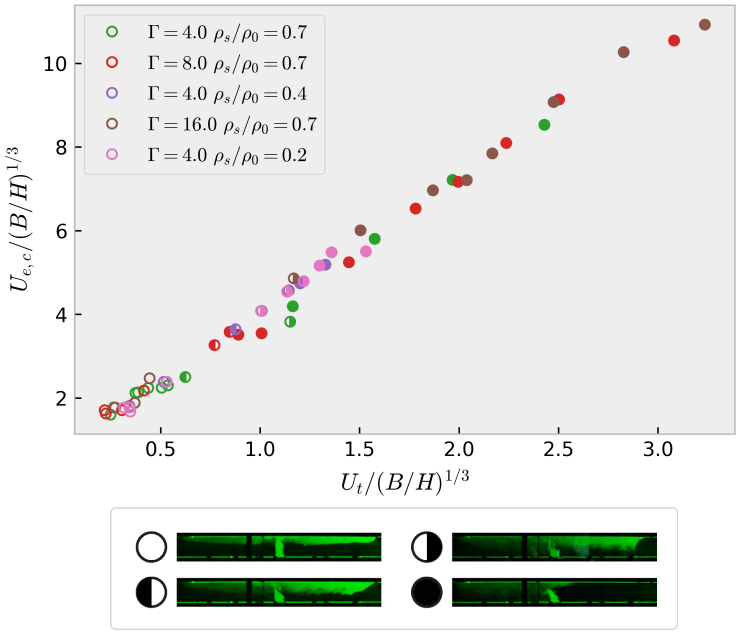

Figure 6.6: Confinement velocity curves as a function of longitudinal tunnel velocity, for different couples of source parameters.

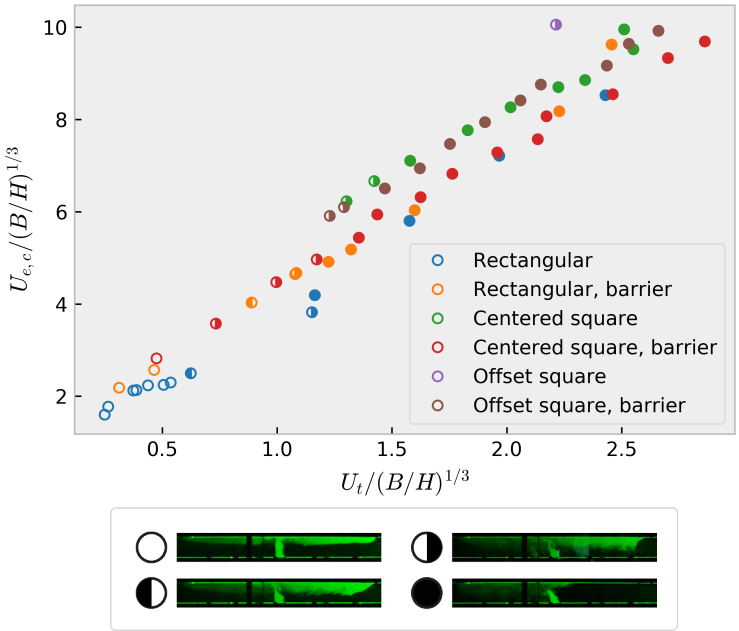

Figure 6.7: Confinement velocity as a function of longitudinal tunnel velocity, for different dampers configurations.

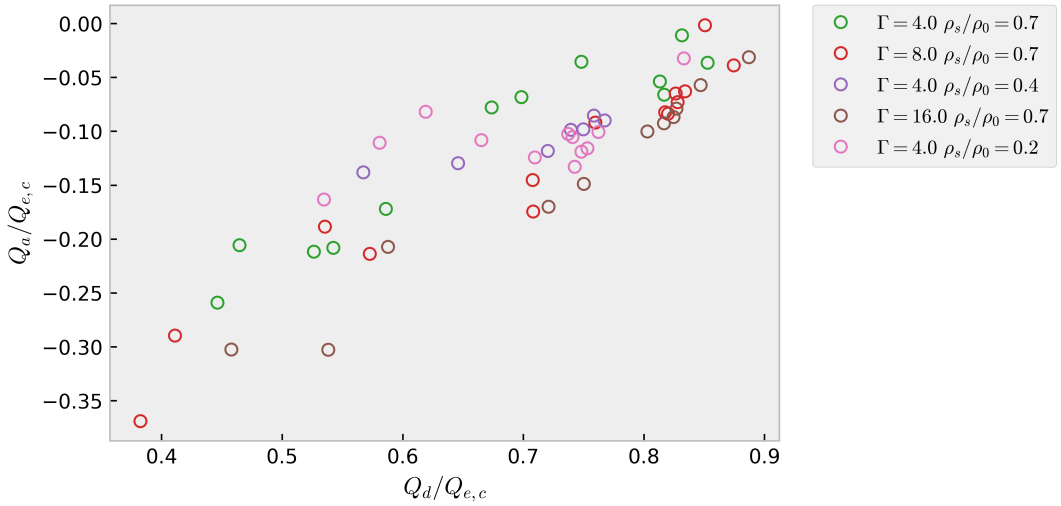

Figure 6.8: Flow rate at the depressurized end, for different couples of source parameters.

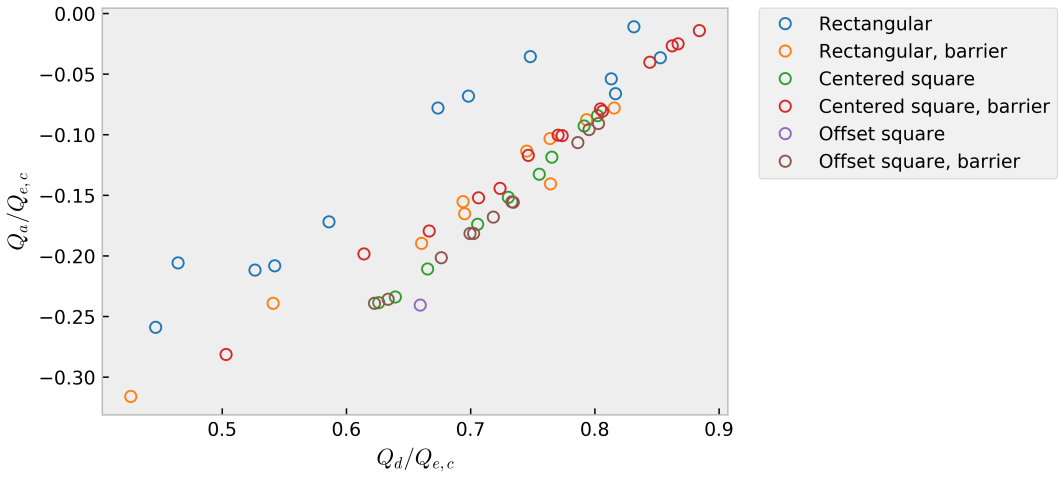

Figure 6.9: Flow rate at the depressurized, for different dampers configurations.

Chapter 7

Conclusions

In the present work, a numerical procedure for the calculation of airflow in a road tunnel ventilation system was presented and applied to the case of the *Mont Blanc* tunnel. The method is based on a Finite Volume discretization of mass, momentum and thermal energy conservation equations, under the hypothesis of 1D, steady-state flow. The topology of the network of ducts that constitute the ventilation system is represented by means of an oriented graph. A mathematical model was outlined starting from equations expressing the balance of mass, momentum and energy in the system. Assumptions has been discussed and adopted in order to simplify the governing equations. Then, the equations have been discretized and re-written in matrix form.

The numerical resolution of the discretized equations was based on a modified version of the SIMPLE algorithm. The method was described in detail, highlighting the peculiar strategies adopted to treat source and sink terms, and variable transfer from nodes to branches of the network and vice-versa.

The programming language of choice for the implementation of the whole procedure has been Python. As it fully supports object-oriented programming, it constitutes the ideal support for the representation of sources through nested models (as described in Section 3.9) as well as the management of *events* and *ramps* in transient simulations (as described in Section 3.10).

Successively, a model network of the *Mont Blanc* tunnel ventilation system was constructed, representing the tunnel itself and its fresh air intake and exhaust air extraction channels. The spatial resolution of the part representing the main tunnel is as small as 10m. In the rest of the network, in absence of particular needs i.e. presence of a centrifugal fan or the frequent connections with the main tunnel (for the distribution stretch of fresh air ducts), a coarser partition has been constructed with maximum branch length within 100m.

A set of 13 parameters representing friction losses within the various parts of the system was defined; parameter values were then calibrated against an experimental benchmark dataset of longitudinal velocity profiles, measured along the tunnel by means of a custom-made survey rake during five in situ tests performed at the *Mont Blanc* tunnel.

Calibration of the parameter set was performed by mean of genetic optimization algorithm, namely DES (Derandomized Evolution Strategy). With the optimized parameter values, a good agreement between the predicted velocity profiles and the experimental data was found, with an overall RMS deviation of ± 0.27 m/s, lower than the measurement accuracy of the probes used for the experimental campaign. Given the complexity

of the model, and the relatively low number of loss coefficients chosen for calibration, the obtained accuracy has to be regarded as highly satisfactory.

The calibrated model has then been employed to provide further validation against a selection of field velocity data recorded by the tunnel monitoring and control system under extremely diverse environmental boundary conditions. Such data set, despite being less rich and accurate than the continuous airflow acquisition measurements carried out for the calibration, represents nevertheless a good benchmark, since it is indeed completely independent from the calibration data.

The calibrated model instance has been also employed for validating the model in transient conditions. Two transient simulations were set up to emulate the time dependent tunnel velocity profiles during two emergency events that were recorded in the *Mont Blanc* tunnel by the embedded control system. A sub-model was outlined and implemented in order to simulate the action of the PID control, which manages the activation and deactivation of the axial jet fans in the TMB tunnel. The simulated transient scenarios showed an encouraging consistency with the recorded data. A few improvements, that could enhance the reliability of the model in transient conditions, were pointed out.

In the last part of the present work, an assumption that has been the basis for every evaluation of emergency management in the TMB tunnel (i.e. to consider the smoke as successfully confined in case of null longitudinal velocity value in correspondence of the emergency event location) has been discussed. Its validity has been investigated through a set of experiments on a scaled model of a road tunnel with transverse ventilation, capable of simulating the action of a pressure difference between the tunnel ends. A buoyant release of a mixture of air and helium was employed to simulate the release of hot smoke from a fire. The assumption has been qualitatively proven valid for a variety of different source parameters values, as well as for different extraction dampers shapes and locations.

Together with the experimental facility previously developed and described in detail in [14], the presented approach stands as a one-of-a-kind, robust methodology for analyzing, modeling and predicting airflow in road tunnel ventilation systems. The methodology could be applied with acceptable effort to any tunnel, and, with suitable adaptations of the experimental facility, also to different kinds of infrastructures that could be modeled as a network of ducts.

Despite its lower accuracy with respect to 3D full scale models, the present method is proven to be a convenient and lightweight computational tool, capable of reproducing different ventilation scenarios potentially occurring in the *Mont Blanc* tunnel with satisfactory accuracy, and applicable with relative ease to a large variety of similar systems.

List of Figures

2.1 Various representations of the *Mont Blanc* tunnel ventilation system: (a) sketch of the transverse cross-section of the tunnel and underground ventilation channels with locations of fresh air and exhaust vents and indication of the corresponding flow paths; (b) photograph showing the tunnel construction with an insight of the underground channels (c) sketch of the longitudinal section of the tunnel (top view) and planform of the underground ventilation channels (bottom view). 12
2.2 Details of the *Mont Blanc* tunnel ventilation system: (left to right) interior of the ventilation station on the Italian side; underground fresh air channel; fresh air supply vents along the sidewalk; a pair of jet fans. 13
2.3 Detail of the installation of sensors in the ventilation channels. 16
2.4 Example of successful smoke management, with null longitudinal velocity at the fire location. 17
2.5 Example of the action of a PID controller (from numerical simulation), represented by 6 subsequent frames. The plot on the left shows the tunnel longitudinal velocity profile (with a red vertical streak highlighting the fire location), while the plot on the right represents the PID action through a time frame of 300 s (with the vertical line indicating current time). 20

3.1 Example of basic graph: (a) a very simple network, (b) control volumes associated to the j-th branch (red) and *(i+1)*-th node (blue) of such network 26
3.2 Representation of the TMB tunnel graph: (a) a simplified overall view, (b) a detailed representation of a portion of (a). 27
3.3 Dimensional characteristic curves of the AF fans at different RPMs for $\rho = 1.07$ kg/m^3. 42
3.4 Dimensional characteristic curves of the AV and *relais* fans at $n = 1000$ rpm and for $\rho = 1.0$ kg/m^3. 43
3.5 Dimensionless characteristic curves of the AF, AV and *relais* fans. 44
3.6 Adapted fan curve (red), original curve (blue), mirrored curve(green) 45
3.7 Dimensional and dimensionless characteristic curve of a jet fan couple as installed in the *Mont Blanc* tunnel. 48
3.8 AV fans, 0-50% switch-on ramps: ensemble average and smoothstep function fit. 53
3.9 AV fans, 50-100% switch-on ramps: ensemble average and smoothstep function fit. 53
3.10 Relais fans switch-on ramps: ensemble average and smoothstep function fit. 54

3.11 Switch-off data for the AV fans and exponential fit. 54
3.12 Switch-off data for the *relais* fans and exponential fit. 55
3.13 Switch-on data for the jet fans and smoothstep fit. 55
3.14 Switch-off data for the jet fans and exponential fit. 56
3.15 Steady solver loop flow chart: source object internal values are updated based on the current state variable arrays. 59
3.16 Steady solver loop flow chart: one step of the guess-correct procedure is performed. Pressure and velocity fields are updated accordingly and the magnitude of the correction is evaluated and recorded, along with the iteration count. 60
3.17 Steady solver loop flow chart: the energy balance is solved, and the temperature field is updated accordingly. 61
3.18 Steady solver loop flow chart: a density array is evaluated basing on the newly calculated temperature field, and used for updating the density field. Then, the stop criteria are evaluated basing on the segregated algorithm output, and the cycle is either repeated or stopped. 62

4.1 3D mathematical model of the survey rake (from [78]) 68
4.2 (a) The vehicle in its final layout (b) The T.A.L.P.A. facility traveling through the *Mont Blanc* tunnel during the measurement campaign. tunnel during the measurement campaign. (from [14]) 68
4.3 Velocity profile as a function of the longitudinal tunnel coordinate (Metric Point, PM) reconstructed for test n. 1. An uncertainty strip for present measurement is added to the graph, as well as the estimated natural draught and the velocity values measured by the 20 ultrasonic anemometers of the TMB S.C.A.D.A. system. 70
4.4 Velocity profile as a function of the longitudinal tunnel coordinate (Metric Point, PM) reconstructed for test n. 2 (see also the caption to Fig. 4.3). The tunnel stretch where air extraction takes place is highlighted in the plot. . . 71
4.5 Velocity profile as a function of the longitudinal tunnel coordinate (Metric Point, PM) reconstructed for test n. 3 (see also the caption to Fig. 4.3). . . 72
4.6 Velocity profile as a function of the longitudinal tunnel coordinate (Metric Point, PM) reconstructed for test n. 4 (see also the caption to Figures 4.3 and 4.4). 73
4.7 Velocity profile as a function of the longitudinal tunnel coordinate (Metric Point, PM) reconstructed for test n. 5 (see also the caption to to Figures 4.3 and 4.4). Locations and direction of activated jet fans are also added to the plot. 74
4.8 Temperature profile as a function of the longitudinal tunnel coordinate (Metric Point, PM) recorded during the five T.A.L.P.A. runs. 75
4.9 Comparison between velocity profiles in Test 1: calculated with constant f model (blue), calculated with Swamee-Jain model (red), measured (black). Pointwise velocity measurements taken by the tunnel anemometers (green) are also plotted. 79

4.10 Comparison between velocity profiles in Test 2: calculated with constant f model (blue), calculated with Swamee-Jain model (red), measured (black). Pointwise velocity measurements taken by the tunnel anemometers (green) are also plotted. 79
4.11 Comparison between velocity profiles in Test 3: calculated with constant f model (blue), calculated with Swamee-Jain model (red), measured (black). Pointwise velocity measurements taken by the tunnel anemometers (red) are also plotted. 80
4.12 Comparison between velocity profiles in Test 4: calculated with constant f model (blue), calculated with Swamee-Jain model (red), measured (black). Pointwise velocity measurements taken by the tunnel anemometers (green) are also plotted. 80
4.13 Comparison between velocity profiles in Test 5: calculated with constant f model (blue), calculated with Swamee-Jain model (red), measured (black). Pointwise velocity measurements taken by the tunnel anemometers (green) are also plotted. 81
4.14 Validation of the algorithm against experimental data provided from the fixed sensors installed in the tunnel, on different occasions. Green line: calculated velocity profile. Gray dotted line: velocity profile as calculated by the tunnel control system (SCADA). Red squares: local velocity as measured by fixed anemometers. (a) 2018-03-01 03:37:00, $\Delta p = -850.59$ Pa (b) 2018-03-01 06:12:41, $\Delta p = -746.49$ Pa (c) 2018-10-07 14:15:30, $\Delta p = 29.59$ Pa (d) 2019-04-09 05:40:45, $\Delta p = 117.21$ Pa (e) 2019-05-16 16:13:46, $\Delta p = 116.69$ Pa (f) 2019-05-27 23:29:27, $\Delta p = 117.46$ Pa 83

5.1 Validation of the unsteady solver results against experimental data recorded from the emergency system test performed on 2018-03-01, with initial $\Delta p = -850.59$ Pa. Green line: calculated velocity profile. Gray dotted line: velocity profile as calculated by the tunnel control system (SCADA). Red squares: local velocity as measured by fixed anemometers. The frames concern different instants, identified by their distance in seconds from the simulation start time 03:37:00. (a) 0 s (b) 100 s (c) 200 s (d) 300 s (e) 400 s (f) 500 s (g) 900 s (h) 1300 s 91
5.2 Validation of the unsteady solver results against experimental data recorded from the emergency system test performed on 2019-04-09, with initial $\Delta p = 117.21$ Pa. Green line: calculated velocity profile. Gray dotted line: velocity profile as calculated by the tunnel control system (SCADA). Red squares: local velocity as measured by fixed anemometers. The frames concern different instants, identified by their distance in seconds from the simulation start time 05:40:45. (a) 0 s (b) 100 s (c) 150 s (d) 200 s (e) 300 s (f) 500 s (g) 540 s (h) 580 s 92
5.3 Comparison of the modeled PID action (blue lines) and the recorded data concerning the behavior of the PID control embedded in the system. Dotted line: number of active jet fan couples, as requested by the PID control. Full line: effective number of active jet fan couples in the TMB tunnel. The frames concern two different events: (a) 2018-03-01 03:37:00, $\Delta p = -850.59$ Pa (b) 2019-04-09 05:40:45, $\Delta p = 117.21$ Pa 93

6.1 Schematic of the experimental facility. 96
6.2 Different extraction vents shapes. (from [31]) 97
6.3 Calibration of the rotameter (from [31]) 99
6.4 Different flow regimes: smoke distribution in absence (a), and in presence (b) of the confinement condition. 100
6.5 Examples of stratification patterns of the smoke in the tunnel. 101
6.6 Confinement velocity curves as a function of longitudinal tunnel velocity, for different couples of source parameters. 107
6.7 Confinement velocity as a function of longitudinal tunnel velocity, for different dampers configurations. 107
6.8 Flow rate at the depressurized end, for different couples of source parameters. 108
6.9 Flow rate at the depressurized, for different dampers configurations. 108

List of Tables

3.1 Coefficients in Eq. (3.9.8) as a function of n. 40
3.2 Coefficients in Eq. (3.9.9) for AV and *relais* fans. 41
3.3 Reference length and coefficients of the reduced curve equation (3.9.10). . . 41
3.4 Parameters for a jet fan couple in the *Mont Blanc* tunnel, Eq. (3.9.18). . . . 47

4.1 Details of the five experimental tests including average pressure and temperature values at the portals, net pressure gradient and natural draught velocity, total flow rates through the ventilation channels (inlet and outlet), settings for fresh air supply, reference metric points for the opening of extraction vents, number of active jet fans and their direction. 69
4.2 Parameters range for DOE and optimization processeses. 77
4.3 Calibrated parameter set (left), RMS deviation for each of the 5 cases (right). 77
4.4 Details of the data base events that were chosen for the validation. 84

List of Symbols

Symbols

$\boldsymbol{A}$	incidence matrix [-]
$\boldsymbol{S}$	cross section [m^2]
$\boldsymbol{c}$	specific heat [J kg^{-1} K^{-1}]
$\boldsymbol{D_h}$	hydraulic diameter [m]
f	friction factor [-]
g	gravitational acceleration [m s^{-2}]
$\boldsymbol{k}_E, \boldsymbol{m}_E$	thermal power source term coefficients [W m^{-3}, W m^{-3} K^{-1}]
$\boldsymbol{k}_M, \boldsymbol{m}_M$	mechanical energy source term coefficients [J m^{-3}, J s m^{-4},]
L	length [m]
$\boldsymbol{P}$	total pressure [Pa]
$\boldsymbol{q}_g$	generated thermal power per unit volume [W m^{-3}]
R	gas constant [J kg^{-1} K^{-1}]
s	longitudinal coordinate [m]
$\boldsymbol{T}$	temperature [^{o}C]
$\boldsymbol{u}$	velocity [m s^{-1}]
U	heat transfer coefficient [W m^{-2} K^{-1}]
w	mean longitudinal velocity [m s^{-1}]
x	longitudinal coordinate [m]
y	wall-normal coordinate [m]
$\boldsymbol{M}$	upwinding operator [-]

Greek letters

β	concentrated loss coefficient [-]

$\gamma_{0,1,2}$	fan curves coefficients [J $s^{0,1,2}$ m $s^{-3,-4,-5}$ [-]
$\boldsymbol{\rho}$	density [kg m^{-3}]
$\boldsymbol{\sigma_M}$	volumetric momentum source term [J m^{-3}]
$\boldsymbol{\sigma_E}$	volumetric thermal power source term [W m^{-3}]

Superscripts

$\dot{}$	flow rate
$\bar{}$	boundary value
$*$	initial guess
$\prime$	correction

Subscripts

bn	branch-to-node
fan	fan
i	node index
j	branch index
l	auxiliary index
$loss$	friction loss
nb	node-to-branch

Chapter 6: Symbols

L	length of the smoke back-layer [m]
H	tunnel height [m]
Γ	plume Richardson number [-]
D	hydraulic diameter [m]
A	section area [m^2]
S	dimensionless shape coefficient [-]
P	dimensionless position coefficient [-]
Fr	Froude number [-]
B	buoyancy [-]

Chapter 6: Subscripts

s	buoyant source

0	tunnel entrance section
D	damper
e	extraction

Bibliography

[1] Richard Carvel and Alan Beard. *The Handbook of Tunnel Fire Safety.* Thomas Telford, 01 2005.

[2] A. Haack. Fire protection in traffic tunnels: General aspects and results of the eureka project. *Tunnelling and Underground Space Technology*, 13(4):377–381, 1998.

[3] Massachusetts Highway Department. Memorial tunnel fire ventilation test program comprehensive test report. Technical report, 1995.

[4] Tony Lemaire and Yvonne Kenyon. Large scale fire tests in the second benelux tunnel. *Fire Technology*, 42:329–350, 01 2006.

[5] RO Carvel, AN Beard, and PW Jowitt. The influence of longitudinal ventilation systems on fires in tunnels. *Tunnelling and Underground space Technology*, 16:3–21, 2001.

[6] B Brousse, A Voeltzel, Y Boltlan, and Emma Ruffin. Mont blanc tunnel ventilation and fire tests. *Tunnel Management International*, 5:13–22, 2002.

[7] A Martegani, G Pavesi, and C Barbetta. The influence of separation, inclination and swirl on single and double jet fans installation efficiency. In *9th International conference on Aerodynamics and Ventilation of Vehicle Tunnels*, pages 43–55, 1997.

[8] A. Król, M. Król, P. Koper, and P. Wrona. Numerical modeling of air velocity distribution in a road tunnel with a longitudinal ventilation system. *Tunnelling and Underground Space Technology*, 91, 2019.

[9] Yongdong Wang, Xingbo Han, Tianyue Zhou, Zhiwei He, Feilong Tian, Zhuoqi Zheng, and Haiping Zhao. Road tunnel axial fan performance in situ test: Taking qinling zhongnan mountain highway tunnel as an example. *Mathematical Problems in Engineering*, 2019.

[10] Chao Qian, Jianxun Chen, Yanbin Luo, and Zhongjie Zhao. Monitoring and analysis of the operational environment in an extra-long highway tunnel with longitudinal ventilation. *Tunnelling and Underground Space Technology*, 83:475 – 484, 2019.

[11] Mingnian Wang, Xu Wang, Li Yu, and Tao Deng. Field measurements of the environmental parameter and pollutant dispersion in urban undersea road tunnel. *Building and Environment*, 149:100 – 108, 2019.

[12] P Levoni, D Angeli, E Stalio, GS Barozzi, and M Cipollone. Concept, design, construction and testing of an experimental facility for multi-point longitudinal air flow measurements in tunnels. *Proceedings of the 29th UIT Heat Transfer Conference*, pages 507–512, 2011.

[13] P Levoni, A Scorcioni, D Angeli, E Stalio, GS Barozzi, and M Cipollone. TALPA: an innovative facility for continuous longitudinal airflow profile acquisition in tunnels. *Proceedings of the 30th UIT Heat Transfer Conference*, pages 325–330, 2012.

[14] P. Levoni, D. Angeli, P. Cingi, G.S. Barozzi, and M. Cipollone. An integrated approach for the analysis and modeling of road tunnel ventilation. Part I: Continuous measurement of the longitudinal airflow profile. *Transportation Engineering*, 3:100039, 2021.

[15] O. Vauquelin and O. M/'egret. Smoke extraction experiments in case of fire in a tunnel. *Fire Safety Journal*, 37(5):525–533, 2002.

[16] O. Vauquelin and D. Telle. Definition and experimental evaluation of the smoke "confinement velocity" in tunnel fires. *Fire Safety Journal*, 40(4):320–330, 2005.

[17] O. Vauquelin. Experimental simulations of fire-induced smoke control in tunnels using an "air–helium reduced scale model": Principle, limitations, results and future. *Tunnelling and Underground Space Technology*, 23(2):171–178, 2008.

[18] Y. Wang, J. Jiang, and D. Zhu. Full-scale experiment research and theoretical study for fires in tunnels with roof openings. *Fire Safety Journal*, 44(3):339–348, 2009.

[19] C.G. Fan, J. Ji, Z.H. Gao, J.Y. Han, and J.H. Sun. Experimental study of air entrainment mode with natural ventilation using shafts in road tunnel fires. *International Journal of Heat and Mass Transfer*, 56(1):750–757, 2013.

[20] H. Ingason and Y. Z. Li. Model scale tunnel fire tests with point extraction ventilation. *Journal of Fire Protection Engineering*, 21(1):5–36, 2011.

[21] J. Ji, Z.H. Gao, C.G. Fan, W. Zhong, and J.H. Sun. A study of the effect of plug-holing and boundary layer separation on natural ventilation with vertical shaft in urban road tunnel fires. *International Journal of Heat and Mass Transfer*, 55(21):6032–6041, 2012.

[22] X. Jiang, X. Liao, S. Chen, J. Wang, and S. Zhang. An experimental study on plug-holing in tunnel fire with central smoke extraction. *Applied Thermal Engineering*, 138:840–848, 2018.

[23] P. Zhao, Z. Yuan, Y. Yuan, N. Yu, and T. Yu. A study on ceiling temperature distribution and critical exhaust volumetric flow rate in a long-distance subway tunnel fire with a two-point extraction ventilation system. *Energies*, 12(8), 2019.

[24] Tao Du, Dong Yang, Shini Peng, Yingli Liu, and Yimin Xiao. Performance evaluation of longitudinal and transverse ventilation for thermal and smoke control in a looped urban traffic link tunnel. *Applied Thermal Engineering*, 96:490–500, 2016.

[25] Eui Ju Lee, Chang Bo Oh, Kwang Chul Oh, Yong Ho Yoo, and Hyun Joon Shin. Performance of the smoke extraction system for fires in the busan–geoje immersed tunnel. *Tunnelling and Underground Space Technology*, 25(5):600–606, 2010.

[26] L.F. Chen, L.H. Hu, X.L. Zhang, X.Z. Zhang, X.C. Zhang, and L.Z. Yang. Thermal buoyant smoke back-layering flow length in a longitudinal ventilated tunnel with ceiling extraction at difference distance from heat source. *Applied Thermal Engineering*, 78:129–135, 2015.

[27] F. Tang, L.J. Li, M.S. Dong, Q. Wang, F.Z. Mei, and L.H. Hu. Characterization of buoyant flow stratification behaviors by richardson (froude) number in a tunnel fire with complex combination of longitudinal ventilation and ceiling extraction. *Applied Thermal Engineering*, 110:1021–1028, 2017.

[28] Julien Le Clanche, Pietro Salizzoni, Mathieu Creyssels, R Mehaddi, F Candelier, and O Vauquelin. Aerodynamics of buoyant releases within a longitudinally ventilated tunnel. *Experimental thermal and fluid science*, 57:121–127, 2014.

[29] Lei Jiang, Mathieu Creyssels, Antoine Mos, and Pietro Salizzoni. Critical velocity in ventilated tunnels in the case of fire plumes and densimetric plumes. *Fire Safety Journal*, 101:53 – 62, 2018.

[30] F. Chaabat, M. Creyssels, A. Mos, J. Wingrave, H. Correia, M. Marro, and P. Salizzoni. The effects of solid barriers and blocks on the propagation of smoke within longitudinally ventilated tunnels. *Building and Environment*, 160:106207, 2019.

[31] F. Chaabat, P. Salizzoni, M. Creyssels, A. Mos, J. Wingrave, H. Correia, and M. Marro. Smoke control in tunnel with a transverse ventilation system: An experimental study. *Building and Environment*, 167:106480, 2020.

[32] Rudolf E Greuer. Study of mine fires and mine ventilation; part i. *Computer Simulation of Ventilation Systems Under the Influence of Mine Fires*, 1977.

[33] National Technical Information Service. *User's guide for the TUNVEN and DUCT programs*. 1980.

[34] U. S. Bureau of Mines. *MFIRE users manual Version 2.20*. 1995.

[35] L.H Cheng, T.H Ueng, and C.W Liu. Simulation of ventilation and fire in the underground facilities. *Fire Safety Journal*, 36(6):597–619, 2001.

[36] I Riess, M Bettelini, and R Brandt. Sprint-a design tool for fire ventilation. In *BHR Group Conf. Series Publication*, volume 43, pages 629–638. Bury St. Edmunds; Professional Engineering Publishing; 1998, 2000.

[37] Alok Majumdar, John Bailey, Biplap Sarkar, Alok Majumdar, John Bailey, and Biplap Sarkar. A generalized fluid system simulation program to model flow distribution in fluid networks. In *33rd Joint Propulsion Conference and Exhibit*, page 3225, 1997.

[38] United States Department of Transportation. Subway environmental simulation computer program, user's manual. Technical report, 1997.

[39] United States Department of Transportation. Subway environmental simulation computer program, programmer's manual. Technical report, 1997.

[40] Ying Wang and Xiaofeng Li. Stess: Subway thermal environment simulation software. *Sustainable Cities and Society*, 38:98–108, 2018.

[41] Zhenzhen Li, Chao Chen, Song Pan, Le Yan, and Kang Li. The effective use of the piston effect, natural cold sources, and energy saving in beijing subways. *Advances in Mechanical Engineering*, 5, 2013.

[42] Chi-Ji Lin, Yew Khoy Chuah, and Chia-Wei Liu. A study on underground tunnel ventilation for piston effects influenced by draught relief shaft in subway system. *Applied Thermal Engineering*, 28:372–379, 2008.

[43] Shih-Cheng Hu and Jen-Ho Lee. Influence of platform screen doors on energy consumption of the environment control system of a mass rapid transit system: case study of the taipei mrt system. *Energy Conversion and Management*, 45(5):639–650, 2004.

[44] Ming-Tsun Ke, Tsung-Che Cheng, and Wen-Por Wang. Numerical simulation for optimizing the design of subway environmental control system. *Building and Environment*, 37(11):1139–1152, 2002.

[45] J E Floyd, S P Hunt, Frederick W Williams, and P A Tatem. Fire and smoke simulator (fssim) version 1-theory manual. Technical report, NAVAL RESEARCH LAB WASHINGTON DC, 2004.

[46] Hong-Ming Jang and Falin Chen. On the determination of the aerodynamic coefficients of highway tunnels. *Journal of Wind Engineering and Industrial Aerodynamics*, 90(8):869–896, 2002.

[47] D A Charters, W A Gray, and McIntosh A C. A computer model to assess fire hazards in tunnels (fasit). *Fire Technology*, 30:134–154, 02 1994.

[48] K. Suzuki, Takeyoshi Tanaka, and Kazunori Harada. Tunnel fire simulation model with multi-layer zone concept. *Fire Safety Science*, 9:713–723, 01 2009.

[49] Richard D Peacock, Walter W Jones, Paul A Reneke, and Glenn P Forney. Cfast–consolidated model of fire growth and smoke transport (version 6). Technical report, NIST, 2008.

[50] C A Wade. *BRANZFIRE Technical reference guide*. BRANZ, 2000.

[51] B.Y. Lattimer, J.L. Hodges, and A.M. Lattimer. Using machine learning in physics-based simulation of fire. *Fire Safety Journal*, 114, 2020.

[52] T. Buffington, J.-M. Cabrera, A. Kurzawski, and O.A. Ezekoye. Deep-learning emulators of transient compartment fire simulations for inverse problems and room-scale calorimetry. *Fire Technology*, 2020.

[53] J.L. Hodges, B.Y. Lattimer, and K.D. Luxbacher. Compartment fire predictions using transpose convolutional neural networks. *Fire Safety Journal*, 108, 2019.

[54] G. Cox. *Combustion fundamental of fire*. Academic press, 1995.

[55] D.F. Fletcher, J.H. Kent, V.B. Apte, and A.R. Green. Numerical simulations of smoke movement from a pool fire in a ventilated tunnel. *Fire Safety Journal*, 23(3):305–325, 1994.

[56] Y Wu and MZA Bakar. Control of smoke flow in tunnel fires using longitudinal ventilation systems. *Fire Safety Journal*, 35:363–390, 2000.

[57] Jojo S.M Li and W.K Chow. Numerical studies on performance evaluation of tunnel ventilation safety systems. *Tunnelling and Underground Space Technology*, 18(5):435–452, 2003.

[58] P.Z. Gao, S.L. Liu, W.K. Chow, and N.K. Fong. Large eddy simulations for studying tunnel smoke ventilation. *Tunnelling and Underground Space Technology*, 19(6):577–586, 2004.

[59] Sung Ryong Lee and Hong Sun Ryou. A numerical study on smoke movement in longitudinal ventilation tunnel fires for different aspect ratio. *Building and Environment*, 41(6):719–725, 2006.

[60] Rafael Ballesteros-Tajadura, Carlos Santolaria-Morros, and Eduardo Blanco-Marigorta. Influence of the slope in the ventilation semi-transversal system of an urban tunnel. *Tunnelling and Underground Space Technology incorporating Trenchless Technology Research*, 21(1):21–28, 2006.

[61] Mihyun Kim, John Woycheese, and Nicholas Dembsey. Fire dynamics simulator (version 4.0) simulation for tunnel fire scenarios with forced, transient, longitudinal ventilation flows. *Fire Technology*, 44:137–166, 06 2008.

[62] KB Maele and B Merci. Application of rans and les field simulatios to predict the ventilation velocity in longitudinally ventilated horizontal tunnels. *Fire Safety Journal*, 43:598–609, 2008.

[63] Miao Cheng Weng, Long Xing Yu, Fang Liu, and Peter V Nielsen. Full-scale experiment and cfd simulation on smoke movement and smoke control in a metro tunnel with one opening portal. *Tunneling and Underground Space Technology*, 42:96–104, 2014.

[64] Aleksander Król and Malgorzata Król. Transient analyses and energy balance of air flow in road tunnels. *Energies*, 11(7), 2018.

[65] Francesco Colella, Guillermo Rein, Romano Borchiellini, R Carvel, Jose L Torero, and Vittorio Verda. Calculation and design of tunnel ventilation systems using a two-scale modelling approach. *Building and Environment*, 44(12):2357–2367, 2009.

[66] Francesco Colella, Guillermo Rein, R Carvel, Pedro Reszka, and Jose L Torero. Analysis of the ventilation systems in the Dartford tunnels using a multi-scale modelling approach. *Tunneling and Underground Space Technology*, 25(4):423–432, 2010.

[67] Francesco Colella, Guillermo Rein, Romano Borchiellini, and Jose L Torero. A novel multiscale methodology for simulating tunnel ventilation flows during fires. *Fire Technology*, 47(1):221–253, 2011.

[68] F. Colella, G. Rein, V. Verda, and R. Borchiellini. Multiscale modeling of transient flows from fire and ventilation in long tunnels. *Computers and Fluids*, 51(1):16–29, 2011.

[69] F Colella. *Multiscale Modelling of Tunnnel Ventilation Flows and Fires.* PhD thesis, Politecnico di Torino, 2010.

[70] B Ralph and R Carvel. Coupled hybrid modelling in fire safety engineering; a literature review. *Fire Safety Journal*, 100:157–170, 2018.

[71] D. Burton, A. Grandison, M. Patel, E. Galea, and J. Ewer. Development of a hybrid field/zone fire model. 2011.

[72] Y. Jiao, J.-H. Wang, M.-J. Xiao, T. Xu, and W.-J. Chen. Development of field-zone-net model for fire smoke propagation simulation in ships. pages 190–193, 2015.

[73] J. Srebric, J. Yuan, and A. Novoselac. On-site experimental validation of a coupled multizone and cfd model for building contaminant transport simulations. volume 114 PART 1, pages 273–281, 2008.

[74] Izabella Vermesi, Guillermo Rein, Francesco Colella, Morten Valkvist, and Grunde Jomaas. Reducing the computational requirements for simulating tunnel fires by combining multiscale modelling and multiple processor calculation. *Tunnelling and Underground Space Technology*, 64:146 – 153, 2017.

[75] P Levoni, D Angeli, GS Barozzi, and M Cipollone. Seconda campagna di rilievi a postazione fissa del flusso innescato dagli acceleratori di volta. internal report, 2011.

[76] R. Diestel. *Graph Theory.* Springer, 1997.

[77] R. W. Fox and McDonald A. T. *Introduction to fluid mechanics 4th edition.* John Wiley and Sons, 1995.

[78] P. Levoni, D. Angeli, E. Stalio, E. Agnani, G.S. Barozzi, and M. Cipollone. Fluid-dynamic characterisation of the mont blanc tunnel by multi-point airflow measurements. *Tunnelling and Underground Space Technology*, 48:110–122, 2015.

[79] Suhas V Patankar. *Numerical heat transfer and fluid flow.* Hemisphere Publishing Corporation (CRC Press, Taylor & Francis Group), 1980.

[80] V Ferro, R Borchiellini, and V Giaretto. Description and application of tunnel simulation model. In *Proceedings of Aerodynamics and Ventilation of Vehicle Tunnels Conference*, pages 487–512, 1991.

[81] C F Colebrook. Turbulent flow in pipes, with particular reference to the transition region between the smooth and rough pipe laws. *Journal of the Institution of Civil Engineers*, 11(4):133–156, 1939.

[82] D.K. Swamee and A.K. Jain. Explicit equations for pipe flow problems. *Journal of the Hydraulics Division*, 102:657–664, 1976.

[83] M. Cavazzuti. *Optimization Methods: from Theory to Design.* Springer, 2015.

[84] U. Steinemann and F. Zumsteg. Measurements of air flow, temperature differences and pressure differences in road tunnels. In *International Conference "Tunnel Safety and Ventilation"*, 2004.

[85] Lei Jiang, Mathieu Creyssels, Antoine Mos, and Pietro Salizzoni. Critical velocity in ventilated tunnels in the case of fire plumes and densimetric plumes. *Fire Safety Journal*, 101:53–62, 2018.

[86] P. Salizzoni, M. Creyssels, L. Jiang, A. Mos, R. Mehaddi, and O. Vauquelin. Influence of source conditions and heat losses on the upwind back-layering flow in a longitudinally ventilated tunnel. *International Journal of Heat and Mass Transfer*, 117:143–153, 2018.

[87] B.R. Morton, G.I. Taylor, and J.S. Turner. Turbulent gravitational convection from maintained and instantaneous sources. *Proc. Roy. Soc.*, A234:1–23, 1956.

[88] L Jiang, M Creyssels, GR Hunt, and P Salizzoni. Control of light gas releases in ventilated tunnels. *Journal of Fluid Mechanics*, 872:515–531, 2019.

Ringraziamenti

La lista delle persone che potrei ringraziare per il loro supporto durante i miei studi sarebbe molto lunga. Resisterò tuttavia alla tentazione di perdermi in una lunga pagina di nomi e convenevoli, preferendo un più conciso ringraziamento diretto alle persone che hanno dato svolte fondamentali al mio percorso scientifico, nell'ordine in cui le ho incontrate. In questo lavoro di tesi convivono, in misure diverse, i contributi di tutti e quattro.

Vorrei ringraziare Maurizio Cingi, Diego Angeli, Carlo Innocenti, Josep Illa.